12-2019

Measurement of the Fierz Interference Term for Calcium-45

Noah Birge
University of Tennessee, nbirge@vols.utk.edu

To the Graduate Council:

I am submitting herewith a dissertation written by Noah Birge entitled "Measurement of the Fierz Interference Term for Calcium-45." I have examined the final electronic copy of this dissertation for form and content and recommend that it be accepted in partial fulfillment of the requirements for the degree of Doctor of Philosophy, with a major in Physics.

Nadia Fomin, Major Professor

We have read this dissertation and recommend its acceptance:

Geoffrey Greene, Soren Sorensen, Maik Lang, Thomas Papenbrock

Accepted for the Council:

Dixie L. Thompson

Vice Provost and Dean of the Graduate School

(Original signatures are on file with official student records.)

Measurement of the Fierz Interference Term for Calcium-45

A Dissertation Presented for the

Doctor of Philosophy

Degree

The University of Tennessee, Knoxville

Noah Watson Birge

December 2019

To my beloved wife Sarah, without whom I would be adrift.

Acknowledgements

First I'd like to thank the folks out at Los Alamos National Lab for all of the assistance with the ^{45}Ca beta spectrum measurement and cooling system tests. Mark Makela and Steve McDonald made it all possible.

Secondly I'd like to thank Aaron Jezghani, David Mathews, Thomas Bailey, Camen Royce, and Huangxing Li. Their work with the various components of the ^{45}Ca experiment was crucial. I'm also indebted to Leendert Hayen for his work in generating the beta spectrum shape for ^{45}Ca.

I'd also like to especially thank Bryan Zeck for all of his work with in developing a simulation for the ^{45}Ca experiment. This work was not initially in the scope of his thesis work, but he took it on anyway.

I would like to thank Stefan Baessler, Dinko Počanić, and Albert Young for their help in assembly of the experiment and their input in analyzing the collected data. I'm especially grateful for Albert's organization of the experiment and participating institutions.

I would like to thank Ben Luffman, Maria Zemke, and Levi Carleton for their engineering work with the cooling system.

I am also grateful for all of the help from John Ramsey. From reviewing my 3D models and engineering diagrams to his input and calculations towards the development of the cooling system, he has provided a great deal of invaluable insight.

I would like to thank Ryan Whitehead and David Perryman. Ryan has been a great for bouncing ideas off of and a source of very useful and constructive criticism.

David Perryman was vital in a large portion of the systematic studies carried out. Additionally, his machine learning work has been very intriguing and will be a useful tool in the future.

I would like to thank Grant Riley for his mentoring and advice, especially in regards to analysis and scientific communication. I'd also like to thank him for the careful editing of this work in its entirety.

I would like to thank Leah Broussard for her various analysis routines. The work to follow stems from much of her work. She has also provided key insights in terms of analyzing and extracting useful information from the data collected.

I would like to thank John Ramsey for all of his help and advice in creating proper engineering drawings and reviewing those which I created. I would also like to thank him for the calculations which he performed in support of the redesign of the cooling system.

I would like to thank Josh Pierce for his advice in the design and testing of the Nab cooling system. I gleaned quite a bit of hardware and cryogenic expertise thanks to Josh.

Finally, I would most of all like to thank my advisor Professor Nadia Fomin for taking me on as her graduate student and all of the guidance that she has provided throughout the process. Her patience and mentorship have imparted me with an invaluable set of scientific skills.

Abstract

The Standard Model (SM) is one of the most complete theories of fundamental particle physics. Despite its wide success, there are still mechanisms for which the SM does not account. Neutrino flavor oscillations, the observed baryon asymmetry, and the dark matter puzzle make it clear that there must exist a sector of physics which is beyond the standard model (BSM). As such, a plethora of BSM extensions have been proposed, necessitating experiments with the ability to validate or set limits upon these extensions. Beta decay spectrum shape measurements provide the ability to probe possible scalar and tensor current interactions not included in the SM. The Nab experiment and a related ^{45}Ca beta spectrum measurement aim to measure the Fierz interference term 'b', which is a purely BSM decay correlation parameter. The following will discuss some aspects of the Nab experiment as well as the current limits placed on 'b' by the aforementioned ^{45}Ca beta spectrum measurement.

Table of Contents

List of Tables

List of Figures

List of Attachments

- High voltage feedthrough design drawings (HV_FT_drawing.pdf)
- Ramsey Bayonet design drawings (Ramsey_bayonet_drawing.pdf)
- Dip Tube Feedthrough design drawings (dip_tube_feedthrough_drawing.pdf)
- Vacuum vessel design drawings (Vacuum_vessel_drawing.pdf)
- Heat exchanger design drawings (HE_drawing.pdf)
- Heat exchanger mount plate design drawings (HE_mount_plate_drawing.pdf)
- Full cooling schematics (Cooling_loop_schematics.pdf)

Chapter 1

Introduction

1.1 Nuclear Decay History

Nuclear radioactivity was first discovered by Henri Becquerel in 1896 while experimenting with photographic plates [1–3]. Subsequent discoveries made by Peter and Marie Curie as well as Hans Geiger and Earnest Rutherford began to illuminate the emerging field of nuclear physics. Rutherford categorized the observed decay modes as alpha, gamma, and beta decay, depending on the penetration depth of the particle ejected from the radioactive nucleus. Initially, alpha decay was characterized as having the smallest penetration depth. A few sheets of paper was more than sufficient to shield from alphas. Charge-to-mass measurements would eventually lead to the identification of the alpha particle as a ^{4}He nucleus. The particles emitted in beta decay were termed "beta rays" and were somewhat more penetrating than alpha particles. Eventually, Becquerel's measurement of the charge-to mass ratio of these "beta rays" proved to be consistent with that of J.J. Thomson's "cathode ray" charge-to-mass measurements. Hence the "beta ray" was identified as an electron. Gamma rays were initially thought to be neutral, massive, highly energetic particles. Gamma radiation was observed to be the most penetrating form of radiation and its trajectory was unperturbed by the presence of a magnetic field. Rutherford would

go on to find that these gamma rays could be reflected from a crystal surface and established that these gamma rays were in fact electromagnetic radiation [4].

As the field matured and new experimental techniques were developed, energy measurements for these decay particles became tractable. This was particularly intriguing for beta decay measurements due to the unexpected nature of the observed electron energy spectrum. At the time, beta decay was thought to be a two-body process, which should give rise to a very narrow band of allowed electron energies. In actuality, a continuous electron energy spectrum was observed. An understanding of the underlying cause eluded physicists until 1930, when Wolfgang Pauli proposed a three-body process to explain the observed spectrum of beta decay. In addition to the electron, it was postulated that a neutral particle is also ejected from the beta decaying nucleus. This particle was initially termed a neutron by Pauli, and the assumption was that this ejected particle resided in the nucleus. James Chadwick would go on to show that the mass of the nuclear neutron was too large to be consistent with the ejected particle proposed by Pauli. Hence the posited neutral particle ejected in a beta decay process was renamed to neutrino, or "small neutron" in Italian. Shortly thereafter, Enrico Fermi developed a formalism for beta decay where a neutron decays into a proton and emits an electron and said neutrino [5]. Direct detection of the neutrino was finally achieved by Clyde Cowan and Frederick Reines [6], which confirmed Pauli's hypothesis and Fermi's formalism.

Since the direct detection of the neutrino, the field of nuclear physics has taken substantial leaps. Several other modes of nuclear decay such as spontaneous fission [7], single and two-proton emission [8–10], neutron emission, and a whole host of various forms of beta decay have since been observed. From Rutherford's initial perception that radioactive decay rates obey Poisson statistics and Fermi's model of the nuclear interaction [5] to the development of the Standard Model (SM) [11–13] and a plethora of effective field theories [14], the theoretical framework to describe nuclei has also seen much development. Nevertheless, 120 years after its advent, there are still countless avenues worth exploring in nuclear physics.

1.2 Beta Decay and the Standard Model

The Standard Model of particle physics describes the interaction of elementary particles on the most fundamental level. The theory has withstood test after test and numerous predictions have been made with SM roots [11–13, 15, 16], which were later observed by experiment[17–19]. Although the theory has not yet been shown to be incorrect, it is clear that it is incomplete. One of the most glaring deficits is the absence of a gravitational interaction. The trajectories of celestial bodies can be determined to high precision with Newtonian Mechanics an General Relativity. However, there are no candidate mediating bosons or interactions currently included in the SM that can give rise to this long-range gravitational interaction that is so well understood macroscopically. According to the SM, neutrinos are massless particles. The absence of neutrino mass implies that each so called neutrino flavor state would be completely stable. Various experiments however have observed neutrino oscillation between flavor states [20–22]. The SM is also unable to address the apparent baryon-antibaryon asymmetry. There are no mechanisms included in the SM which give a preference to the production of baryons to antibaryons to a degree that is consistent with current observations. The majority of the known universe is composed primarily of baryonic matter. Various searches have limited the possible existence of anti-baryonic to amounts inconsistent with the SM [23–25]. Forays into these research topics and others search for so called Beyond Standard Model (BSM) processes or structures to explain one or more of the aforementioned discrepancies.

1.2.1 SM Particle Content

The SM itself is a quantum field theory (QFT) which describes interactions of fundamental particles in terms of fields. In much the same way the interaction of electric charges can be described in terms of electric and magnetic fields, fundamental interactions are governed by particle fields in the SM. These particles can be found in Fig. 1.1. Note that the abbreviations used in Fig. 1.1 will be used for the remainder

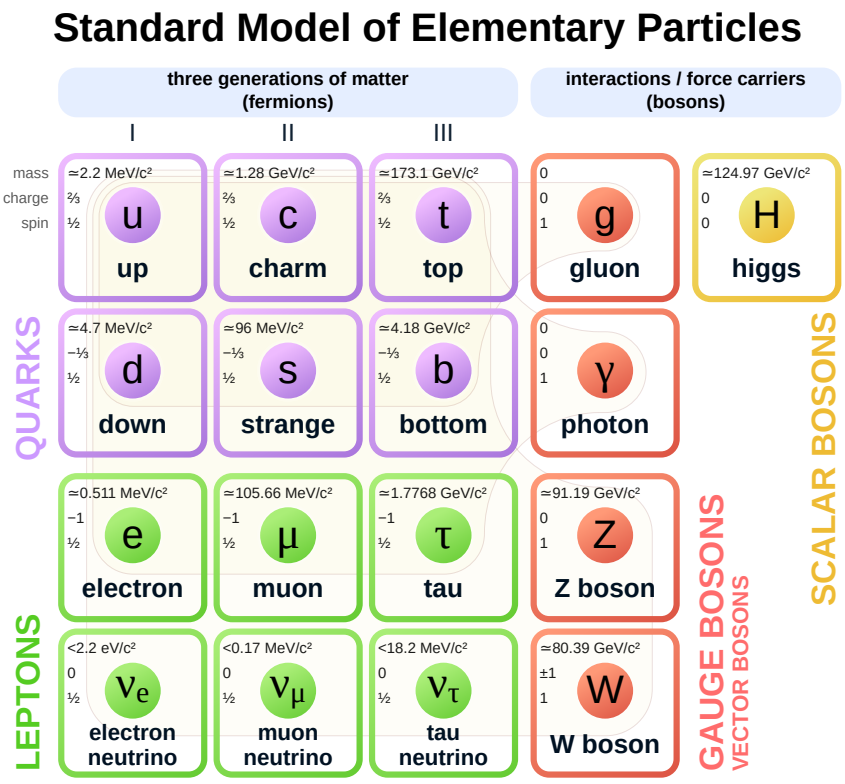

Figure 1.1: The above shows the particles included int the SM. [26]. The fermions (quarks and leptons) consit of six flavors, and are all spin 1/2 particles. The vector bosons are all spin 1 particles and are the mediators for the SM interactions. The Higgs boson is a spin 0 (scalar) boson which couples to fermions and the Z and W bosons, which gives rise to nonzero masses.

of the document, i.e. an up quark will be represented by u, a down quark by d, and so on.

All leptons and quarks are considered fermions, spin $\frac{1}{2}$ particles. There are six lepton types or flavors as well as six anti-lepton flavors which have equal mass but opposite charge to the corresponding lepton flavor. The only stable lepton is the electron. All others decay into lighter species, or in the case of the neutrinos, oscillate between neutrino flavors. The fundamental unit of charge is given in terms of the charge of the electron. Neutrinos are neutral leptons with no electric charge, while the remaining leptons have a charge of 1. There are also six quark flavors with an accompanying six anti-quark flavors. The charges of the quarks are either $\frac{2}{3}$ or $-\frac{1}{3}$. Due to the strength of the strong force which binds quarks to one another (discussed further in Sec. 1.2.2), quarks are not isolated particles. Instead, they typically form composite particles called hadrons. Hadrons with an even number of quark anti-quark pairs are referred to as mesons. Hadrons which are composed of three quarks are referred to as baryons. Protons and neutrons are examples of baryons.

All spin 1 or spin 0 particles are called. These bosons are responsible for mediating the various interactions between SM particles. Spin 1 bosons are referred to as vector bosons, since its spin may be projected along some axis, taking on values of -1, 0 or 1 for massive bosons. For massless bosons, the spin projection can take values of -1 or 1. The vector bosons include the photon, gluon, Z, W^+ and W^- ($W^\pm$) bosons. The gluon and photon are electrically neutral, massless and are involved in strong and electromagnetic interactions respectively. The Z and $W^\pm$ bosons are massive bosons which take part in the weak interaction. The $W^\pm$ bosons carry an electric charge of ± 1, and the Z boson is neutral. Spin 0 bosons are referred to as scalar bosons. The Higgs boson is the only fundamental scalar boson present in the SM. It is a chargless, massive boson, which is responsible for the generation of mass terms in the SM Lagrangian. Observation of and measurement of its mass has been the driving force for many large-scale collider based experiments. The first observation was achieved in 2012 via proton-proton collisions [19].

1.2.2 SM Interactions

The Higgs Couplings

The Higgs boson couples to all massive particles. In effect the Higgs boson can decay into any massive particle with a strength that goes as $\frac{m}{m_H}$, where m is the mass of the outgoing particle(s) and m_H is the mass of the Higgs. The coupling of each particle to this Higgs field gives rise to non-zero particle masses. The Higgs boson also participates in self-interactions or self-couplings whereby multiple Higgs bosons interact.

The Strong Interaction

The strong interaction is mediated by gluons. This interaction occurs between quarks and gluons. Both gluons and quarks carry an additional "color" charge. Unlike electric charge which consists of a single type of charge, color charge is one of three types. The standard colors used to denote the type of color charge for a given quark are red, green and blue. The corresponding color charges for the antiquarks are denoted as anti-red, anti-blue, or anti-green. A quark carries one of the three possible color charges. A gluon carries some combination of color-anticolor charges. The strong interaction between quarks occurs via the exchange of a gluon. The interaction of a gluon with each quark results in a quark color change. This exchange is responsible for the binding of quarks to form hadrons. Hadrons are referred to as colorless, as they either contain quarks of all three colors (or anticolors) or are composed of a color-anticolor pair. At the length scale of hadrons, the strong force does not diminish with increasing distance. Additionally, the strength of the strong force as measured by the size of the coupling constant (relative to the other fundamental interactions at this length scale) is the largest of all forces. Thus at some distance, the action of separating two quarks requires enough energy to produce another quark-antiquark pair from the vacuum, which bind to the original two quarks producing two (colorless) hadrons.

This is known as color confinement and is thought to be responsible for the lack of observations of isolated quarks.

Because these colorless hadrons are composite particles, there exists a residual strong interaction between hadrons, similar to the residual Coulomb interaction between to neighboring neutral molecules. This residual strong force is responsible for the binding of nucleons into nuclei. At length scales much smaller than 1 fm, the residual force is repulsive. At the range of a few fm, the net force is attractive, but quickly diminishes with increasing distance.

The Electroweak Interaction

The electroweak interaction, as the name implies, includes the weak and electromagnetic interactions. There are three sectors to the elctroweak interaction: the boson self-interactions, the "neutral current" and the "charged current" sectors. The self-interactions consist of the possible interactions among the photon, Z and W bosons. The neutral and charged current sectors concern the fermion to W/Z boson or photon couplings. In the neutral current sector, a fermion couples to one or both of the neutral vector bosons: the photon or Z boson. When the involved energy scale is much smaller than that of the rest mass of the Z boson, interactions are predominantly mediated by the photon and are electromagnetic in nature. At these scales, the resulting formalism is consistent with Quantum Electrodynamics. As energy tends towards the mass of the Z-boson, the Z-boson contribution becomes more relevant and must be included.

In addition to spin, mass, and charge, a particle field also has a "handedness". The handedness of a particle is only relevant to the weak charged current interaction, as the strong and weak neutral current interactions show no preference for the handedness of a particle and are thus parity conserving. The charged current interaction however only couples left handed particles or right-handed antiparticles to the W bosons. The parity violating nature of this interaction was first demonstrated in Ref. [27]. This experiment involved the observation of electron emission direction in the beta decay of polarized ^{60}Co. Under a parity conserving charged current sector, the preferred

direction of emission would be independent of the the nuclear polarization. However, the experiment showed a preferential direction of emission opposite to the spin of the polarized nucleus and thus established the parity violating structure of charged current processes.

Weak charged current interactions couple left-handed fermions to a W boson. The "charged" portion of the terminology originates from the fact that the mediating boson is a W^+ or W^- boson, which carries an electric charge. It is only this process through which a fermion flavor change can occur. Strong and neutral current interactions are flavor conserving and do not change the respective flavor of the fermions involved. As such, all forms of beta decay are charged current processes.

A Formalism for Beta Decay: The Electroweak Lagrangian

Beta minus decay is the mechanism by which a neutron (n) transitions into a proton (p) via the emission of a virtual W^- boson which decays into an electron (e^-) and electron anti-neutrino ($\overline{\nu}_{e^-}$). Within this document all symbols used to represent anti-particles will be written as the standard symbol with an overbar. The electron neutrino is written as ν_{e^-}, hence the electron anti-neutrino is written as $\overline{\nu}_{e^-}$.

$$n \rightarrow p + e^- + \overline{\nu}_{e^-} \tag{1.1}$$

$${}^{A}_{Z}X \rightarrow {}^{A}_{Z+1}X' + e^- + \overline{\nu}_{e^-} \tag{1.2}$$

In the above, X is an example nucleus with Z protons and A total number of nucleons in X. To first order, the likelihood of the transition is dictated energetically. If the transition is not energetically forbidden, it can occur. Thus a nucleus (termed the mother) may beta decay into a daughter nucleus if enough energy is available. For ground state nuclei, a nucleus may beta decay if the daughter product is less massive than the mother. Because this principle is true for any physical process, it also holds for the charge conjugated process where a nuclear proton transitions to a neutron via

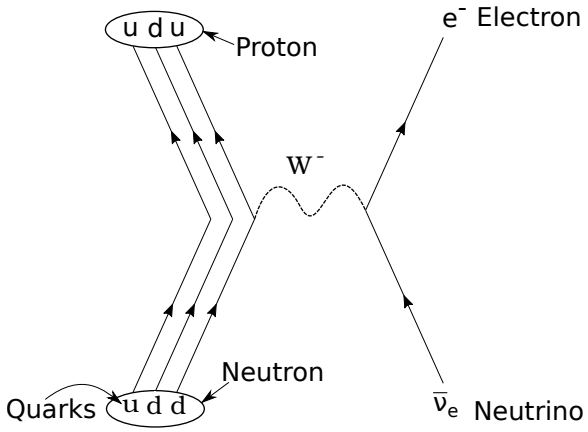

Figure 1.2: A neutron is composed of an up quark and two down quarks. A down quark decays into an up quark via the emission of a virtual W^- boson, which decays into an electron and electron-antineutrino.

the emission of a virtual W^+ boson. The W^+ promptly decays into a positron and electron neutrino. This process is known as beta plus decay and can be written as:

$$ {}^{A}_{Z}X \rightarrow {}^{A}_{Z-1}X' + e^+ + \nu_{e^-} \tag{1.3} $$

All beta decay processes can be represented by any particle-antiparticle rearrangement of Eqs. 1.2 and 1.3. The material below is only concerned with beta minus decay, and beta minus decay will simply be referred to as beta decay henceforth.

Returning to the SM, beta decay can be described at the quark level by the electroweak charged current interaction, whereby a down quark of the neutron transitions to an up quark through emission of a virtual W^- boson. The virtual vector minus boson decays into an electron and electron antineutrino (see Fig. 1.2). To mathematically describe this process, a Lagrangian QFT formalism is typically used. The form of the SM charged current Lagrangian governing the transition on the quark level is given as [28]:

$$ \mathcal{L}^{\mathrm{SM}}_{\mathrm{CC}} = \frac{ig_2}{2\sqrt{2}} \left[W^-_\mu \left(\overline{e}'_m \gamma^\mu \left(1+\gamma_5\right) \nu'_m + \left(V^\dagger\right)_{mn} \overline{d}'_m \gamma^u \left(1+\gamma_5\right) u'_n \right) \right] \tag{1.4} $$

Where g_2 is the weak gauge coupling, $g_2 = \frac{2M_W}{v}$, M_W the mass of the W boson, v the vacuum expectation value, W_i^- is the i'th component of the W^- field, and γ^i the i'th Dirac matrix, $V_{ij}^\dagger$ is the conjugate of the Cabbibo-Kobayashi-Maskawa matrix. e, ν, u, and d denote the quark or lepton Dirac spinor type, and the subscripts n and m denote the quark or lepton flavor. For example $u_1 = u$ represents the up quark Dirac spinor, $e_2 = \mu$ denotes the muon Dirac spinor, and $d_3 = b$ represents the bottom quark Dirac spinor. Also note that repeated indices indicate Einstein summations. Note that this interaction only includes a vector $(\overline{f}\gamma_\mu f')$ and axial vector $(\overline{f}\gamma_\mu\gamma_5 f')$ interactions. This need not be the only type of interaction included. The most general interaction would also include scalar $(\overline{f}f')$, pseudoscalar $\overline{f}\gamma_5 f'$, and tensor $(\overline{f}\sigma_{\mu\nu} f')$ contributions as well, see Ref. [29].

Effective Field Theories for the Weak Interaction

To deal with the complexity of the Lagrangian one may recast it in terms of relevant energy scales, i.e. an effective field theory (EFT). The quintessential example of an EFT is quantum electrodynamics (QED). While not necessarily developed as an EFT, the QED lagrangian results when the SM electroweak Lagrangian is restricted to interactions between charged particles with energies less than twice that of the muon rest mass. The advantage of such a method is that numerical calculations may be greatly simplified when performed in terms of an EFT. Additionally, an EFT can be used when much higher energy processes (or much heavier mediating particles) are relevant but not well known, and the low energy implications of their inclusion are desired. In such cases, operators are constructed from the well-understood fields and expanded in terms of the heavier particle mass.

The first principle in constructing an effective field theory is to identify the relevant energy scale. For the transition of a down quark into an up quark (i.e. a beta decay process), an EFT may be constructed by restricting the particle content to at most the mass of the down quark. Hence the relevant degrees of freedom (included particle content) are the up and down quarks, the electron, and the neutrinos. The full

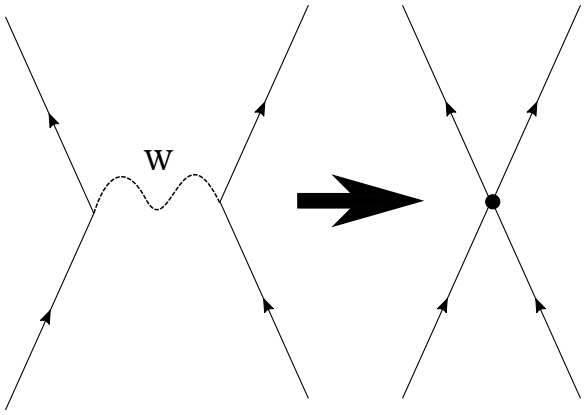

Figure 1.3: Shown above on the left is the transition of one fermion to another via the emission of a virtual W boson. With an appropriately modeled EFT, the diagram can instead be reduced to that on the right. Two 3-particle vertices with a virtual W boson internal line can instead be represented as a 4-particle vertex with an effective coupling.

calculation of transition probabilities would ordinarily include the W boson field and its propagation. Within an EFT framework where the energy of the incoming and outgoing particles are much smaller than the rest mass of the W boson, the momentum of the virtual W boson is negligible in comparison to its rest mass. The intermediate states can therefore be accounted for with a simple approximation which depends only on the intermediate particle mass. The SM charged current Lagrangian of Eq. 1.4 becomes:

$$\begin{aligned} \mathcal{L}_{\mathrm{CC}}^{\mathrm{SM}} &= e_W W_\mu^- C^\mu \\ \rightarrow \mathcal{L}'_{\mathrm{CC}} &= \frac{G_F}{\sqrt{2}} C^\mu C_\mu^* \end{aligned} \tag{1.5}$$

with $C^\mu := \sum_{m=1}^{3} \left[i\overline{e}\gamma^\mu \left(1+\gamma_5\right) \nu_e + \sum_{n=1}^{3} iU_{nm}^* \overline{d}_m \gamma^\mu \left(1+\gamma_5\right) u_n \right]$ and $\frac{G_F}{\sqrt{2}} = \frac{g_2^2}{8M_W^2}$ [28]. This effectively takes two three-particle vertices with virtual particle propagation and replaces the diagram with a four-particle interaction (see Fig. 1.3). Instead of evaluating the full propagation of the virtual W boson, the process is approximated by a four particle vertex with an effective coupling given by G_F.

The above is a SM EFT with Vector - Axial Vector (V-A) operators. A BSM EFT of beta decay may be constructed by postulating that heavier BSM particles exist and play a role in beta decay. Then in addition to the V-A SM operators additional operators can be included with an interaction strength (coupling constant) which scales as $\left(\frac{1}{\Lambda^2}\right)^n$, where Λ is the mass or energy scale of the BSM particle.

Ref. [30] developed a low-scale effective Lagrangian for semi-leptonic charged-current transitions. The EFT includes the standard up u, down d, electron e, and neutrino ν fields along with an additional right-handed neutrino state. The effective couplings $\epsilon_i : i \in \{\text{P,S,T,L,R}\}$ are pseudoscalar, scalar, tensor, left and right handed couplings, respectively. These couplings scale as $\epsilon_i, \tilde{\epsilon}_i \propto \left(\frac{m_W}{\Lambda}\right)$, and their exact form in terms of weak-scale couplings can be found in [30]. The energy scale was restricted to be on the order of 1 GeV. The resulting quark level Lagrangian is given as [30]:

$$
\begin{aligned}
\mathcal{L}_{\text{eff}} = -\frac{G_F V_{ud}}{\sqrt{2}} \Bigg[& \left(1+\epsilon_L\right) \bar{e}\gamma_\mu \left(1-\gamma_5\right) \nu_e \cdot \bar{u}\gamma^\mu(1-\gamma_5)d \\
& + \tilde{\epsilon}_L \bar{e}\gamma_m u \left(1+\gamma_5\right) \nu_e \cdot \bar{u}\gamma^\mu \left(1-\gamma_5\right) d \\
& + \epsilon_R \bar{e}\gamma_\mu \left(1-\gamma_5\right) \nu_e \cdot \gamma^\mu \left(1+\gamma_5\right) d + \tilde{\epsilon}_R \bar{e}\gamma_\mu \left(1+\gamma_5\right) \nu_e \cdot \bar{u}\gamma^u \left(1+\gamma_5\right) d \\
& + \epsilon_S \bar{e} \left(1-\gamma_5\right) \nu_e \cdot \bar{u}d + \tilde{\epsilon}_S \bar{e} \left(1+\gamma_5\right) \nu_e \cdot \bar{u}d \\
& - \epsilon_P \bar{e} \left(1-\gamma_5\right) \nu_e \cdot \bar{u}\gamma_5 d - \tilde{\epsilon}_P \bar{e} \left(1+\gamma_5\right) \nu_e \cdot \bar{u}\gamma_5 d \\
& + \epsilon_T \bar{e}\sigma_{\mu\nu} \left(1-\gamma_5\right) \nu_e \cdot \bar{u}\sigma^{\mu\nu} \left(1-\gamma_5\right) d + \tilde{\epsilon}_T \bar{e}\sigma_{\mu\nu} \left(1+\gamma_5\right) \nu_e \cdot \bar{u}\sigma^{\mu\nu} \left(1+\gamma_5\right) d \Bigg] + \text{h.c.}
\end{aligned}
\tag{1.6}
$$

where h.c. is the Hermitian conjugate of the terms listed, $\sigma_{\mu\nu} = \frac{i}{2}\left[\gamma_\mu, \gamma_\nu\right]$, $G_F/(\hbar c)^3 = 1.1663787(6)$ GeV^{-2} [31] is the Fermi coupling constant and is related to the vacuum expectation value v by $\frac{G_F}{\sqrt{2}} = \frac{e_W^2}{M_W^2} = \frac{g_2^2}{8M_W^2} = \frac{1}{2v^2}$. V_{ud} is the ud element of the Cabibbo-Kobayashi-Maskawa matrix, which represents the coupling strength of the transition from a down quark to an up quark. Currently, the most precise value of $|V_{ud}|$ is obtained from super-allowed $0^+ \rightarrow 0^+$ beta decays with

$|V_{ud}| = 0.97420 \pm 0.00021$ [31, 32]. The contributions from terms involving right handed neutrino (terms with $\tilde{\epsilon}_i$) are very small, and can be neglected [14]. The resulting lagrangian is given as:

$$\begin{aligned}\mathcal{L}_{\text{eff}} = -\frac{G_F V_{ud}}{\sqrt{2}} \Big[& \bar{e}\gamma_\mu \left(1-\gamma_5\right) \nu_e \cdot \bar{u}\gamma^\mu \left(1-(1-2\epsilon_R)\gamma_5\right) d \\ & + \epsilon_S \bar{e} \left(1-\gamma_5\right) \nu_e \cdot \bar{u} d \\ & - \epsilon_P \bar{e} \left(1-\gamma_5\right) \nu_e \cdot \bar{u}\gamma_5 d \\ & + \epsilon_T \bar{e}\sigma_{\mu\nu} \left(1-\gamma_5\right) \nu_e \cdot \bar{u}\sigma^{\mu\nu} \left(1-\gamma_5\right) d \Big] + \text{h.c.} \end{aligned} \tag{1.7}$$

Note that the operators included in the above Lagrangian are written in terms of up and down quark fields. To write any beta decay observables in terms of these BSM couplings, the corresponding neutron-proton matrix must be evaluated for each operator involved. In effect $\left\langle p \mid \hat{\mathbf{O}}_\mathbf{i} \mid n \right\rangle i \in \{\text{P, S, T, L, R}\} = g_i \left\langle u, e^-, \overline{\nu}_e \mid \hat{\mathbf{O}} \mid d \right\rangle$, where g_i is a Lorentz-invariant form factor which depends on the momenta of the proton and neutron. This was carried out in Ref. [33]. The Lagrangian of Eq. 1.7 can then be evaluated at the nucleon level and compared that of Lee and Yang in Ref. [29]. The comparison yields the following relations to the Lee-Yang coupling constants $C_i : i \in \{\text{P,V,A,S,T}\}$ [30]:

$$
\begin{aligned}
C_i &= \frac{G_F}{\sqrt{2}} V_{ud} \overline{C}_i \\
\overline{C}_V &= g_V \left(1 + \epsilon_L + \epsilon_R + \tilde{\epsilon}_L + \tilde{\epsilon}_R\right) \\
\overline{C}'_V &= g_V \left(1 + \epsilon_L + \epsilon_R - \tilde{\epsilon}_L - \tilde{\epsilon}_R\right) \\
\overline{C}_A &= -g_A \left(1 + \epsilon_L - \epsilon_R - \tilde{\epsilon}_L + \tilde{\epsilon}_R\right) \\
\overline{C}'_A &= -g_A \left(1 + \epsilon_L - \epsilon_R + \tilde{\epsilon}_L - \tilde{\epsilon}_R\right) \\
\overline{C}_S &= g_S \left(\epsilon_S + \tilde{\epsilon}_S\right) \\
\overline{C}'_S &= g_S \left(\epsilon_S - \tilde{\epsilon}_S\right) \\
\overline{C}_P &= g_P \left(\epsilon_P + \tilde{\epsilon}_P\right) \\
\overline{C}'_P &= g_P \left(\epsilon_P - \tilde{\epsilon}_P\right) \\
\overline{C}_T &= 4 g_T \left(\epsilon_T + \tilde{\epsilon}_T\right) \\
\overline{C}'_T &= 4 g_T \left(\epsilon_T - \tilde{\epsilon}_T\right)
\end{aligned}
\tag{1.8}
$$

Beta decay observables then derived in terms of the Lagrangian of Lee and Yang can thus now be written in terms of the above EFT BSM coupling coefficients.

1.2.3 The Beta Decay Distribution

A general beta decay distribution was derived in Refs. [9, 34]. For nuclei with spin $\mathbf{J}$, the distribution is given in Ref. [9] as:

$$
\begin{aligned}
w\big(\langle \mathbf{J} \rangle \mid E_e, \Omega_e\big) dE_e d\Omega_e d\Omega_\nu = \frac{F(Z, E_e)}{(2\pi)^5} p_e E_e \left(E_0 - E_e\right)^2 dE_e d\Omega_e d\Omega_\nu \times \\
\xi \left\{ 1 + a \frac{\mathbf{p_e} \cdot \mathbf{p}_\nu}{E_e E_\nu} + b \frac{m_e}{E_e} + \frac{\langle \mathbf{J} \rangle}{J} \cdot \left[A \frac{\mathbf{p}_e}{E_e} + B \frac{\mathbf{p}_\nu}{E_\nu} + D \frac{\mathbf{p}_e \times \mathbf{p}_\nu}{E_e E_\nu} \right] \right\}
\end{aligned}
\tag{1.9}
$$

Where m_e, p_e, E_e are the outgoing electron mass, momentum and energy respectively; E_0 is the endpoint energy of the beta decay spectrum; p_ν and E_ν are the

neutrino momentum and energy; and $F(Z, E_e)$ is the Fermi function which accounts for the dominant Coulomb interaction between the outgoing electron and the daughter nucleus with Z protons. For unpolarized nuclei, $\langle \mathbf{J} \rangle = 0$, and Eq. 1.9 becomes:

$$w\big(E_e, \Omega_e\big) dE_e d\Omega_e d\Omega_\nu = \frac{F(Z, E_e)}{(2\pi)^5} p_e E_e \left(E_0 - E_e\right)^2 dE_e d\Omega_e d\Omega_\nu \times \xi \left\{ 1 + a \frac{\mathbf{p_e} \cdot \mathbf{p}_\nu}{E_e E_\nu} + b \frac{m_e}{E_e} \right\} \tag{1.10}$$

Coulomb distortion and relativistic corrections were neglected in the above expressions. As such, the expression is independent of pseudoscalar coupling constants. The expressions for ξ,ξa, and ξb are given in terms of the Lee-Yang coupling constants as [9, 14]:

$$\begin{aligned} \xi = & |M_F|^2 \left(|C_V|^2 + |C'_V|^2 + |C_S|^2 + |C'_S|^2 \right) \\ & + |M_{GT}|^2 \left(|C_A|^2 + |C'_A|^2 + |C_T|^2 + |C'_T|^2 \right) \end{aligned} \tag{1.11}$$

$$\begin{aligned} \xi \times a = & |M_F|^2 \left(|C_V|^2 + |C'_V|^2 - |C_S|^2 - |C'_S|^2 \right) \\ & - \frac{|M_{GT}|^2}{3} \left(|C_A|^2 + |C'_A|^2 - |C_T|^2 - |C'_T|^2 \right) \end{aligned} \tag{1.12}$$

$$\xi \times b = \pm\, 2\gamma \mathrm{Re} \left[|M_F|^2 \left(C_S C_V^* + C'_S C'^*_V \right) + |M_{GT}|^2 \left(C_T C_A^* + C'_T C'^*_A \right) \right] \tag{1.13}$$

$\gamma := \sqrt{1 - (\alpha Z)^2}$, where α is the fine structure constant. If these expressions are evaluated at the linear level in terms of the non-standard (BSM) Lee-Yang coupling constants as in [14]:

$$\xi \approx \frac{|M_F|^2}{2} |C_V + C'_V|^2 \left(1 + |\tilde{\rho}|^2\right) \tag{1.14}$$

$$a \approx \frac{1 - \frac{1}{3}|\tilde{\rho}|^2}{1 + |\tilde{\rho}|^2} \tag{1.15}$$

$$b \approx \pm 2\gamma \frac{1}{1 + |\tilde{\rho}|^2} \mathrm{Re}\left(\frac{C_S + C'_S}{C_V + C'_V} + |\tilde{\rho}|^2 \frac{C_T + C'_T}{C_A + C'_A}\right) \tag{1.16}$$

Where $\tilde{\rho} := \frac{C_A + C'_A}{C_V + C'_V} \frac{M_{GT}}{M_F}$, which in the SM limit goes to $\tilde{\rho} \to \rho = -\frac{g_A M_{GT}}{g_V M_F}$, the Fermi/Gamow-Teller mixing ratio for the transition in consideration.

The important feature of eq. 1.16 is that the decay correlation parameter 'b', which is known as the Fierz interference term, is linear in scalar and tensor coupling constants. If one considers polarized nuclear decay or measures the polarization of the outgoing electrons, additional decay correlation parameters may be found as shown in Refs. [9, 34]. These decay correlation parameters however are either quadratic in terms of these small nonstandard Lee-Yang coupling constants, or are experimentally difficult to access (e.g. measurement of nuclear polarization, electron spin and neutrino momentum simultaneously). As such, beta spectrum measurements of unpolarized nuclei provide a relatively clean path to observing or setting bounds on possible BSM physics via the Fierz interference term. The focus of this thesis is to measure 'b' for ^{45}Ca, the details of this measurement can be found in Ch. 4.

1.3 Free Neutron Beta Decay

An especially enticing nucleus is the free neutron, as it is the most fundamental nucleus that exhibits beta decay. Since there are no other nucleons with which the decaying neutron can interact, any observables related to the process are free of the typical nuclear corrections that must be applied with more complex nuclei. As mentioned above, the most precise extractions of the CKM matrix element $|V_{ud}|$ have been achieved via super-allowed Fermi transitions. These extractions, however,

involve said nuclear structure corrections which can only be accessed computationally. In fact, the experimental precision achieved by these experiments [32, 35] has led to extractions of $|V_{ud}|$ with the predominant uncertainties arising from these corrections. The largest contributor to this uncertainty results from the transition-independent radiative correction ($\Delta_R^V = (2.361 \pm 0.038)\%$) [36]. This term is present for all beta decay transitions, including that of the free neutron. The isospin-symmetry breaking correction, with an uncertainty ranging from 0.18% to 1.62% [35], and the nuclear-structure-dependent radiative correction, however, are not present for free neutron beta decay. Hence the free neutron could provide an additional check of the value of $|V_{ud}|$ obtained from these $0^+ \rightarrow 0^+$ transitions, while carrying fewer theoretical corrections.

1.3.1 V_{ud} and ft Values

The total decay rate Γ can be obtained by integrating the differential decay rate of Eq. 1.10 over all kinematic variables:

$$\begin{aligned}
\Gamma = \frac{1}{\tau} &= \int w\big(E_e, \Omega_e\big) dE_e d\Omega_e d\Omega_\nu \\
&= \frac{1}{(2\pi)^5}\xi \int \left(F(Z, E_e) p_e E_e \left(E_0 - E_e\right)^2 \left[1 + b\frac{m_e}{E_e}\right] \right) dE_e d\Omega_e d\Omega_\nu \\
&= \frac{(4\pi)^2}{(2\pi)^5}\xi \int \left(F(Z, E_e) p_e E_e \left(E_0 - E_e\right)^2 \left[1 + b\frac{m_e}{E_e}\right] \right) dE_e \\
&= \frac{m_e^5}{2\pi^3}\xi f \left[1 + b\left\langle \frac{m_e}{E_e} \right\rangle\right]
\end{aligned} \tag{1.17}$$

where $f := \frac{1}{m_e^5}\int F(Z, E_e) p_e E_e (E_0 - E_e)^2 dE_e$, $\left\langle \frac{m_e}{E_e} \right\rangle := \frac{1}{m_e}\int F(Z, E_e) p_e (E_0 - E_e)^2 dE_e$, and τ is the mean lifetime of the transition. Note that up to this point, natural units have been used ($\hbar = c = 1$). For the sake of the following expression, these units will be explicitly written. Following the convention of [14] with $K/(\hbar c)^6 :=$

$2\pi^3\hbar\ln(2)/(m_e c^2)^5 = 8120.27649(25) \times 10^{-10}\text{GeV}^{-4}\text{s}$ [37], given the half life of the transition $t_{1/2} = \tau\ln(2)$, Eq. 1.17 can be rearranged to give the so-called ft value:

$$ft_{1/2} = \frac{K}{\xi\left[1 + b\left\langle\frac{m_e}{E_e}\right\rangle\right]} \tag{1.18}$$

In the SM limit, $\xi \to |M_F|^2 |G_F V_{ud} g_V|^2 \left(1 + |\rho|^2\right)$ and $b \to 0$, and Eq. 1.18 becomes:

$$ft_{1/2} = \frac{K}{|M_F|^2 G_F^2 |V_{ud} g_V|^2 \left(1 + |\rho|^2\right)} \tag{1.19}$$

Note that up to quadratic isospin symmetry breaking terms, $g_V = 1$ [38, 39]. For a $0^+ \to 0^+$ transition, i.e. pure Fermi transition, $M_{GT} = 0$ and $|M_F|^2 = 2$. Then in the SM limit $ft_{1/2} = \frac{K}{2G_F^2|V_{ud}|^2}$, which is constant for all $0^+ \to 0^+$ transitions. Therefore a measurement of the endpoint energy to determine f and a partial half-life and branching ratio measurement for a $0^+ \to 0^+$ transition are all that is required for an extraction of $|V_{ud}|$. In Refs. [32, 35] the authors have compiled all such ft values as well as the resulting extraction of $|V_{ud}|$.

For transitions between isobaric analog states, the number of neutrons of the parent nucleus is equal to the number of protons of the daughter nucleus. If these states are separated by a single beta decay transition, the transition is referred to as a mirror beta transition. In such cases, the total angular momentum of the initial and final state are equal. There is no net change in the total angular momentum. These transitions are referred to as "super-allowed" transitions. For such super-allowed transitions $|M_F|^2 = 1$. The ft value is then given as:

$$ft_{1/2} = \frac{K}{G_F^2 |V_{ud}|^2 \left(1 + |\rho|^2\right)} \tag{1.20}$$

In addition knowledge of the endpoint energy, partial half-life and branching ratio, an additional measurement of the mixing ratio ρ must also be performed to extract $|V_{ud}|$ for most of these mirror transitions. In the decay of the free neutron, $|M_{GT}|^2 = 3$. Then the ft value (again in the SM limit) becomes:

$$ft_{1/2} = f\ln(2)\tau_n = \frac{K}{G_F^2\left|V_{ud}\right|^2(1+3\lambda^2)} \tag{1.21}$$

with $\lambda = \left|\frac{g_a}{g_v}\right|$ and the neutron mean lifetime is given as τ_n. Then solving for $|V_{ud}|^2$ yields:

$$\left|V_{ud}\right|^2 = \frac{K}{G_F^2 f\ln(2)\tau_n(1+3\lambda^2)} \tag{1.22}$$

In this case, the masses of the decay products are known thus the enpdoint energy $E_0 = (m_n - m_p - m_e)c^2 = 939.5654133(58)\text{MeV} - 938.2720813(58)\text{MeV} - 0.5109989461(31)\text{MeV} = 782.234(16)$ keV [31, 40, 41]. Thus only two measurements are required to extract $|V_{ud}|$ via free neutron beta decay: a measurement of the neutron lifetime τ_n and a measurement of the hadronic ratio λ.

A brief note: for the sake of clarity, the above derivations and expressions do not include the typical corrections to the ft values as outlined in Ref. [35]. The isospin-symmetry-breaking correction is noted as δ_C, the transition independent radiative correction is Δ_R^V, and the transition dependent corrections are δ_R' and δ_{NS}. Then applying these corrections the ft value becomes [35]:

$$(ft)_{corr.} = \frac{(ft)_{\text{above}}}{(1+\delta_R')(1+\delta_{NS}-\delta_C)(1+\Delta_R^V)} \tag{1.23}$$

1.3.2 The status of τ_n and λ

The first dedicated measurements of the neutron lifetime τ_n were published in 1950 and superseded by a result with higher statistics in 1951 [42, 43]. These findings placed $\tau_n \sim 18$ minutes $\pm$ 3.6 minutes. There have been many measurements of the

lifetime since these first experiments and the Particle Data Group (PDG) value of the lifetime is $\tau_n = 880.2 \pm 1.0$s [31]. Despite this apparently benign uncertainty of $\sim 0.1\%$, the different methods by which τ_n has been measured are not self-consistent. The current discrepancy is at the level of 4σ. The two primary methods used to measure the neutron lifetime are referred to as the beam and the bottle method respectively.

Bottled neutron lifetime measurements

The premise of a neutron bottle measurement is as follows, a container is filled with some number of neutrons N_0, which in general is not known. The the number of neutrons remaining in the bottle after some time t_1 is measured as N_1. The bottle is again filled to N_0, and the number of neutrons after some time t_2 is measured as N_2. The number of neutrons within the bottle written as a function of time is given as:

$$N(t) = N_0 e^{\frac{-t}{\tau_s}} \tag{1.24}$$

where the storage lifetime τ_s is related to the neutron lifetime τ_n and neutron loss rate τ_l via $\tau_s^{-1} = \tau_n^{-1} + \tau_l^{-1}$. Then the storage time can be expressed as $\tau_s = \frac{\Delta t}{\ln\left(\frac{N_1}{N_2}\right)}$, where $\Delta t = t_2 - t_1$. The lifetime is given as:

$$\begin{aligned} \tau_n &= \frac{\tau_s}{1 - \frac{\tau_s}{\tau_l}} \\ &\approx \tau_s \left(1 + \frac{\tau_s}{\tau_l} + \left(\frac{\tau_s}{\tau_l}\right)^2 + \cdots\right) \end{aligned} \tag{1.25}$$

In reality, there are many loss mechanisms which contribute to τ_l. These include neutron scattering from the bottle due to bottle walls, residual gas scattering, and vibrational excitations from the bottle. All loss mechanisms must be accurately modeled and thus can lead to substantial corrections, as large as 10% of the storage time [44]. Because material interactions tend to increase as a function of neutron

energy, ultra-cold neutrons (UCNs) with kinetic energies on the order of a few neV are generally used in confinement experiments. The first iterations consisted of UCN traps with material walls to confine the neutrons [45, 46]. More recently, magnetic confinement of the UCNs has also been achieved [47, 48], which reduces losses and loss uncertainties due to interactions with the trap walls.

Neutron beam lifetime measurements

The other technique used to measure the neutron lifetime is the "beam" method. A beam of neutrons is passed through an electromagnetic proton trap.The number of protons found in the trap is counted. The number of neutrons per unit time is measured at two different points along the beam. The ratio of these two rates can then be used to extract the lifetime. The proton counter is used to measure the rate at one point, and a neutron flux monitor placed further downstream (further along the direction of neutron propagation along the beam) measures the rate at another. Then given adequate knowledge of detection efficiencies, the neutron lifetime can be extracted by taking a ratio of these two rates. The technical details of this type of measurement can be found in Ref. [49].

$\mathbf{V_{ud}}$ $\tau_{\mathbf{n}}$ and λ

Returning to the discussion of V_{ud} in the context of neutron decay, it is more convenient to rewrite the uncertainty of $|V_{ud}|$ of Ref. [35] as $\frac{\delta(|V_{ud}|^2)}{|V_{ud}|^2}$. This is obtained by:

$$\begin{aligned}\frac{\delta(|V_{ud}|^2)}{|V_{ud}|^2} &= \frac{\partial}{\partial|V_{ud}|}(|V_{ud}|^2)\delta(|V_{ud}|)|V_{ud}|^{-2} \\ &= 2\frac{\delta(|V_{ud}|)}{|V_{ud}|} \\ &= 4.311 \cdot 10^{-4} \end{aligned} \tag{1.26}$$

The the uncertainty of $|V_{ud}|^2$ is given by $\delta(|V_{ud}|^2) = \left[\sum_i \left(\frac{\partial|V_{ud}|^2}{\partial x_i}\delta x_i\right)^2\right]^{1/2}$ where the sum is carried out over all measured quantities x_i. Then using the expression given in Eq. 1.22, including the additional radiative corrections, the uncertainty is given as:

$$\frac{\delta(|V_{ud}|^2)}{|V_{ud}|^2} = \Big[\left(\frac{\delta K}{K}\right)^2 + \left(2\frac{\delta G_F}{G_F}\right)^2 + \left(\frac{\delta(1+\Delta_R^V)}{1+\Delta_R^V}\right)^2 \left(\frac{\delta(f(1+\delta_R')}{f(1+\delta_R')}\right)^2 + \left(\frac{\delta\tau_n}{\tau_n}\right)^2 + \left(\frac{6\lambda\delta\lambda}{1+3\lambda^2}\right)^2\Big]^{1/2} \tag{1.27}$$

Note that $\frac{\delta K}{K} \sim 1.11\cdot10^{-7}$ and $\frac{\delta G_F}{G_F} \sim 5.1\cdot10^{-7}$. The value of $\frac{f(1+\delta_R')}{f(1+delt_R')} = 5.25\cdot10^{-5}$ is taken from Ref. [50], $\left(\frac{\delta(1+\Delta_R^V)}{(1+\Delta_R^V)}\right) = 3.712\cdot10^{-4}$ is from [36], and the value of $\lambda = -1.2783(22)$ was obtained from Ref. [51, 52]. Substituting these into the above:

$$\frac{\delta(|V_{ud}|^2)}{|V_{ud}|^2} \sim \Big[1.37\cdot10^{-7} + 1.70\cdot(\delta\lambda)^2 + \left(\frac{\delta\tau_n}{\tau_n}\right)^2\Big]^{1/2} \tag{1.28}$$

The first two values were intentionally separated in Eq. 1.28 to illustrate that the dominant uncertainty (second term) arises from λ and the sum of all others (with the exception of the neutron lifetime) contribute to a value less than $2\cdot10^{-7}$. Then if an extraction of $|V_{ud}|$ via the free neutron is to be competitive with those of the super-allowed Fermi transitions, Eq. 1.28 must be comparable to the value 1.26. This gives the following relation:

$$1.70\cdot(\delta\lambda)^2 + \frac{\delta(\tau_n)^2}{(\tau_n)^2} < 4.8\cdot10^{-8} \tag{1.29}$$

The current precision of the best lifetime measurements is limited to $\delta\tau_n \sim 1$s [48, 53]. Thus a competitive extraction of $|V_{ud}|$ is not possible, regardless of the precision in λ. Next generation lifetime measurements, however, are currently projecting an

uncertainty on the level of about 0.1s. At this level, a competitive extraction of $|V_{ud}|$ is feasible. With a lifetime of about 880s and a 0.1s uncertainty, a competitive $|V_{ud}|$ can be obtained via the free neutron, provided a measurement of λ with an uncertainty of $\delta\lambda < 10^{-4}$.

Chapter 2

Overview of the Nab Experiment

2.1 Introduction

The intent of the Nab experiment is to measure the electron-neutrino correlation parameter 'a' and the Fierz interference term 'b' of Eq. 1.10 for the free neutron. As outlined in the 2007 proposal, the anticipated precision is $\frac{\delta a}{a} \sim 10^{-3}$ and $\delta b \sim 10^{-3}$ [54, 55]. Assuming maximal parity violation ($C_i = C_i'$; for $i \in \{\mathrm{V}, \mathrm{A}\}$) and given that $|M_{GT}|^2 = 3$ and $|M_F| = 1$ for the free neutron, the expression for 'a' of Eq. 1.14 becomes $a = \frac{1-\lambda^2}{1+3\lambda^2}$, where the hadronic mixing ratio $\lambda := |g_A/g_V|$. Hence Nab will be set a limit on λ with a precision of $\frac{\delta\lambda}{\lambda} \sim 2.7 \cdot 10^{-4}$; nearly an order of magnitude more precise than any value of λ listed by the PDG [31]. A measurement of the Fierz interference term at the $\delta b \sim 10^{-3}$ level would be competitive with the most stringent limits on Fierz interference set by the BSM ft values measured for super-allowed $0^+ \to 0^+$ Fermi transitions (see Ch. 6 for a discussion of past and ongoing Fierz searches).

Such a measurement will be achieved by utilizing a custom 7 meter tall magnetic spectrometer described in Sec. 2.3. The magnet is situated on the Fundamental Neutron Physics Beamline (FnPB) of the Oak Ridge National Laboratory (ORNL) Spallation Neutron Source (SNS). Beta decay particle energies will be measured with

thick, large-area, pixelated, single-crystal silicon detectors, which are detailed in Sec. 4.3.1.

2.2 Principles of the Nab measurement

2.2.1 The electron-neutrino correlation parameter: 'a'

Recall from Eq. 1.9, the triple differential decay rate for free neutrons is given as:

$$w\big(\langle \mathbf{J}\rangle \mid E_e,\Omega_e\big)dE_e d\Omega_e d\Omega_\nu = \frac{F(Z,E_e)}{(2\pi)^5} p_e E_e \left(E_0 - E_e\right)^2 dE_e d\Omega_e d\Omega_\nu \times \tag{2.1}$$
$$\xi\left\{1 + a\frac{\mathbf{p_e}\cdot\mathbf{p}_\nu}{E_e E_\nu} + b\frac{m_e}{E_e} + \frac{\langle \mathbf{J}\rangle}{J}\cdot\left[A\frac{\mathbf{p}_e}{E_e} + B\frac{\mathbf{p}_\nu}{E_\nu} + D\frac{\mathbf{p}_e\times\mathbf{p}_\nu}{E_e E_\nu}\right]\right\}$$

In the above equation, $\langle \mathbf{J}\rangle$ is the expectation value for the spin of the neutron. $\boldsymbol{p_e}$ and E_e represent electron momentum and energy respectively. Similarly $\boldsymbol{p_\nu}$ and E_ν represents the anti-neutrino momentum and energy. For an unpolarized ensemble of neutrons, $\langle \mathbf{J}\rangle = 0$ and eq 2.1 simplifies to Eq. 1.10:

$$w\big(E_e,\Omega_e\big)dE_e d\Omega_e d\Omega_\nu = \frac{F(Z,E_e)}{(2\pi)^5} p_e E_e \left(E_0 - E_e\right)^2 dE_e d\Omega_e d\Omega_\nu \times \tag{2.2}$$
$$\xi\left\{1 + a\frac{\mathbf{p_e}\cdot\mathbf{p}_\nu}{E_e E_\nu} + b\frac{m_e}{E_e}\right\}$$

Now $\boldsymbol{p_e}\cdot\boldsymbol{p_\nu} = p_e p_\nu cos(\theta_{e\nu})$, where $\theta_{e\nu}$ represents the opening angle between the electron and anti-neutrino momenta. For the FnPB, neutron momentum (p_n) ranges from 60 eV/c to 2.5 keV/c [56]. Since $m_n \sim 939$ MeV/c^2, the total energy of the neutron can be approximated as $E_n = ((m_n c^2)^2 + (p_n c)^2)) \approx m_n c^2$. The neutron momentum is effectively zero with respect to that of the daughter particles: the electron, proton (p_p), and anti-neutrino. Therefore from momentum conservation:

$-\boldsymbol{p_p} = \boldsymbol{p_e} + \boldsymbol{p_\nu}$, so squaring both sides and solving for $cos(\theta_{e\nu})$ gives:

$$cos(\theta_{e\nu}) = \frac{p_p^2 - p_e^2 - p_\nu^2}{2p_e p_\nu} \tag{2.3}$$

From energy conservation, $E_n = E_p + E_e + E_\nu$, where $E_n \sim m_n c^2$. Note that $E_\nu = (m_\nu^2 c^4 + p_\nu^2 c^2)^{1/2} \sim p_\nu c$, since $m_\nu^2 c^4 < 0.6eV^2$ [37]. Therefore solving the energy relation for E_ν yields $p_\nu c = E_n - E_p - E_e$. Then substituting for p_ν in eq. 2.3:

$$cos(\theta_{e\nu}) = \frac{p_p^2 - p_e^2 - (E_n - E_p - E_e)^2}{2p_e(E_n - E_p - E_e)} \tag{2.4}$$

Substituting $E_n = m_n$ in the above expression for $\cos(\theta_{e\nu})$ and $p_\nu c = E_n - E_p - E_e$ into Eq. 2.2 gives:

$$\frac{dw}{dE_e d\Omega_e d\Omega_\nu} \propto p_e E_e (E_0 - E_e)^2 \left(1 + a\frac{p_p^2 - p_e^2 - (m_n - E_p - E_e)^2}{2E_e\,(m_n - E_p - E_e)} + b\frac{m_e}{E_e}\right) \tag{2.5}$$

Now for a fixed electron energy, eq. 2.5 can be written as:

$$\frac{dw}{dE_e d\Omega_e d\Omega_\nu} \propto C_{1,e}\left(a\frac{p_p^2 - p_e^2 - (m_n - E_p - E_e)^2}{2E_e\,(m_n - E_p - E_e)} + C_{2,e}\right) \tag{2.6}$$

Note that $C_{1,e}$ and $C_{2,e}$ are simply constants for a fixed E_e, and $E_p = m_p c^2 + T_p \approx m_p c^2$ (see Appendix A). Thus the only varying quantity in the above expression for fixed E_e is the squared proton momentum. Then 'a' can be extracted for neutron beta decay by measuring the proton momentum (specifically p_p^2) distribution at various fixed electron energies E_e (see Fig. 2.1 for an *ideal* proton momentum spectra). The extraction of 'a' in Nab will be achieved by measuring the electron energy directly and measuring the proton momentum via time of flight (ToF) analyses for coincident proton-electron events.

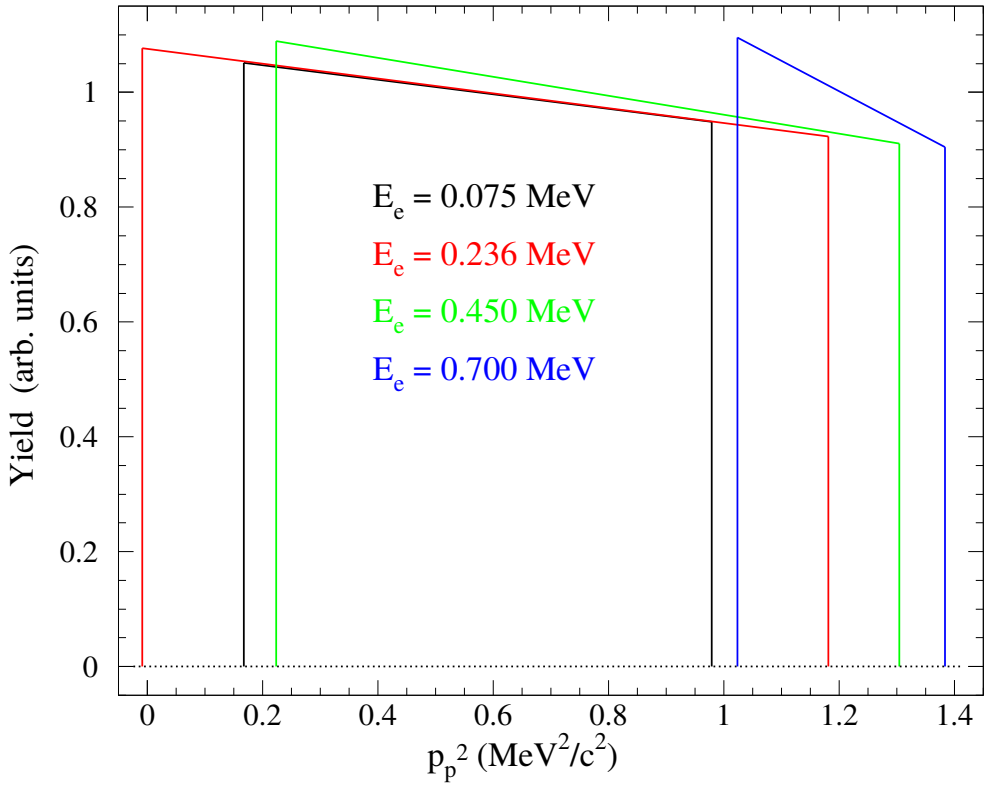

Figure 2.1: Above is the squared proton momentum distribution at various electron energies. These are simulated ideal spectra.

2.2.2 The Fierz interference term for the free neutron

A brief overview of the measurement of the Fierz interference term for Nab will be discussed below. A more detailed discussion may be found in Ch. 4.

If Eq. 2.2 is integrated over the electron and neutrino solid angles $d\Omega_e$ and $d\Omega_\nu$, the result is given as:

$$w\big(E_e\big)dE_e = \frac{F(Z,E_e)}{2\pi^3} p_e E_e \left(E_0 - E_e\right)^2 \xi \left(1 + b\frac{m_e}{E_e}\right) dE_e \tag{2.7}$$

The Fierz interference term is proportional to scalar and tensor (BSM) couplings. These operators are absent in the SM, hence 'b' may be extracted by measuring the free neutron beta decay spectrum and comparing it to that predicted by the SM. Instead of detecting coincident proton-electron events as above for an electron-neutrino correlation measurement, a measurement of 'b' will be achieved for Nab simply by collecting all outgoing electrons, which minimizes distortions resulting from uncaptured backscattered events. See Fig. 2.2 for the effect of various values of 'b' on the electron energy spectrum.

2.3 Spectrometer & Detector Mount

A schematic of the Nab spectrometer as well as its ideal magnetic field map can be found in Fig. 2.3. The asymmetric design of the magnet extends the length of the proton flight path, minimizing energy uncertainty in ToF analyses. The basic operating principle of the spectrometer is as follows. Neutrons enter the decay volume of the spectrometer, and some decay into a proton, electron, and electron antineutrino (the latter of which is not detected). The magnetic field guides charged decay products to the silicon detectors at the top and bottom of the spectrometer. Any protons with downward directed momentum are rejected. The 4T field spike just above the decay volume creates a magnetic mirror. Protons with large angles between their momenta

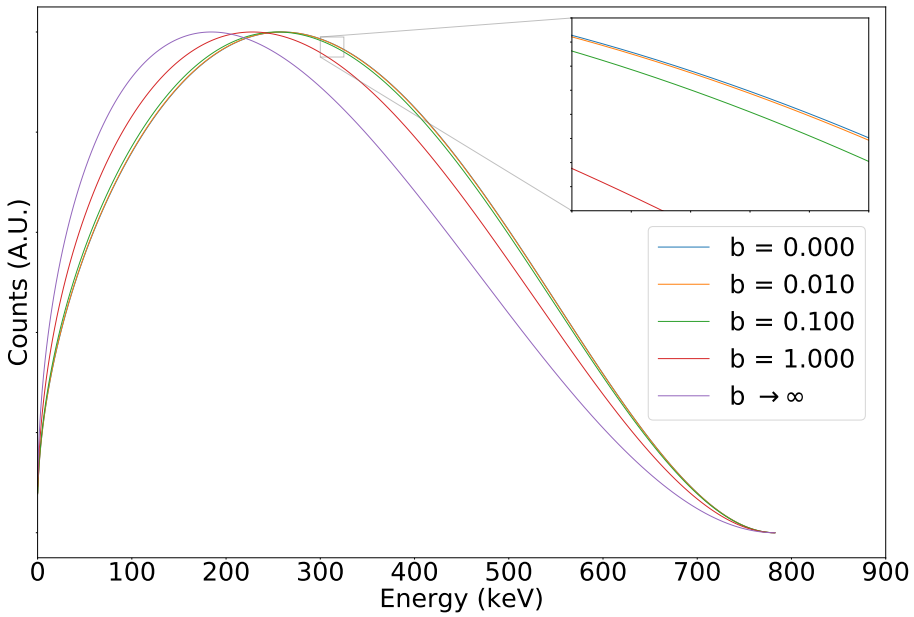

Figure 2.2: Above is the electron energy spectrum from neutron beta decay for various values of the Fierz interference term.

and the magnetic field are reflected downward and also rejected. The protons with sufficiently small angles pass through the "pinch" region and are subjected to a field expansion region. The magnetic field rapidly decreases from 4 T to 0.2 T. This change adiabatically longitudinalizes the proton momentum in the direction of the upper detector and allows for a momentum extraction via $|p_p| \propto \frac{1}{\mathrm{ToF}}$. At the end of the ToF region, the charged particles are subjected to a -30 kV accelerating potential. This acceleration provides the protons with enough energy to be measured by the silicon detector. The electron energies are measured directly, by either detector. The projected goal is to measure the proton ToF with a 100 ps timing resolution and electron energies with a resolution of a few keV.

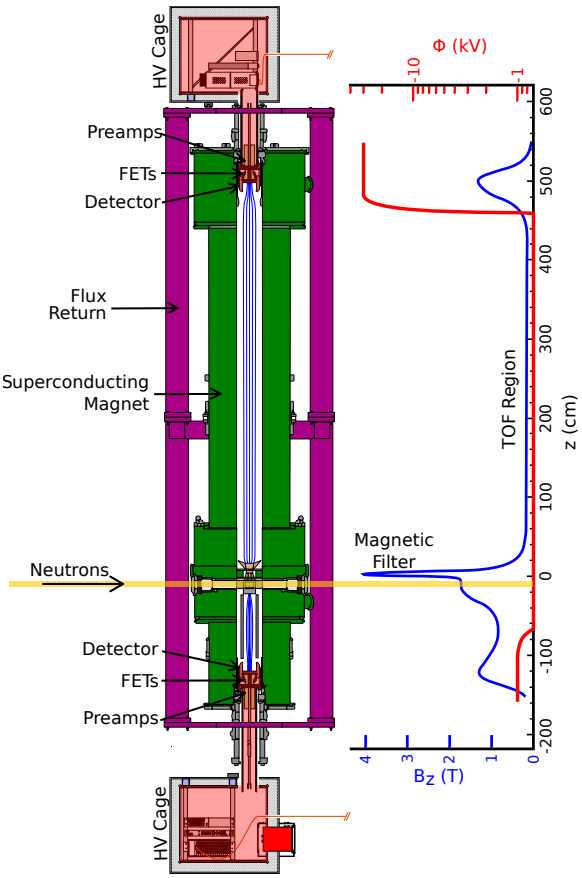

Figure 2.3: In the above schematic of the Nab spectrometer, the neutron beam enters the spectrometer from the left. Some portion of the neutrons decay within this fiducial volume and the decay particles are constrained by the magnetic field of the spectrometer. Upward-going protons with sufficiently small opening angles between their momentum and the magnetic field enter a ToF region where the magnetic field rapidly changes from 4T to $\sim 0.2T$. This adiabatically redirects the proton mometum such that it is nearly normal to the face of the silicon detector upon entry.

Chapter 3

Temperature Stabilization for the Nab Experiment

3.1 Introduction

Reaching a precision of $\frac{\delta a}{a} \sim 10^{-3}$ requires an energy resolution of a few keV and a timing resolution on the order of 100 ps. Much of the system resolution is dictated by the amplifying and digitizing electronics used, however a well controlled and stable detector temperature is also critical to achieve these specifications. A terse discussion of solid state detector characteristics will be presented here only to provide motivation for the rest of the chapter. For a more detailed discussion, see Ch. 4. As with any solid state particle detector, a decrease in temperature reduces the probability of thermal excitation of charge carriers across the band gap, i.e. a reduction of thermal noise [57]. The additional benefit to a lower detector temperature is better position sensitivity. As a charged particle interacts with the silicon, some number of electron-hole pairs proportional to the energy of the incident particle are liberated. This charge diffuses through the detector, thereby reducing the position resolution. The diffusion of charge through the detector depends linearly on the temperature of the detector [57]. Then by reducing the temperature of the detector,

the uncertainty in deposition location is also reduced. This is particularly important for event reconstruction as position information can be used in the identification of backscattered or coincident proton-electron events. Although lowering the detector temperature leads to a noise reduction, it is possible for the detector to be too cold. The phenomenon known as carrier freeze out occurs when the temperature of the semiconductor reduces charge mobility and effectively freezes electrons or holes to the impurity site. Typically at higher temperatures, the impurity is thermally ionized, and the charge carrier contributes to the overall carrier concentration. At freeze out temperatures, the carrier cannot be thermally ionized and is bound to the donor or acceptor impurity site. The net effect reduces the donor or acceptor concentration, and the n or p-type carrier concentration approaches that of the intrinsic semiconductor [58, 59]. A more detailed discussion of the detector properties can be found in Sec. 4.3.1. In addition to cooling the silicon detector, the cooling system also controls the temperature of the accompanying electronics. Temperature stability in within these sensitive amplifying and shaping chains is essential as temperature fluctuations can result in an amplifier gain shift . Consequently a cooling system for Nab has been carefully designed and tested to ensure precise temperature control.

3.1.1 Nab Cooling System Design

A schematic of one of the two identical Nab cooling loops can be seen in Fig. 3.1. The system operates by circulating helium gas around a closed circuit. The primary pump is a custom KNF N1400 project pump, which moves helium around the loop. The mass flow of the gas is regulated by an MKS GE250 mass flow controller. After traveling through the mass flow controller, the gas is then cooled with Sumitomo CH-110 cold head and custom heat exchanger (see Fig. 3.2). The heat exchanger is comprised of a stack of oxygen-free high thermal conductivity (OFHC) copper disks and spacers on a threaded rod. Each disk has an offset 1/4" hole through which the gas travels. Neighboring disks are rotated by 180° with respect to one another to

ensure the maximum distance between these holes. This orientation maximizes the path length of the gas through the exchanger, which in turn maximizes the cooling power delivered to the gas.

Temperature control and stabilization is achieved with two separate heaters. The Sumitomo cold head operates at 20K, however the detector optimally operates at a warmer temperature. To raise the temperature of the cold head (and therefore the helium coolant) one heater is fixed to the cold head and allows for a 20K-100K temperature range. Separate, in-line cartridge heaters allow for the fine adjustment and stabilization of the helium temperature . By utilizing a temperature sensor down stream of the heater, a PID feedback loop is implemented, which allows for very precise temperature control, given a reasonable choice of PID parameters.

The cold gas is transported to the high voltage (HV) cage in $\sim$ 45' long, vacuum jacketed, flex line. As shown in Fig. 2.3, there is a high voltage cage for the detectors at the top and the bottom of the spectrometer. Since the inner portion of the HV cage is maintained at a 30 kV potential with respect to the outer (grounded) cage, a custom electrically and thermally insulated feedthrough was designed and fabricated to pass the gas into the high voltage cage (see Fig. 3.3). From there, the gas travels through a custom bayonet which mates with the detector mount. As can be seen in Fig. 3.4, the gas travels through the mount providing cooling to both the field effect transistor (FET) circuits and the detector itself. The FET circuits are responsible for the first stage of amplification of the detector signal, and are fairly sensitive to temperature fluctuations. After exiting the detector mount and HV cage (via a second identical HV feedthrough), the gas is warmed back up using a room temperature heat exchanger, as the specifications of the KNF pump require that the gas temperature be above 0^oC at the pump inlet.

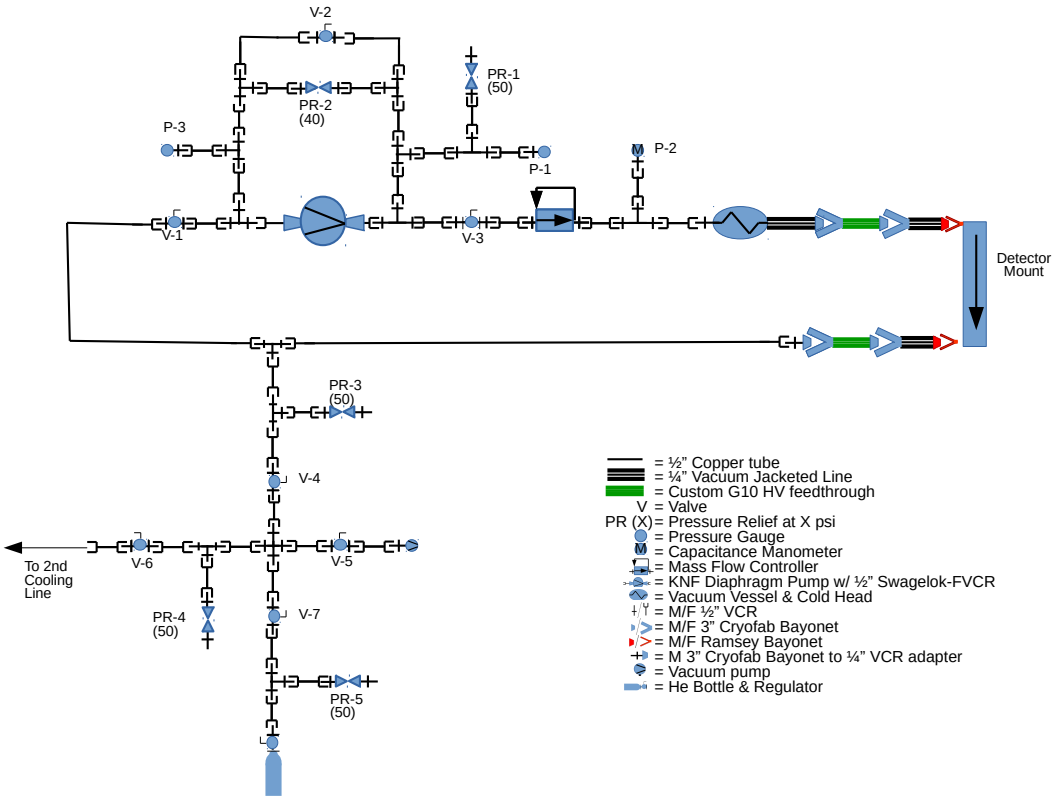

Figure 3.1: There will be two such cooling loops for the Nab experiment: one for the upper detector and one for the lower detector.

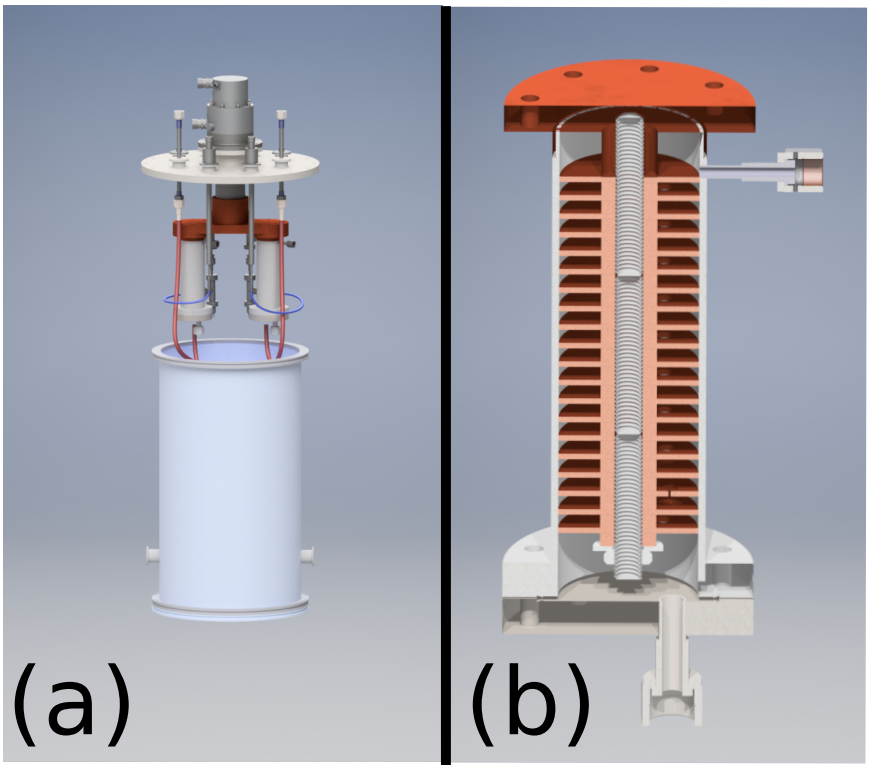

Figure 3.2: (a) A model of the vacuum vessel and cooling components within. Warm gas enters the volume via standard KF40 feedthroughs. The gas travels through steel-braided flex line (red) and enters a heat exchanger. After being cooled and passing PID loop components, the cold gas travels along more flex line (blue) and exits the chamber. **(b)** A half section view of the heat exchanger. The gas enters at the bottom and travels upwards towards the cold head.

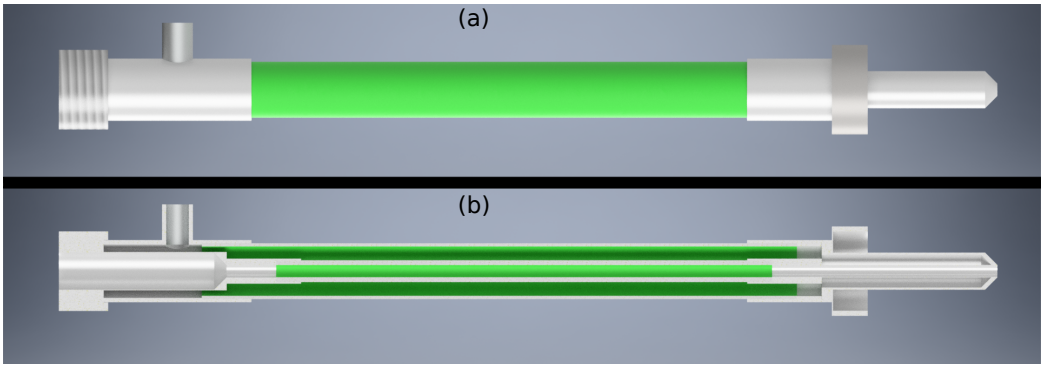

Figure 3.3: (a) A model of the high voltage feedthrough. A Cryofab transfer line connects to the bayonet on the left, which is at ground. The gas travels through vacuum jacketed G-10 line and enters the high voltage cage (30 kV). **(b)** A half section view of the feedthough. The space between the two G10 lines (green) is vacuum. The electrically insulating properties of the G10 and the vacuum between the two G10 lines provides the electrical and thermal insulation.

3.2 LANL Prototyping

The UCNB [61] and ^{45}Ca experiments (see Chapter 4) share experimental approaches with Nab [62] and have served as a prototyping platform for various Nab subsystems, including the cooling system. These experiments were conducted in Area B of the Los Alamos Neutron Science Center (LANSCE) of the Los Alamos National Laboratory. The earliest implementations of the cooling system consisted of a very rudimentary LN_2 based system. Taking into consideration the problems brought about by LN_2 cooling, helium based prototypes were designed and tested for subsequent UCNB and ^{45}Ca runs.

3.2.1 Liquid Nitrogen (LN_2) Cooling

The original cooling system designed for the UCNB mount was a LN_2 based cooling system, whereby the silicon detectors were cooled by passing LN_2 through the UCNB detector mount. Very rough flow control was provided by the globe valve on the LN_2 dewar. The simplicity of the system required very little custom infrastructure,

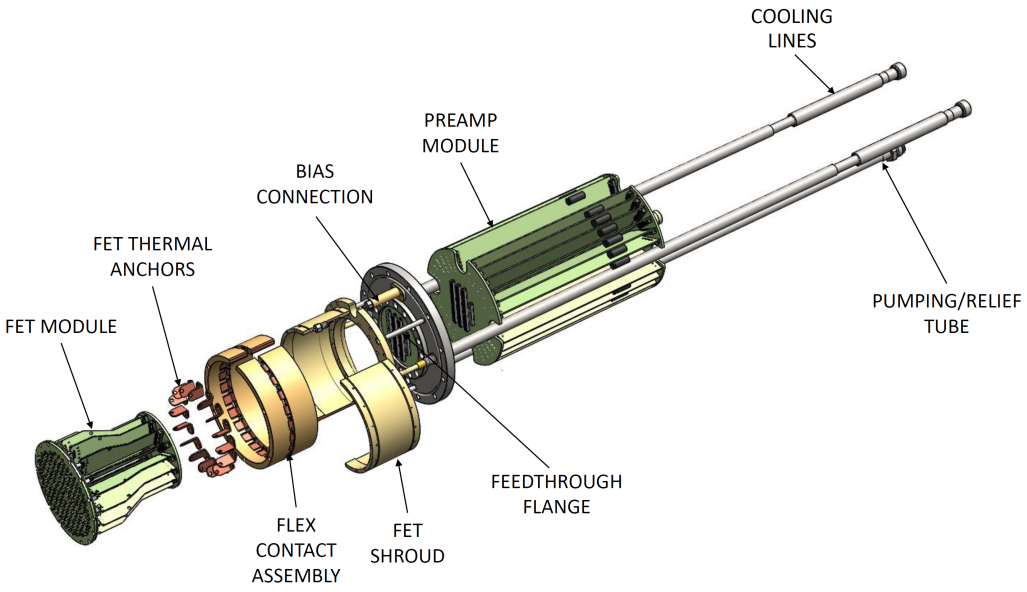

Figure 3.4: Shown above is an exploded view of a Nab detector mount courtesy of Ref. [60]. The detector (not pictured) mates with the pogo-pin board to the left of the Fet module assembly. The cold helium gas enters the mount's vacuum jacketed cooling lines labeled above. The FET volume (to the left of the Feedthrough Flange) is maintained at vacuum ($\sim 10^{-6}$ Torr). The helium circulates around the gold plated copper FET shroud. The FET thermal anchors tie the shroud and FET cards together. The detector is cooled by direct contact with the FET shroud and Flex Contact Assembly.

however there were some aspects that affected data taking during UCNB and early ^{45}Ca running.

For one, the finite volume of the LN_2 dewars paired with relatively poor insulation of the transfer lines required expeditious and frequent refilling. In addition to the time lost due to the filling, data taking also suffered lost time to re-cooling the detectors which warmed during the filling process. The magnet in which the ^{45}Ca and UCNB experiments were conducted (the SCS [51]) is a warm bore magnet. Without active cooling over a span of 30 minutes, the detector temperature can rise by $\sim$ 25K.

Secondly, frequent oscillations in detector baseline were observed and attributed to the LN_2 system. The waveform in Fig. 3.5 exhibits the typical baseline oscillation attributed to LN_2 microphonics. These oscillations were caused by the physical shaking of the cooling lines which, due to their proximity to the electronics chain, created vibrations along the FETs and/or preamps. This baseline oscillation degraded energy resolution and created a need for larger (higher energy) trigger thresholds, see Chapter 5 for more detail. Although switching to relatively high flow rates of LN_2 slightly reduced the amplitude of these oscillations, the problem still persisted and caused a loss in energy resolution.

3.2.2 Cold He gas cooling at LANSCE

Two prototypes for the Nab cooling system were studied at LANSCE. The goal of the first prototype was to provide a proof of principle for a helium based cooling system for a UCNB/Nab style detector mount. The second iteration was used to study the achievable temperature stability of a helium cooled system.

The first He cooled prototype

A following set of data was taken where a circulating loop of cold helium gas was used instead of LN_2 to cool the detector system (see Fig. 3.6). This implementation consisted of a room temperature helium supply and around 20 feet of coiled ½" tubing

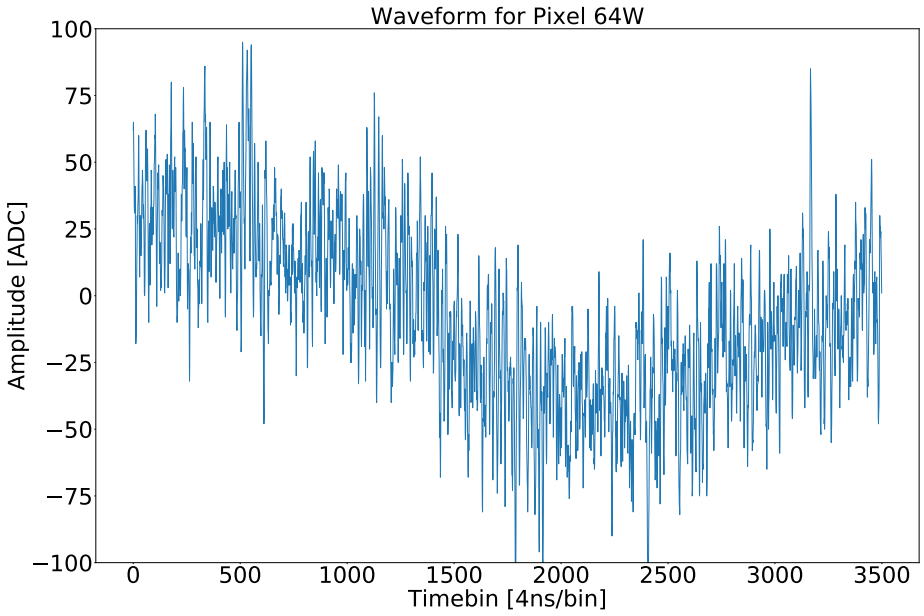

Figure 3.5: Shown above is baseline data, taken from the central pixel of the West detector. In the absence of microphonics, the signal is flat with a $\sigma_{\text{rms}} \sim 20$ ADC. For reference, a 16 keV event corresponds to a signal of 100 ADC. Not only do these oscillations necessitate higher trigger thesholds, but also give rise to distortions in extracted energy and create additional energy uncertainties. See Sec. 5.1.4 for more discussion.

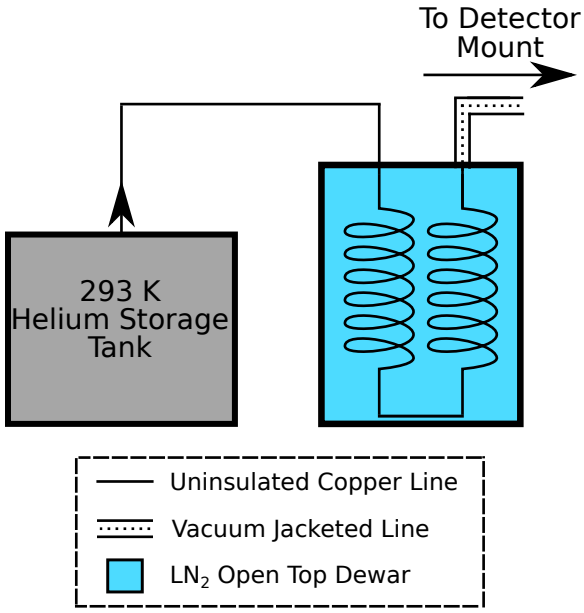

Figure 3.6: Shown above is the basic premise for the first prototype of a helium cooled system. Room temperature helium was cooled down in an LN_2 bath, and the cooled gas was transported to the detector mount via vacuum jacketed lines.

submerged in LN_2. The mass flow was regulated by an in-line MKS flow controller on the warm gas side, upstream of the LN_2 bath. The gas then traveled to the detector mount via vacuum jacketed flex line. The temperature was monitored at five points of interest within the detector mount (see Fig. 3.7). Three different mass flow rates were chosen: 60,80, and 100 standard liters per minute (SLM) all at roughly 35 PSIG. The resulting temperature data (i.e. cooling rate and temperature profile) was compared to that of previous cooling runs.

As can be seen in Fig. 3.8, LN_2 brought the detector mount to the coolest temperatures. This was to be expected since the mass flow rate of LN_2 was much greater and the input temperature much lower than that of the gaseous helium at any of the observed flow rates. In terms of stability, the helium gas cooling performed better than LN_2 cooling. With LN_2 cooling, the uncertainty of the baseline temperature of the copper can cooling the FETs and detector was 0.78K over 3 hours. For helium delivered at 100 SLM, the uncertainty was 0.58K over 3.5 hours. Ideally,

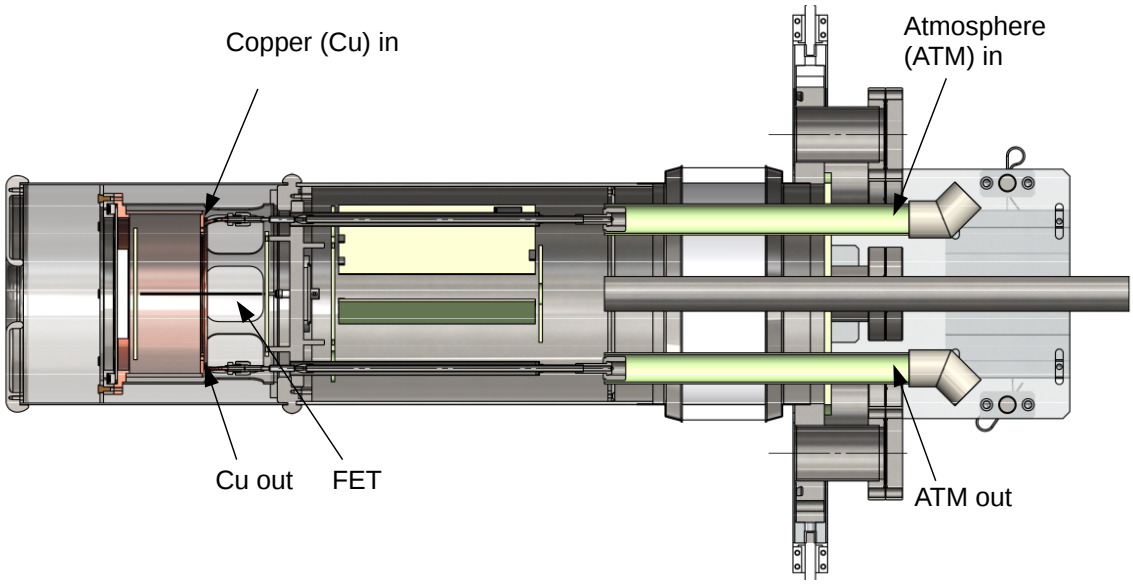

Figure 3.7: The temperature was measured at ATM In, ATM Out, Cu In, Cu Out, & FET.

Table 3.1: Although with helium cooling the peak does broaden, the peak location is consistent to 1 σ.

Flow Rate (Type)	**Counts**	**Mean (keV)**	**Width (keV)**
LN_2	$4.92{\cdot}10^5$	$80.95 \pm 0.56_{\text{stat}}$	4.83
80 SLM He	$4.84{\cdot}10^5$	$81.29 \pm 0.61_{\text{stat}}$	5.21
100 SLM He	$4.65{\cdot}10^5$	$81.19 \pm 0.61_{\text{stat}}$	5.15

a range from 100-200 SLM of cold helium would have been desirable, however the requisite equipment to do so was not available.

In addition to providing a proof of principle for the designed Nab cooling system, this helium cooled setup was also used to monitor gain drift of the front end electronics as a function of temperature. A ^{133}Ba source was placed in front of the detector. As will be detailed further in Chapter 4, the source spectra provide multiple sets of conversion electrons as well as X-ray lines with well known energies. These spectral lines were fitted to gaussians for various cooling setups, and peak widths (σ_{gaussian}) and peak locations (μ_{gaussian}) were ascertained from the fits. Any gain drift would be indicated by a shift in a given peak's location, and energy resolution of the system can be determined from the widths. These widths and locations were also compared to those of LN_2 cooled data. Despite the lower flow rates and therefore higher temperatures, the locations (μ) for the ^{133}Ba 80 keV peak fits were consistent to 1σ (see table 3.1). The peak widths for the helium cooled system however were 6-7% larger than those of LN_2. The peak broadening due to a slightly warmer detector and accompanying electronics chain temperature was to be expected. The secondary goal of this testing was to begin to quantify any gain drift brought about by warmer temperatures. From the above, we conclude that if there is any gain drift of the front amplification, it is beyond our sensitivity.

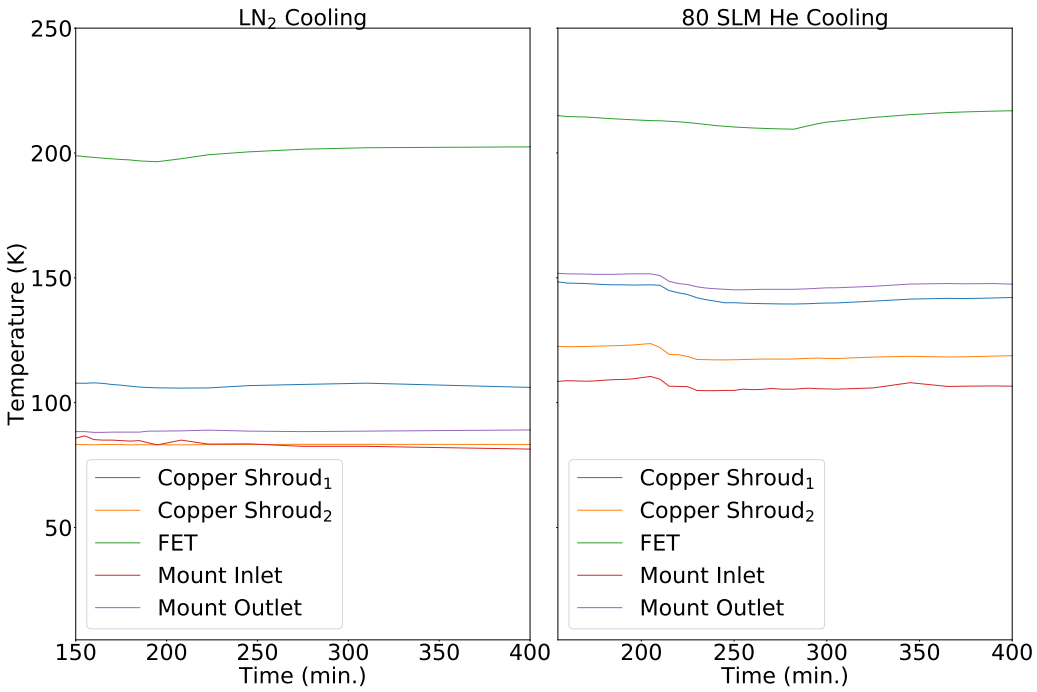

Figure 3.8: The overall temperature profile of the detector mount was colder for LN_2 cooling than that cooled via He, however the temperature stabilities proved to be comparable.

The second He cooled prototype

In the late spring/early summer of 2017, more sophisticated tests were conducted at LANSCE to demonstrate temperature stability for a cooling system similar to that of Nab. These data were taken just prior to the 2017 ^{45}Ca data set, and the prototype cooling system was then implemented for ^{45}Ca production data taking. Instead of using a room temperature helium supply, the exhaust from a helium liquefier in Area B was used to cool the system. At the detector mount inlet, the helium temperature was measured to be 40-50K. Similar to the Nab design, the temperature control and stability were achieved using an in-line cartridge heater in tandem with an in-line temperature sensor, all monitored and controlled by a Lakeshore 336 temperature controller. The controller then operated as a tuned PID feedback loop to maintain a constant detector temperature. Temperature sensor locations can be found in Fig. 3.9. Temperature profiles for the above setup were compared to those of an LN_2 cooled system, with an emphasis on stabilities at various points along the mount. The goal of the study was to benchmark temperature stability provided by helium gas at a much colder temperature, closer to that of the Nab design.

Temperature stability proved to be challenging to demonstrate with LN_2. For one, the mass flow rate was too large for a 100W heater to regulate. Secondly, most of the heat transferred to the gas was lost to the latent heat of vaporization, as LN_2 is stored near its boiling point. Consequently, the temperature stability was roughly maintained by providing the maximum flow rate the dewars used would allow. This translated to a $\sim$ 1K increase in detector temperature over a 100 minute period. As the dewar emptied, the flow rates dropped, and temperatures rose.

The helium cooled system provided much finer control over system temperatures, and surpassed the Nab cooling stability specification comfortably. A stability of $\pm$ 0.1K was demonstrated for typical run lengths (4.5 to 5.5 hours): see Fig. 3.10. The temperature stability goal for Nab is $\pm$ 0.5K. Consequently for the 2017 ^{45}Ca running, this helium cooled system was implemented.

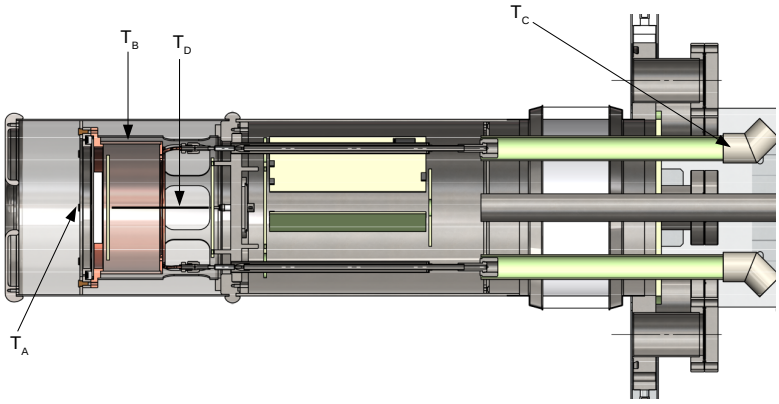

Figure 3.9: The temperature sensor at T_A measured the temperature on the face of a silicon detector. T_B monitored the temperature of the copper can which acted as a coldfinger for the detector. T_C was the temperature at the cooling inlet to the detector mount, and T_A corresponded to a temperature sensor mounted to a FET.

3.2.3 Nab Improvements

The design of the Nab cooling system was updated and improved upon with each prototype. As such, the Nab design reflects important aspects discovered while testing. As previously noted, the 2017 ^{45}Ca detector system was cooled by helium liquefier exhaust. Because only a single liquefier was operating, the helium line was split to cool each detector. This split occurred downstream of the flow controller. A separate PID loop was implemented for each line in an attempt to independently stabilize detector temperatures. The cooling procedure was as follows. The system was allowed to naturally cool to equilibrium over the course of about two hours. Upon reaching equilibrium, the temperature setpoint of each PID loop was set one or two degrees C higher than the equilibrium temperature. However, these relatively small changes to the helium temperature resulted in large temperature oscillations between the two lines. When a heater was powered in one line (say the East line), the effective flow impedance for that path increased, which caused a decrease in mass flow along the East line. The increased impedance caused the excess helium to travel along West line, which created a higher power demand on the West cartridge heater maintaining the West line's temperature. Then as the impedence along the West line

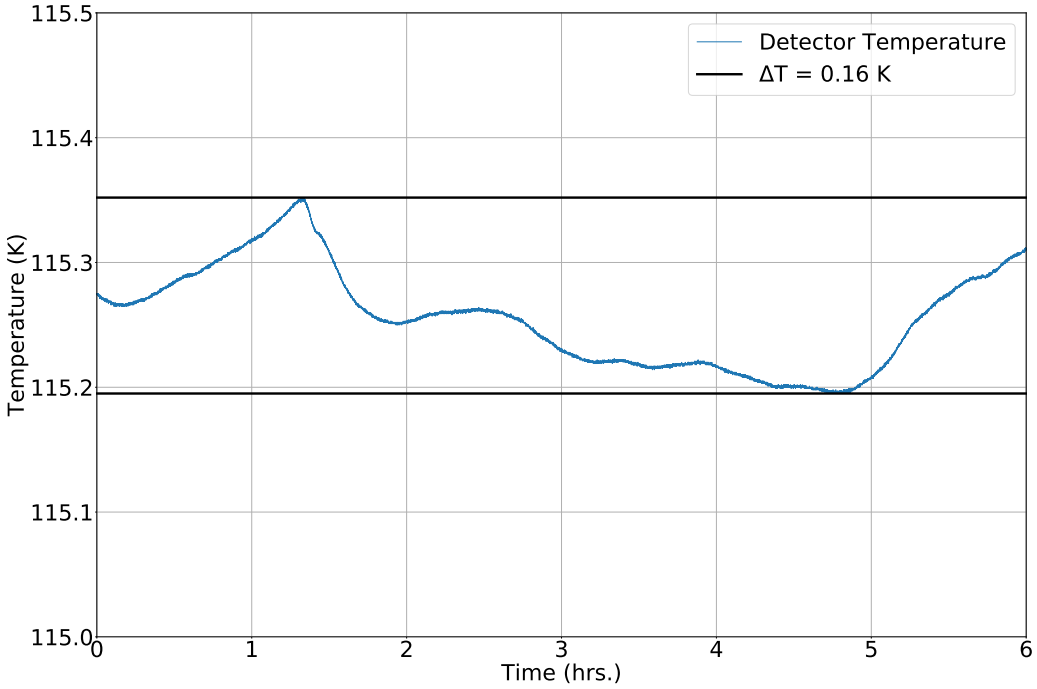

Figure 3.10: The goal for the Nab detector temperature stability is $\Delta T \sim 0.5K$ over the length of a run. Above demonstrates a $\Delta T < 0.16K$ over a 6 hour (rougly 12 run) period.

increased, more flow was directed along the East line. Despite several PID parameter changes, the resulting large, correlated temperature oscillations between the two lines could not be damped. This problem has been eliminated from Nab by the use of two separate helium lines.

Microphonic noise due to cooling also has also been significantly reduced. The switch to helium from LN_2 eliminated a coolant phase change, which resulted in a significant reduction in oscillation amplitude. The coolant switch did not completely remove the oscillations present in waveform data. By comparing the amplitude of the oscillations observed in the East detector system to that of the West, it has been deduced that the cooling line size is partially responsible. The major mechanical difference between the East and the West detector mount is the size of the cooling lines within the mount. The West mount has a neckdown from a 1/4" line to an 1/8" line. The East detector mount was designed with a 1/4" cooling line throughout, and the data collected from the East detector did not suffer from as large of baseline oscillations as that of the West detector. The Nab detector mounts have both been designed with 1/4" inner diameter (ID) lines.

In addition to noise reduction and an elimination of "cross-talk" between cooling lines, the thermal loads within the mount and spectrometer have also been reduced. The Nab spectrometer is a cold bore magnet ($\sim$ 70K), as opposed to the warm bore of the SCS. Thus the bore of the Nab magnet results in radiative cooling of the detectors. Another gain in cooling power comes from the update to the inlets of the detector mounts. As can be seen in Fig. 3.7, the inlet and outlet both are composed of uninsulated G10 (green). A significant portion of the cooling power for the ^{45}Ca experiment was lost here regardless of the cooling method. This G10 (and accompanying ceramic break of the mount) provided electrical insulation between the high voltage (30 kV) and grounded components of the UCNB and ^{45}Ca setups. For Nab, the entire mount floats at 30 kV and the break occurs between the inner and outer HV cage. G10 is still used to transport the coolant from a grounded line to a 30 kV line, however these feedthroughs are vacuum jacketed (see above Fig. 3.3).

Although there exists some heat leak at the bayonet connections ($\sim$ 7W per bayonet connection [63]) the rest of the line is vacuum jacketed. Therefore heat loads due to coupling to the room temperature are significantly reduced.

3.3 ORNL Benchmarking

3.3.1 High Voltage Feedthrough Testing

The first custom components produced for the Nab cooling system were the high voltage feedthroughs seen in Fig. 3.3. The technical drawings for these feedthroughs along with a few notes of interest may be found in Appendix B. As noted above, the lines are used to transport the helium coolant into the high voltage cage, while standing off the 30 kV potential between the inner and outer cage. The lines were constructed by using cryogenic epoxy to glue the inner and outer G-10 tubes to 3" linde-style bayonets manufactured by Cryofab. The fully assembled high voltage feedthroughs were then checked for leaks with a standard helium leak detector. Three of the four feedthroughs maintained a leak rate of $< 10^{-8}$ mbar $\cdot$ L/s. To determine a the lowest attainable pressure of the isolating volume between the inner and outer G-10 lines, the three leak tight feedthroughs were individually pumped on over the course of a few days. With a HiCube Eco 80 pumping station, a base pressure of a few 10^{-4} Torr was achieved for the three assemblies. While the next round of testing for the three lines was ongoing, the leak of the fourth feedthrough was eventually identified and repaired.

The three lines were subjected to thermal cycling to verify their structural integrity at low temperatures. The cycling was designed to test the feedthroughs in much harsher conditions than that of their designed usage. The vacuum jacketing of each line was actively pumped and, its pressure monitored. See Fig. 3.11 for a diagram of the setup. The feedthroughs were connected to a LN_2 dewar, and once the pressure reached the $10^{-3} - 10^{-4}$ Torr level, LN_2 was passed through the feedthrough. The

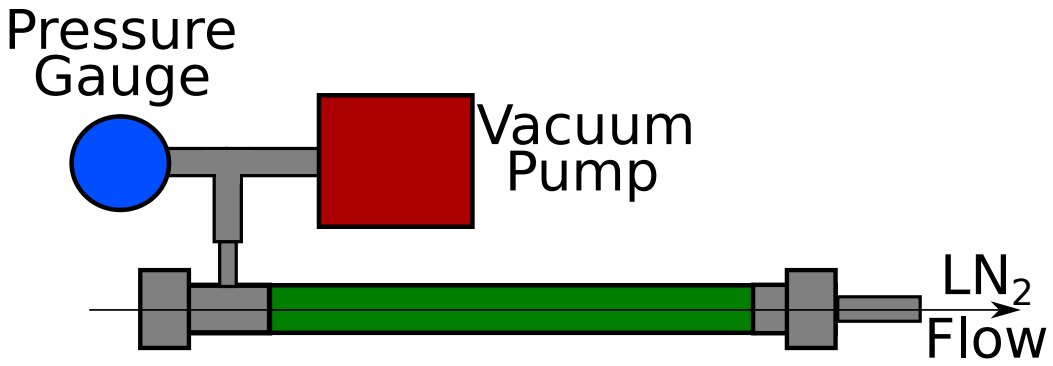

Figure 3.11: The pump out port of the high voltage feedthrough lines were connected to a vacuum pump in parallel with a pressure gauge. Once a pressure on the order of mid-10^{-4} Torr was reached, LN_2 was passed through the feedthrough at the maximum rate provided by the dewar.

maximum flow rate was used to test the HV feedthroughs at extreme conditions, with very large thermal gradients across the feedthrough. LN_2 cooling of the HV feedthrough for roughly continued for roughly 5 minutes, until LN_2 was observed exiting the feedthrough. This was repeated on a daily basis approximately ten times for all available feedthroughs.

The results of the cycling were mixed. All feedthroughs survived four rounds of cycling without any indication of structural failure. One feedthrough failed during the fifth round. While cooling, a metallic pop was heard and the pressure immediately jumped from the 10^{-6} Torr range to the 10^{-1} Torr level. The test was abandoned, and the feedthrough was allowed to warm back to room temperature naturally over the course of 24 hours. Upon inspection with the helium leak detector, a leak was discovered in the inner line of the feedthrough. The cause of the leak was attributed to the thermal contraction of the inner G-10 line. Because of the insulation provided by the vacuum between the inner line and the outer jacketing, the outer G10 remains at room temperature and does not exhibit significant thermal contraction. However, the temperature of the inner line decreases by 200K, which creates internal stresses longitudinally along the inner line. Although the outer vacuum jacketing was never removed and the exact location of the leak identified, it is highly likely the leak occurred at the glue joint between the G-10 and the stainless steel bayonet. The

tensile strength of the epoxy (3500 PSI) is an order of magnitude smaller than the rating of the G-10. As the inner line cooled, the internal stresses built and eventually overcame the ultimate tensile strength of the joint. The remaining two high voltage feedthroughs were subjected to five more rounds of cycling for a total of ten cycles without failure.

Subsequently, a modification was made to the feedthrough design. A small bellows was included in the inner line, which allows the inner line to have some flexibility. See Appendix B for more detail.

3.3.2 Heat Exchager Testing

It was apparent from the results of the first set of cooling studies conducted at LANSCE (see Sec. 3.2.2) that a heat exchanger somewhat more sophisticated than cold coiled copper tube was required. As previously discussed in Sec. 3.1.1, the heat exchanger designed for Nab consisted of cold copper disks through which the gas travels. The design creates more turbulence and increases the efficacy of the heat exchanger. The heat exchangers, being custom components, therefore also required some benchmarking. The technical drawings for these may be found in Appendix F.

Base Temperatures

The first study aimed to measure the lowest temperature achievable for the two heat exchangers. See Fig. 3.12 for a model of the setup. The heat exchangers were bolted to the cold head via the cold head mount plate. This mount plate was machined from OFHC copper and bolted to the cold head. Because of the purity of the copper and the area over which contact is made (the full cross section of the cold head), the temperature of the mount plate is tightly coupled to and, for all of the following, will be regarded as having the same temperature as the cold head itself. Temperature sensors were mounted to the cold head mount plate (CH) and the disk furthest from the cold head (i.e. warmest) in each heat exchanger (HE). The cold head was powered

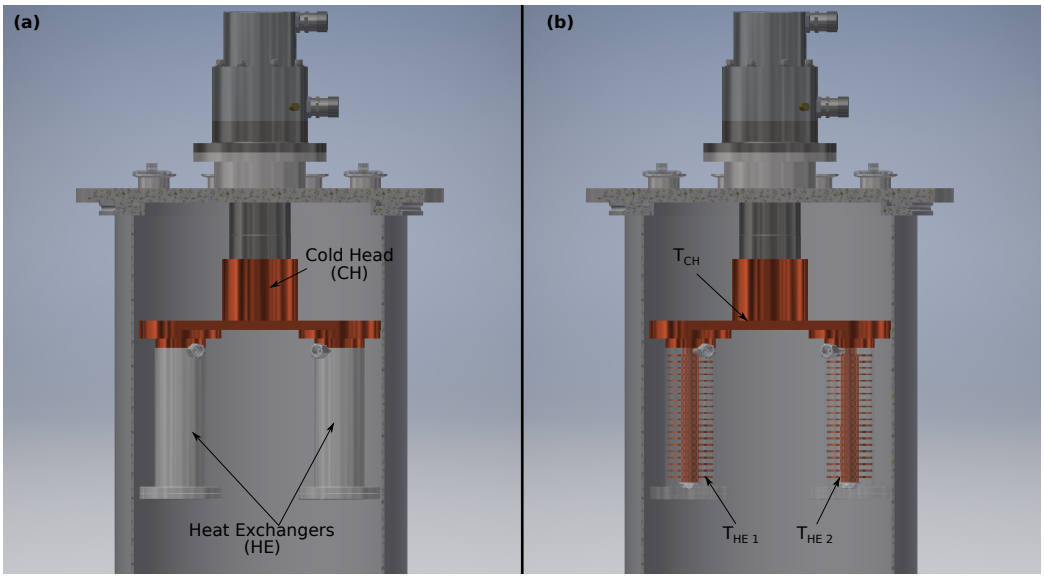

Figure 3.12: As shown above, heat exchangers were mounted to the cold head. A temperature sensor was fixed to the cold head mount plate (T_{CH}), as well as to the warmest copper disks of the two heat exchangers (T_{HE_1} and T_{HE_2}).

and the temperatures were monitored until they began to approach equilibrium, at which point the cold head was shut off. See fig 3.13 for a plot of the observed temperatures as a function of time.

Note that the cold head temperature ($\mathrm{T_{CH}}$) and second heat exchanger temperature ($\mathrm{T_{HE_2}}$) were measured via platinum resistance temperature detectors (RTDs). The lower limits of the platinum RTDs are on the order of 20K. Upon reaching this limit, the reading falls to 0K and should be disregarded. The goal of the test was to verify that the cooling power provided by the cold head could dissipate the radiative heat loads and keep the temperatures of the heat exhangers well below 60K, the design temperature of the helium coolant. As shown in Fig. 3.13, both heat exchanger temperatures did indeed fall to temperatures less than 35K.

Heat Exchanger Coupling

The cooling system studied at LANSCE which utilized the exhaust of a helium liquefier (see Sec. 3.2.2) showed that coupling between the two cooling lines

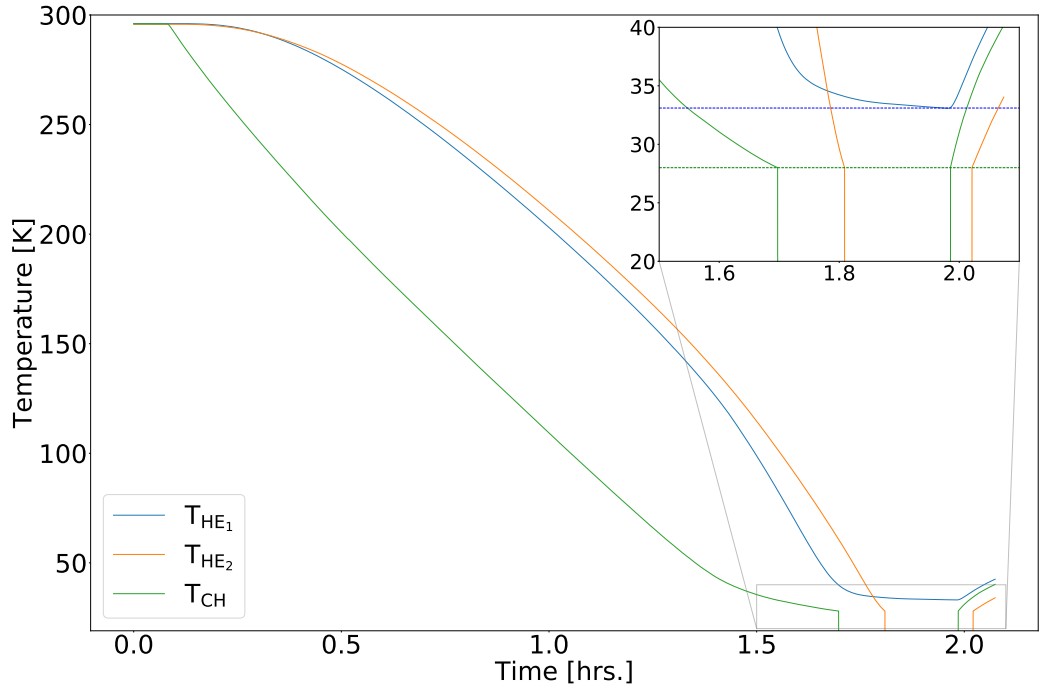

Figure 3.13: Shown above are the temperature profiles observed during the cooldown of the cold head and attached heat exchangers.

complicated temperature control and stability. For the Nab system, the helium lines themselves are separated, and the only coupling that can occur is thermal coupling through the heat exchangers and cold head. A second study was attempted following the above cool down with the intent to begin to quantify the degree to which the two cold head temperatures were coupled.

After conducting the base temperature measurement of the heat exchangers, the cold head was powered down and the system allowed to warm. Temperature recording was initiated during the warming process, and some time later the cold head was re-energized. See Fig. 3.14 for the temperature profiles recorded. For this study, the quantity of merit is the amount of time Δt required for a change in the cold head temperature to be reflected at the warmest part of the heat exchanger, i.e. the amount of time required for a temperature change in the cold head to fully propagate through the heat exchanger. This time Δt was estimated by comparing the time at which the maximum temperature was reached by the heat exchangers and the corresponding

time for the cold head. As indicated in Fig. 3.14, a $\Delta t \sim 65$s was measured. In comparison, the amount of time for a change in one line to be reflected in the other cooling line was on the order of a few seconds while testing at LANSCE. Hence, it was concluded that the coupling between the heat exchangers was much weaker than that of the coupling between the two lines used at LANSCE.

3.3.3 Conclusion

The preliminary design of the cooling system for the Nab detectors and accompanying electronics featured LN_2 as the coolant. This system was tested and benchmarked via the UCNB experiment. There were many logistical problems which arose from such a system design. Additionally, a strong presence of noise due to the physical shaking of the cooling lines was observed in the UCNB data. This shaking has been attributed to the phase change which inevitably occurs with a coolant stored at its boiling point. To mitigate these complications, the cooling system was redesigned. The updated design features a recirculating helium gas coolant. Early prototypes of this system implemented at LANSCE showed promising results. The major components have been assembled and tested at the FnPB. The Nab detector mounts should arrive at ORNL in spring of 2020, at which point the cooling system will be fully commissioned. Technical design drawings created by this author may be found in the appendix (Ap. B-G).

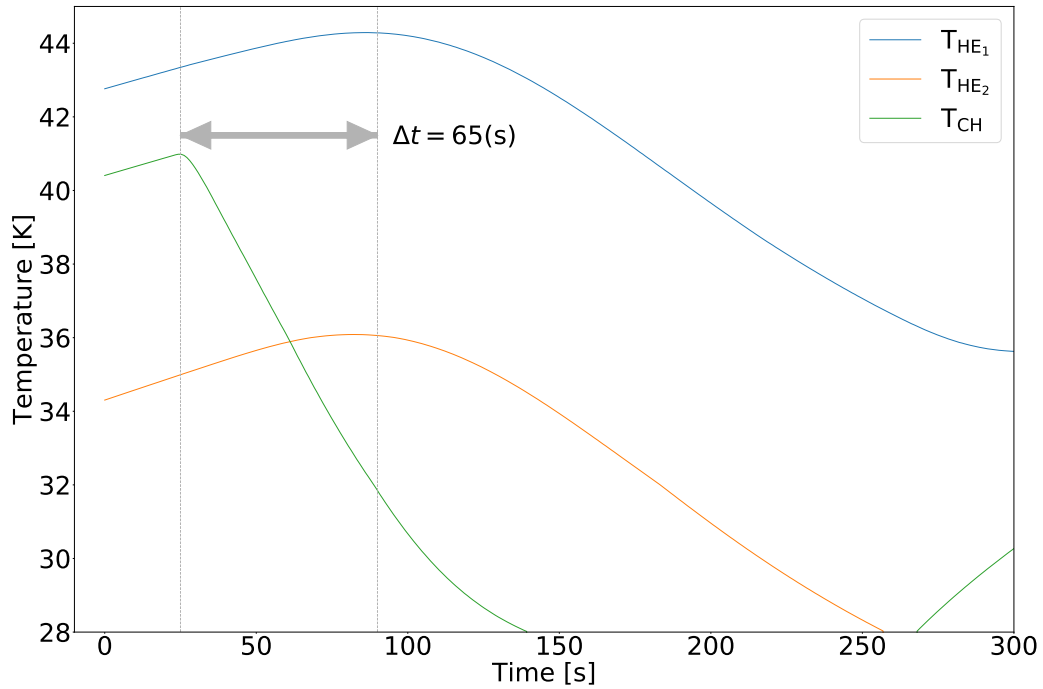

Figure 3.14: The temperatures recorded for the second set of testing conducted on the heat exchangers is shown above. The strength of the coupling between the two heat exchangers was inferred from the amount of time elapsed Δt between the location of the cold head maximum temperature and the heat exchanger maximum temperature. In comparison to the amount of time for changes in cooling lines at LANSCE to be reflected in one another (on the order of seconds) this change is relatively long, and therefore the coupling is weak in comparison.

Chapter 4

^{45}Ca Beta Spectrum Measurement at LANL

4.1 Motivation & Theory

As has been discussed in Ch. 1, the Fierz interference term 'b' is a beta decay correlation coefficient that provides an avenue to probe BSM physics. The advantage to a measurement of 'b' is that it is linear in scalar and tensor currents, whereas other BSM sensitive coefficients are typically quadratic in these small couplings [9]. From Ref. [14], the linearized form of 'b' is:

$$b \approx \pm 2\gamma \frac{1}{1+|\tilde{\rho}^2|} \mathrm{Re}\left(\frac{C_S + C'_S}{C_V + C'_V} + \left|\tilde{\rho}^2\right| \frac{C_T + C'_T}{C_A + C'_A}\right) \tag{4.1}$$

where $\tilde{\rho} \equiv \frac{C_A + C'_A}{C_V + C'_V} \frac{M_{GT}}{M_F}$, $\gamma \equiv \sqrt{1-\alpha^2 Z^2}$, and the leading sign corresponds to the decay type :+ for beta minus and − for beta plus decay. For a pure Fermi beta minus transition, $M_{GT} = 0$, and thus 'b' reduces to:

$$b_F \approx -2\gamma \mathrm{Re}\left(\frac{C_S + C'_S}{C_V + C'_V}\right) \tag{4.2}$$

Similarly for a pure Gamow-Teller beta minus transition, $M_F = 0$ and 'b' is given as:

$$b_{GT} \approx -2\gamma \mathrm{Re}\left(\frac{C_T + C'_T}{C_A + C'_A}\right) \tag{4.3}$$

Recall from Eq. 1.10 that for an unpolarized nucleus, the beta decay distribution is given as:

$$\begin{aligned} w(E_e\Omega_e\Omega_\nu)dE_e d\Omega_e d\Omega_\nu =& \frac{F(\pm Z, E_e)}{(2\pi)^5} p_e E_e (E_0 - E_e)^2 dE_e d\Omega_e d\Omega_\nu \times \\ & \xi\left(1 + a\frac{\boldsymbol{p_e}\cdot\boldsymbol{p_\nu}}{E_e E_\nu} + b\frac{m_e}{E_e}\right) \end{aligned} \tag{4.4}$$

Hence a measurement of 'b' can be accomplished by looking for deviations in the beta decay energy spectrum from that of SM predicted spectra. It is worth noting, however, that as new techniques and technologies push the bounds of experimental precision, BSM searches are forced to include corrections (arising from SM physics) that had previously been neglected. The weak magnetism form factor b_{WM}, which arises from the confined nature of quarks, is of particular importance to Fierz searches via beta decay energy spectrum distortions.

To accurately describe the Fierz term at the $\Delta b \sim 10^{-3}$ level, the weak magnetism form factor must be included when considering any pure or mixture of Gamow-Teller transitions [64, 65]. For a pure Gamow-Teller transition, the differential decay rate gains a term proportional to the energy of the outgoing electron (positron) scaled by the average of the mass of the parent and daughter nucleus M. Eq. 4.4 becomes [64, 66–68]

$$\begin{aligned} w(E_e\Omega_e\Omega_\nu)dE_e d\Omega_e d\Omega_\nu =& \frac{F(\pm Z, E_e)}{(2\pi)^5} p_e E_e (E_0 - E_e)^2 dE_e d\Omega_e d\Omega_\nu \times \\ & \xi\left(1 + a\frac{\boldsymbol{p_e}\cdot\boldsymbol{p_\nu}}{E_e E_\nu} + b\frac{m_e}{E_e} + b_{\mathrm{WM}}\frac{E_e}{M}\right) \end{aligned} \tag{4.5}$$

Note that the Fierz term is proportional to $1/E_e$ and the weak magnetism term is proportional to E_e. Therefore a nucleus with a low endpoint energy is best suited for Fierz searches, as the beta spectrum shape suffers from smaller weak magnetism interference. The decay of ^{45}Ca is a $7/2^- \rightarrow 7/2^-$ transition with a branching ratio of 99.9981(11)%. With an endpoint energy of $\sim$ 256 keV [69], ^{45}Ca is a particularly well suited nucleus for a Fierz measurement. In Fig. 4.1, the effect of the Fierz interference term on the ^{45}Ca beta spectrum can be seen for various values of 'b'.

4.2 Experimental Setup

Radioactive Sources

The ^{45}Ca source used was prepared at the Institute for Nuclear and Radiation Physics (IKS) of The Catholic University of Leuven (KU Leuven). A 60 μL water-based solution of ^{45}Ca with an activity of approximately 1.2 kBq was deposited on a 100nm thick 6F-6F polymer film. The source was dried under an infrared lamp and mounted in an aluminum frame. See Fig. 4.2 for a picture of the source in its holder. For the remainder of the discussion, the ^{45}Ca source and the aluminum frame in which it was mounted will simply be referred to as the ^{45}Ca source. Additional radioactive sources of ^{113}Sn, ^{207}Bi, and ^{139}Ce were used for energy calibration and gain monitoring sources throughout production data taking. These sources are Isotrak calibration sources commercially produced by the Eckert and Ziegler Group [70].

The Superconducting Solenoidal Magnet

To measure the beta energy spectrum, the aforementioned sources were placed the Super Conducting Spectrometer (SCS) in Area B of LANSCEf. See Fig. 4.3 for a layout of the area. The SCS consisted of a 1 T superconducting solenoidal magnet and two detector systems at each end. The superconducting solenoidal magnet is a custom warm bore magnet manufactured by American Magnetics Inc. Further information

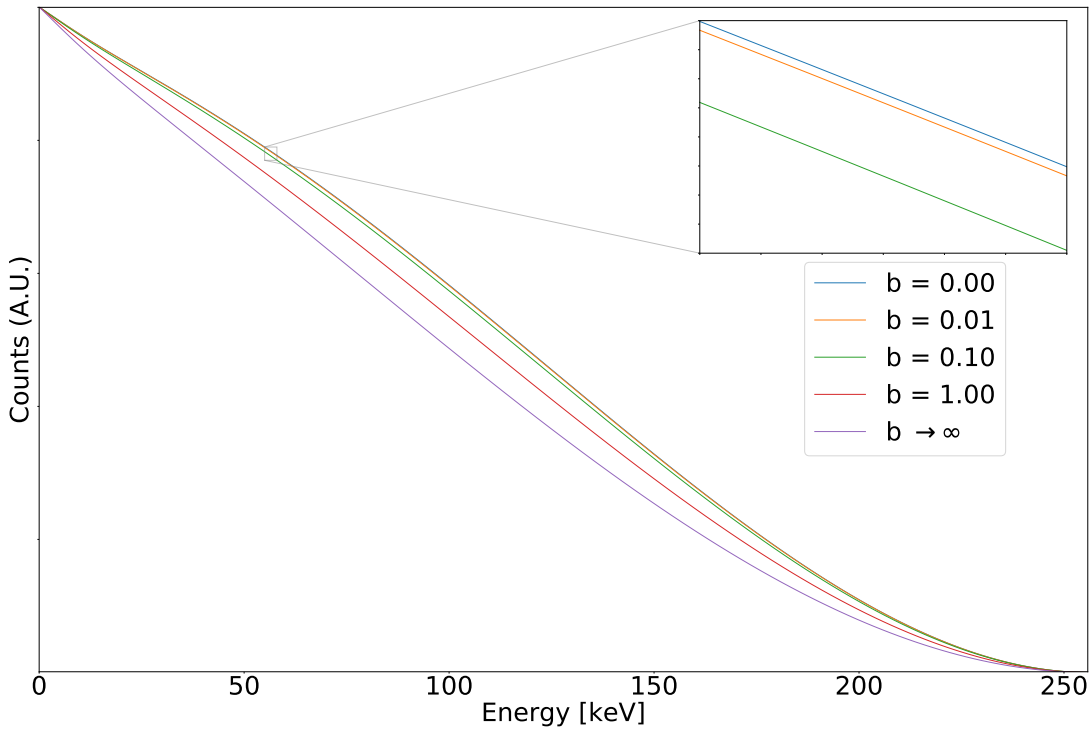

Figure 4.1: Above is a plot of the simulated beta decay energy spectrum for ^{45}Ca, including the effect of the Fierz interference term at various values. In comparison to the Fierz distortions of the neutron spectrum of Fig. 2.2, the ^{45}Ca beta spectrum is much more sensitive to a nonzero value of 'b'.

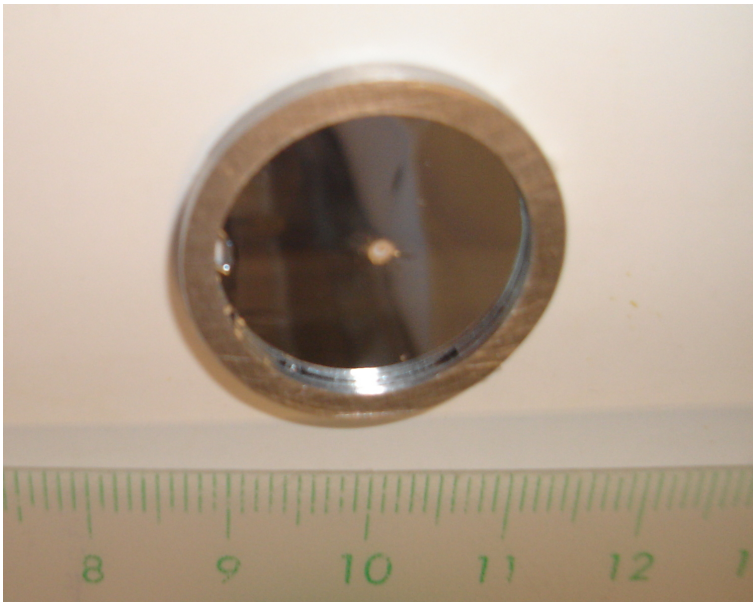

Figure 4.2: The ^{45}Ca source was deposited in solution on a 100 nm 6F-6F foil. The solution was dried and mounted in an aluminum frame on a 10 nm aluminum substrate.

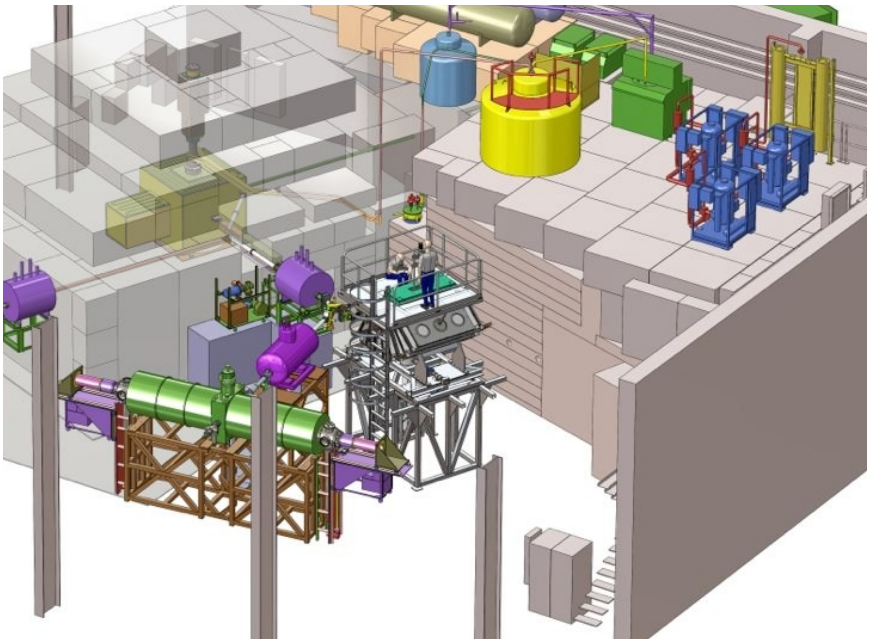

Figure 4.3: The ^{45}Ca source was placed in the SCS (green cylinder). The detector cooling was supplied via the exhaust of the helium liquefier in the area (green rectangular prism upper right corner).

regarding the design of the SCS can be found in ref. [71]. The ^{45}Ca source was set in a polyethylene carriage and placed near the center of the SCS in the 1T magnetic field region. The decay electrons were guided by the magnetic field to silicon detectors at either side of the SCS. The detectors themselves resided in the 0.6T field expansion region (see Fig. 4.4). To insert the calibration sources *in situ*, the load-lock on the SCS was utilized to intermittently insert the ^{113}Sn, ^{139}Ce, or ^{207}Bi sources.

The detectors were cooled with cold ($\sim$ 40K) helium gas (see Sec. 3.2.2), and the detectors were biased to 250-300 V, The signals generated were amplified and shaped by front end electronics. The main components of the electronics chain consisted of a FET, pre and post-amplifier [61, 62]. The output of this electronics chain was fed to a National Instruments (NI) data acquisition (DAQ) system. The signal was digitized and then processed by on board field programmable gate arrays (FPGAs). The amplitude of the digitized signal was given in terms of analog to-digital-converter bins (ADC) Should an event satisfy a trigger condition as determined by the FPGA,

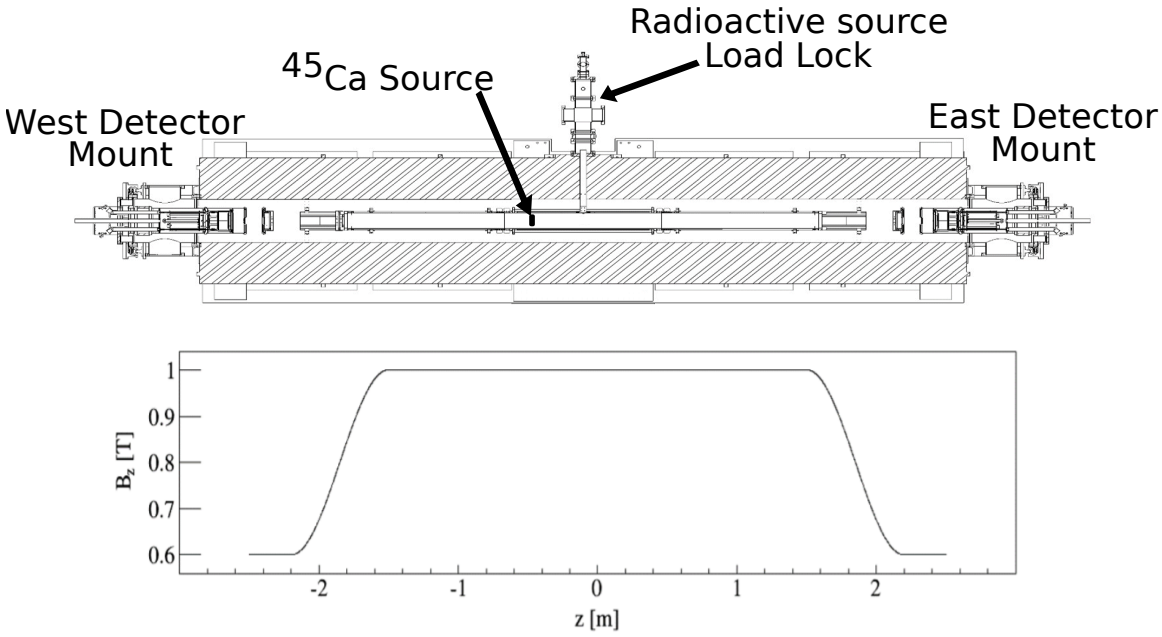

Figure 4.4: Decay electrons were guided by the 1T magnetic field to the silicon detectors mounted at each end of the SCS.

the event was written to file. The triggering scheme and is discussed in more detail in Sec. 4.3.2.

4.3 The Detector System

4.3.1 Silicon Detectors

The detectors used for the ^{45}Ca experiment were single-crystal silicon diode detectors. Single crystal silicon is a useful medium for radiation detection because it is much more dense and therefore much smaller than its gas-filled, ionization chamber counterparts. In addition, the electronic energy level structure inherent to semiconductors provides excellent energy resolution. For crystalline semiconductors, outer shell electron energies fall within one of two energy bands: the valence or conduction band. Any electron within the valence band is energetically confined to a specific lattice site. Electrons within the conduction band have higher energy and can

freely propagate through the lattice. The valence and conduction bands are separated by a band gap of energy E_{g}. Intrinsic, un-doped, crystallized silicon has a band gap of $E_{\mathrm{g}} \approx 1.63$ eV at 110 K [72]. For a zero temperature crystalline lattice, the valence band would be completely occupied, and the conduction band would be left empty. At finite temperatures, the probability of thermal excitation of a valence band electron to a conduction band is given by: $p(T) = CT^{3/2}e^{\left(-\frac{E_{\mathrm{g}}}{2kT}\right)}$, where k denotes the Boltzmann constant and T the temperature of the lattice (K) [57].Thus with a low, well controlled detector temperature, the number of charge carriers liberated by incident radiation is proportional to the energy of the incident particle.

Pure semiconductors are referred to as intrinsic semiconductors. The aforementioned property whereby the energy of charged particle stopped by a semiconductor can be determined by the number of charge carriers liberated is very desirable for radiation detection. The downside is that the charge carriers liberated by the incident particle are difficult to collect from an intrinsic semiconductor, as diffusion of charge depends linearly on temperature. Thus the low temperature used to reduce the thermal noise also lowers charge mobility. As such, fully intrinsic semiconductors are rarely used as radiation detectors. Instead, the intrinsic semiconductor is typically doped with impurities that readily accept or donate charge carriers within the crystalline lattice.

The type of doping is referred to by the type of charge the dopant introduces or facilitates. An n-type (negative) dopant is an element which donates an electron to the conduction band of the crystal. Electrons bound to the n-type dopant only require a small amount of energy to be promoted to the conduction band, and the overall effect of the n-type dopant is a contribution of negative charge (the elctron) to the conduction band of the intrinsic semiconductor. A p-type (positive) dopant is generally an element which has an unoccupied electron state which is energetically very close to the valence band of the crystalline lattice. Very little energy is required for an electron within the valence band of the crystal to move to a bound state of the p-type "acceptor". The movement of a valence band electron to an acceptor

site leaves behind a hole, or a low-lying unoccupied state, in the silicon atom from which it came. Neighboring valence band electrons fill this hole, and the hole diffuses through the lattice. While in actuality, the only particles involved are electrons, this hole can be treated as an electron with a $+e$ charge. Hence, the net effect of the p-type impurity is to accept valence electrons, which creates a positive current. These impurities are introduced to the semiconductor crystal typically either through diffusion or ion implantation.

At the boundary between a p-type and an n-type region, there exists a discontinuity in conduction electron (and valence hole) density. Therefore a net diffusion takes place, where conduction electrons migrate from the n-type material to the acceptor sites of the p-type. Just as the conduction electron density discontinuity causes the migration of electrons to acceptor sites, the hole density discontinuity as seen from the p-type side causes a net diffusion of holes across the boundary as well [57]. The effect of these two processes creates a negative charge accumulation into the p-type material and a positive charge accumulation into the n-type material. This establishes an electric field that suppresses charge migration across the boundary away from its respective carrier material (see Fig. 4.5). The field established repels electrons from the p-type side, towards the n-type material. The accumulation of negative space charge near the boundary within the p-type region repels the electrons back into the n-type region. Similarly, the positive charge within the n-type material near the junction sweeps holes back to the p-type side. The region over which this electric field extends is the depletion region. This region may be extended through the width of the entire detector by *reverse biasing* the detector. By applying a negative potential to the p-type side with respect to the n-type, the electric field established near the boundary is extended. The potential causes further conduction electron migration across the boundary and further into the p-type bulk. The overall effect is to increase the magnitude of the electric field and extend the region over which the depletion region exists. With a sufficiently large bias, this depletion region will extend through

the entire detector. As a result, very little current naturally fluctuates through the detector, which significantly reduces detector noise.

When a charged particle is stopped in a crystalline semiconductor, most of the deposited energy results in electron-hole pair creation. If an energy of E is deposited, then roughly $N = E/E_{\text{p-h}}$ particle hole pairs are created. For silicon, $E_{\text{p-h}} \sim 3.6$ eV [57]. For ^{45}Ca, Q $\sim$ 256 keV. Then for an electron at the endpoint energy, there are roughly 85,000 electron-hole pairs created. With a sufficiently large bias (i.e. a sufficiently depleted detector) the majority of these charges do not recombine and are collected. The silicon detectors implemented also have a small layer of silicon dioxide which surrounds the bulk crystal. Even with a fully depleted detector, charge liberated within the dead layer cannot fully be collected. Silicon detector manufacturers go to great lengths to minimize the thickness of this dead layer and thereby increase detector energy resolution. The ^{45}Ca detectors are reported to have a very thin dead layer of roughly 100 nm.

The silicon detectors used for the ^{45}Ca and Nab experiments are single-crystal silicon and were developed by Micron Semiconductor, Ltd [73]. A diagram can be seen in Fig. 4.6. The bulk of the ^{45}Ca and Nab detectors was slightly n-type due to residual donor impurities. The junction side (top in Fig. 4.6) was heavily doped with boron, creating a p^+ region. The ohmic side (bottom in Fig. 4.6) was a phosphorous-implanted n-type region. The junction side was metallized with a $\sim$ 300 nm thick, square aluminum wire grid covering 0.04% of the active area. The active area itself covered roughly 90 cm^2, with an 11.7 cm diameter. Charge collection took place through the hexagonal pads in contact with the ohmic side of the detector. These pads were separated by about 100 μm. The pad-detector combination is referred to as a detector pixel.

There were 127 pixels total on each detector, however for the ^{45}Ca experiment, only 19 were instrumented, and the others were grounded (see Fig. 4.7 for a pixel map). Relative pixel locations between the two detectors were determined via calibration sources (this work was carried out by the author of Ref. [74]). The sources in the

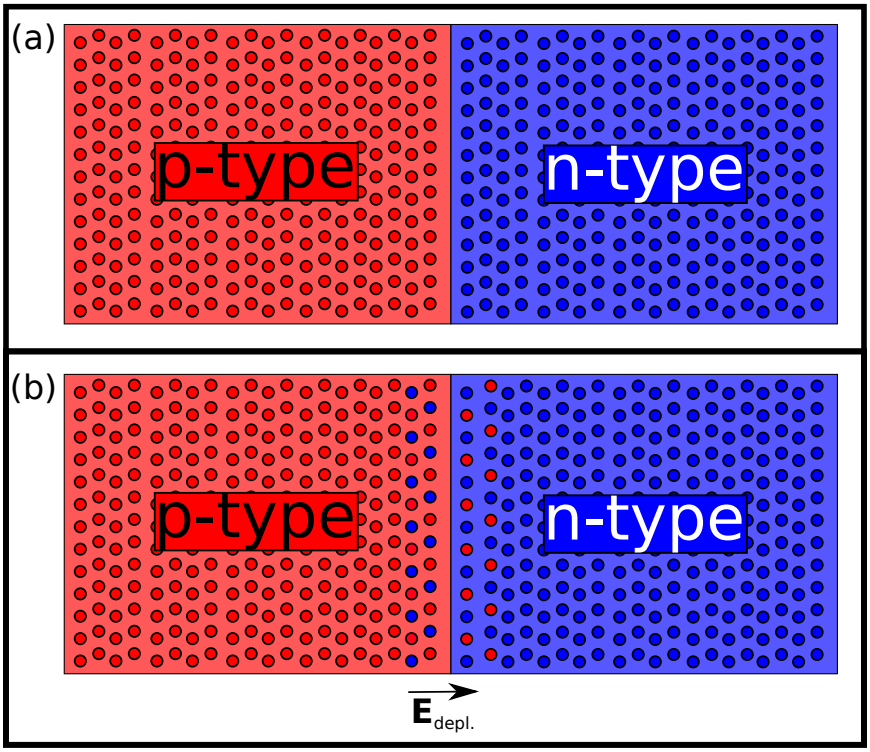

Figure 4.5: (a) A p-type and n-type material are brought together to form a p-n junction. **(b)** The proximity of acceptor sites to donor sites at the boundary causes electrons and holes diffuse across the boundary [57]. It is important to note that the p-n junction is neutral overall. This charge migration only results in local nonzero charge densities. The region overwhich these densities exist is the depletion region. The electric field which exists throughout the depletion region suppresses further charge migration.

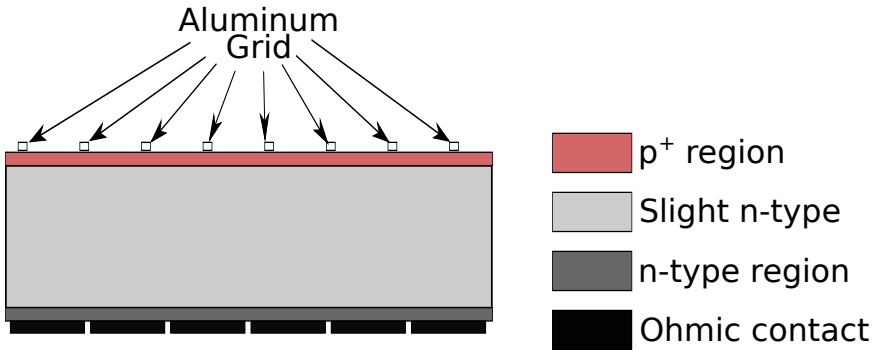

Figure 4.6: Detector Diagram: The bulk of the silicon is slightly (near intrinsic) n-type. The Junction side (red) is p^+ (heavily doped with Boron) with an aluminum grid to improve conductivity. The ohmic region is an n-type phosphorous doped region. Contact with the detector is achieved via the 127 ohmic contacts (black), which create a pixelation of the silicon bulk [61, 62].

load-lock of the SCS were repositioned on a run-by-run basis. The changes in relative count rates between pixels from run to run were then used to determine approximate relative pixel locations. If one considers the centroid of a pixel on a given detector, its *mirror pixel* is the pixel on the opposite detector whose centroid is closest to that of the original pixel. The mirror pixel to 64E is 64W, for example. The locations were utilized in the trigger scheme discussed below (see Sec. 4.4).

4.3.2 Front End Electronics & Data Acquisition System

The detector signal was amplified and shaped by front end electronics which consisted of a cooled ($\sim$ 200K) BF682 field effect transistor (FET) and a room temperature AD8011 preamplifier. For a more detailed description, see Ref. [62]. The amplified and shaped signal was then passed to an NI PXIe-5171R ADC Module, where the signal was digitized and processed by an onboard field programmable gate array (FPGA). To determine whether to write a given trace to file, a double trapezoid filter was implemented. Further details about the DAQ firmware developed and implemented for the experiment can be found in Ref. [75].

A single trapezoidal filter and its implementation is outlined in Ref. [76] and its interpretation is described in Ch. 5. The double trapezoidal filter is produced by first

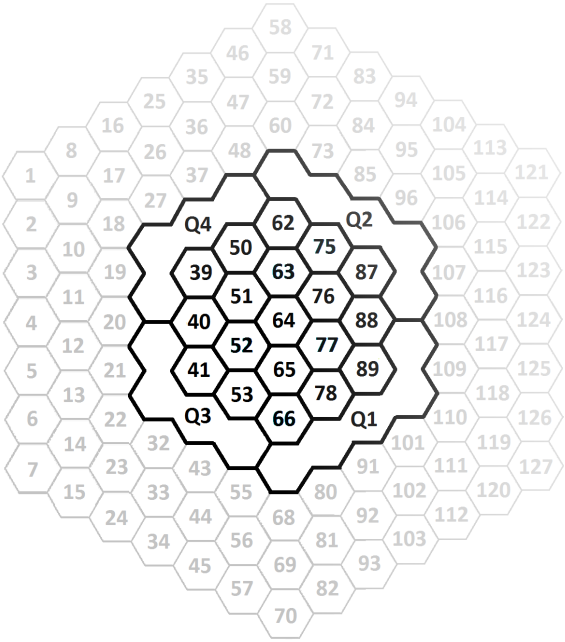

Figure 4.7: For the ^{45}Ca experiment, only the central 19 pixels of the 127 were active pixels; all others were grounded. The pixel designated Q1, Q2, Q3, and Q4 were banks of 5 pixels tied together and read out by a single preamp channel. Capacitve mismatch between the preamp and the ganged pixels however caused the preamplifier to be highly unstable and highly susceptible to large oscillations. Ultimately these too were grounded.

constructing a negative single trapezoidal filter impulse response and concatenating it with the negative of itself. The FPGA recursively generated the double trapezoidal filter output in real time. If the ouput exhibited a rising edge through some threshold, the trigger was armed. If the output then rose above zero, the trigger condition was met, and the 14 μs trace was written to file. See Fig. 4.8 for a demonstration.

4.4 Run Configurations and Setup

The data taking run modes for the ^{45}Ca beta spectrum measurement fall into one of two types of running. In *pre-production* run modes aspects of the detector or the amplifying electronics chain were studied. No ^{45}Ca data was taken during these runs. During *production* data taking, either ^{45}Ca or calibration source data were taken.

4.4.1 Pre-production data

To determine the appropriate bias voltage and monitor any gain drift of the electronics chain, a Precision BNL PP5 was capacitively coupled to the bias line of each detector through a 1 nF capacitor (see Fig. 4.9). The voltage was set such that the charge injected into the detectors corresponded to a roughly 530 keV signal. For production data taking, the rate was set to 2 Hz, which corresponds to about 1000 counts in the pulser peak per pixel per run. Thus any statistically significant change in the pulser peak mean location would be indicative of amplifier gain shift.

The bias voltage for each detector was determined by measuring the pulser peak width as a function of bias voltage. It should be noted that the voltage measured across the detector junction and the ground was negative, however only the magnitude of the voltages will be referenced. A set of data runs were taken at various bias voltages from 0 V to 100 V in 10 V increments and then from 100 V to 500 V in 50 V increments. For this set of runs, the pulser output was split, with one line fed directly to the DAQ. The DAQ trigger was set such that all pixel waveforms were written to

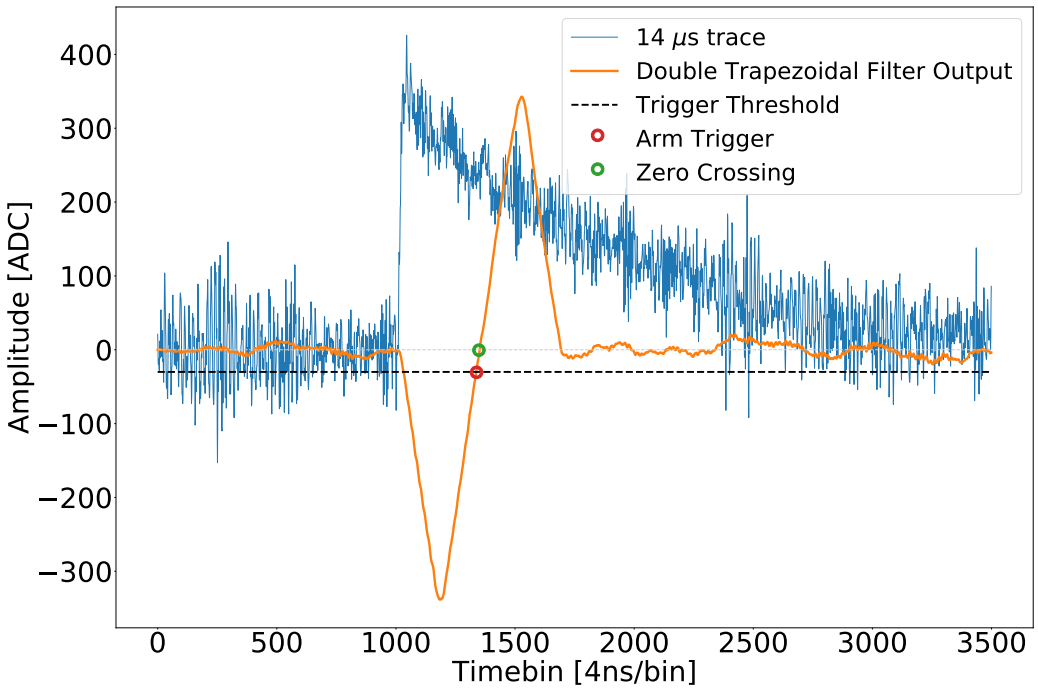

Figure 4.8: The output of the preamp was digitized and processed by the FPGA. The FPGA applied a double trapezoidal filter to the data and monitored the output for a trigger condition. Should the signal have a rising edge through some threshold (black), the trigger was armed (red circle). If this is followed by a zero crossing (green circle), the 14 μs trace was written to disk.

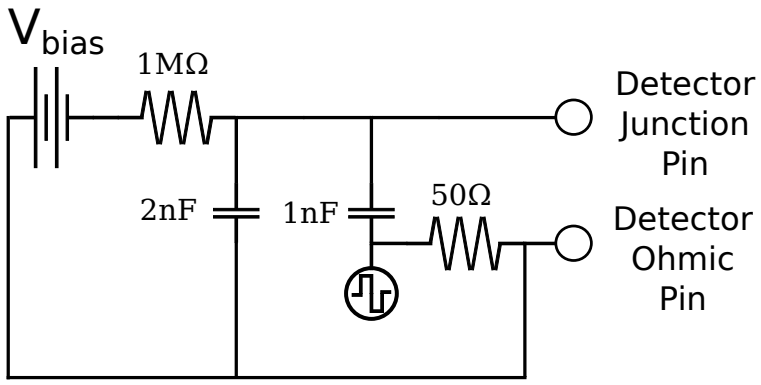

Figure 4.9: Each detector was pulsed by a BNL PB5 precision pulser independently. The pulse was injected through a 1 nF capacitor, which deposited charge on the junction side of the detector.

disk with this direct signal from the pulser. For each recorded waveform, an energy was extracted (see Sec. 5.1.1). For a given bias voltage setting (i.e. a given run), a histogram of measured pulser energies was created. These histograms were fitted to a gaussian distribution, providing a mean and a width for each voltage setting. As the depletion region increased with an increase in bias voltage, these widths became narrower. In effect, the detector resolution increased. The voltage at which there was no appreciable change in detector resolution was chosen as the bias voltage for each detector. This bias voltage results in a "fully depleted" detector. The applied bias was 200 V for the East detector and 300 V for the West detector.

The pulser was also used in a set of runs to study detector linearity. The DAQ again triggered via direct output from the split pulser line. The bias voltage was fixed for each detector, and the amplitude of the pulser output was varied from 50 mV to 0.1 mV, which corresponds to a range of about 550 keV to 1 keV. The pulser rate was set to 1 kHz and data was taken for 100 s for each pulser amplitude setting. Unfortunately it was discovered that the pulser pulse shapes were inconsistent at different amplitude settings. Ultimately a study of system linearity was forced to proceed via the aforementioned calibration sources: ^{139}Ce, ^{113}Sn, and ^{207}Bi.

4.4.2 Production data

For production data, ^{45}Ca, ^{113}Sn, ^{207}Bi, and ^{139}Cesources were used. The ^{45}Ca source was placed in the SCS approximately 75 inches from the West detector mount flange. The ^{45}Ca source remained fixed in this position for all production data taking. The length of a typical run was about 30 minutes. For the first 7 hours of a 24 hour period, data was collected with only ^{45}Ca present in the SCS. At the end of each 7 hour period, two runs were conducted with the ^{113}Sn source. The ^{113}Sn source was placed in the center of the SCS via the load lock. Because the ^{45}Ca source was fixed for all production data, the ^{113}Sn runs also include events from the decay of ^{45}Ca. After the ^{113}Sn data were collected, the source was retracted and the collection of solely ^{45}Ca data resumed for 7 more hours. This collection of ^{45}Ca data for 7 hours followed by an hour long collection of ^{113}Sn and ^{45}Ca data was repeated a total of three times each day. Each detector was pulsed continuously at a rate of 2 Hz and at a voltage of 50 mV. The pulsers were initially synchronized in time. The coupling of the two pulsers introduced an increase in the root-mean-square (RMS) of the background noise by a factor of about 6. Therefore the pulsers were decoupled and allowed to pulse independently. The trigger scheme shown in Fig. 4.10 was used for all production data taking.

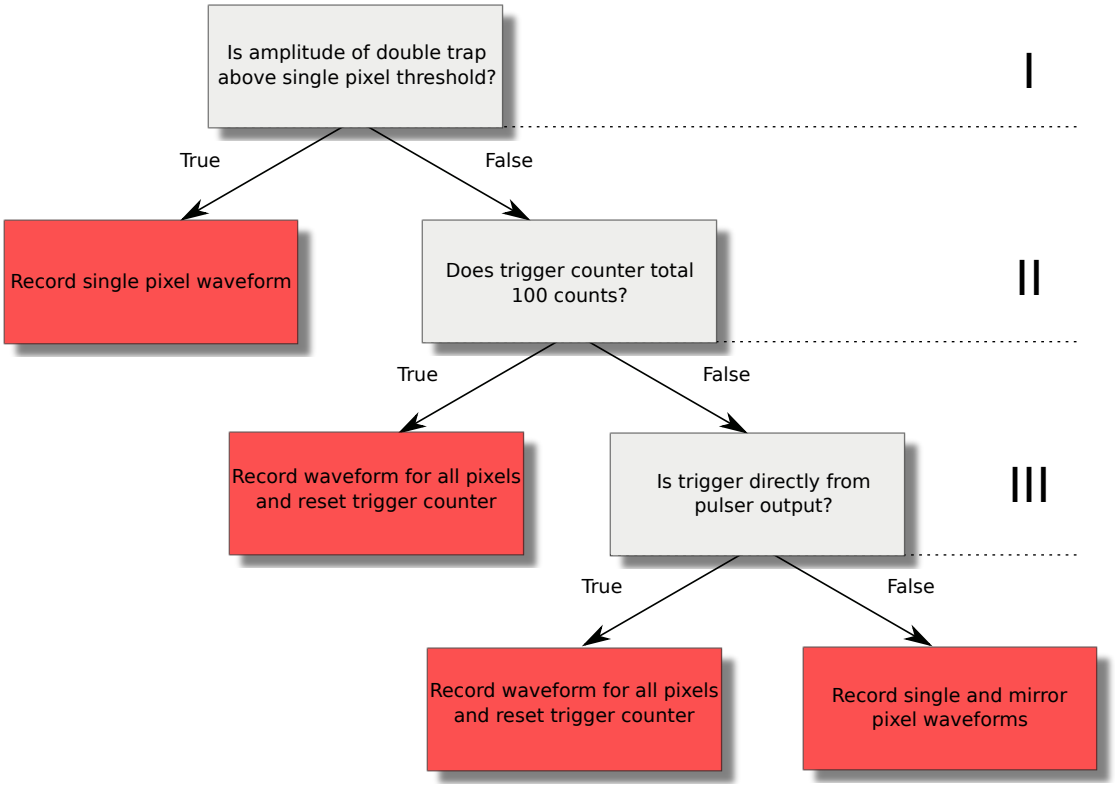

Figure 4.10: Above is the logical progression followed by DAQ FPGA firmware following a triggered event. The first layer (I) is used to determine whether the event was of cosmic origin. The threshold was set such that all source lines were well below this threshold. The second layer (II) was used to sample the detector in a somewhat random fashion. Every 100th trigger resulted the waveforms present on all pixels being written to file. The third layer (III) was used to ensure all pixels were recorded with a trigger generated by the direct signal from the pulser to the DAQ. Otherwise only the pixel which caused the trigger and its corresponding mirror pixel were written to file. The mirrors were recorded to capture low energy backscatters.

Chapter 5

^{45}Ca Analysis

The ^{45}Ca experiment took data to test or further constrain the SM by precisely measuring the ^{45}Ca beta decay energy spectrum (see Chs. 1 & 4 for more detail). The analysis procedure is discussed in the sections to follow this overview. For every waveform recorded by the DAQ, an energy was extracted using a trapezoidal filter based on that of Ref. [76]. ^{113}Sn, ^{207}Bi, and ^{139}Ce source data and Monte-Carlo (MC) simulation performed in PENELOPE were used to calibrate the detector via single-pixel spectra. The single-pixel spectra are composed from events that were well isolated in time to individual pixels. The resulting calibrations were applied. Calibrated single-pixel ^{45}Ca spectra were compared to MC simulation (also carried out in PENELOPE). A value of 'b' was extracted by fitting a combination of 'b'= 0 and 'b'= 1 MC simulation to the observed ^{45}Ca beta spectrum. Additionally, various systematic effects were analyzed and accounted for in the value of 'b' reported here. It should be noted that the development and running of the PENELOPE simulation was performed by the author of Ref. [74].

5.1 Waveform Analysis

Every event recorded consisted of pixel identifiers, a data quality flag, timing information, and a 14 μs waveform trace of preamplifier output sampled by the

DAQ (250 MHZ sample rate). Initially, these waveform traces were fitted to $f(t_i) = A \cdot \left(e^{-(t_i-t_0)/\tau_1} - e^{(t_i-t_0)/\tau_2}\right)$, where A, τ_1 and τ_2 were fit parameters. While initial results were promising, the required computational time as well as difficulties quantifying associated systematic biases introduced by such a fit ultimately resulted in abandoning this method. Instead, A few digital filters were applied to these waveforms to extract energies and determine the underlying structure of each event. Additionally, a linear least square fit of the waveform to an oscillating baseline was performed on a waveform-by-waveform basis. The output of these fits was used as a data quality filter for spectra generation.

5.1.1 Energy Determination

A trapezoidal filter was used to extract the electron energies from amplifier waveforms. The details on the derivation of trapezoid parameters can be found in Ref. [76]. Trapezoidal shaping is ideal for energy extraction, since the waveforms have a short (< 100 ns) rise time and a long (~ 4 μs) exponentially decaying tail. See Fig. 5.1 for trapezoidal filter response. The trapezoidal output is produced by convolving a trapezoidal impulse response (red in Fig. 5.1) and the waveform (blue). The energy is directly proportional to the pulse height of the output. If $h(t)$ is the impulse response, where

$$h(t) = \begin{cases} \tau_{\text{fall}} + t; & 0 < t < \tau_{\text{rise}} \\ \tau_{\text{rise}}; & \tau_{\text{rise}} < t < \tau_{\text{rise}} + \tau_{\text{top}} \\ 2\tau_{\text{rise}} + \tau_{\text{top}} - \tau_{\text{fall}} - t; & \tau_{\text{rise}} + \tau_{\text{top}} < t < 2 \cdot \tau_{\text{rise}} + \tau_{\text{top}} \\ 0; & \text{Otherwise} \end{cases} \tag{5.1}$$

and $v(t)$ the waveform, then the trapezoidal output $s(t)$ is given as:

$$s(t) = \frac{1}{\tau_{\text{rise}}\tau_{\text{fall}}} \int_{-\infty}^{+\infty} v(t')h(t-t')dt' \tag{5.2}$$

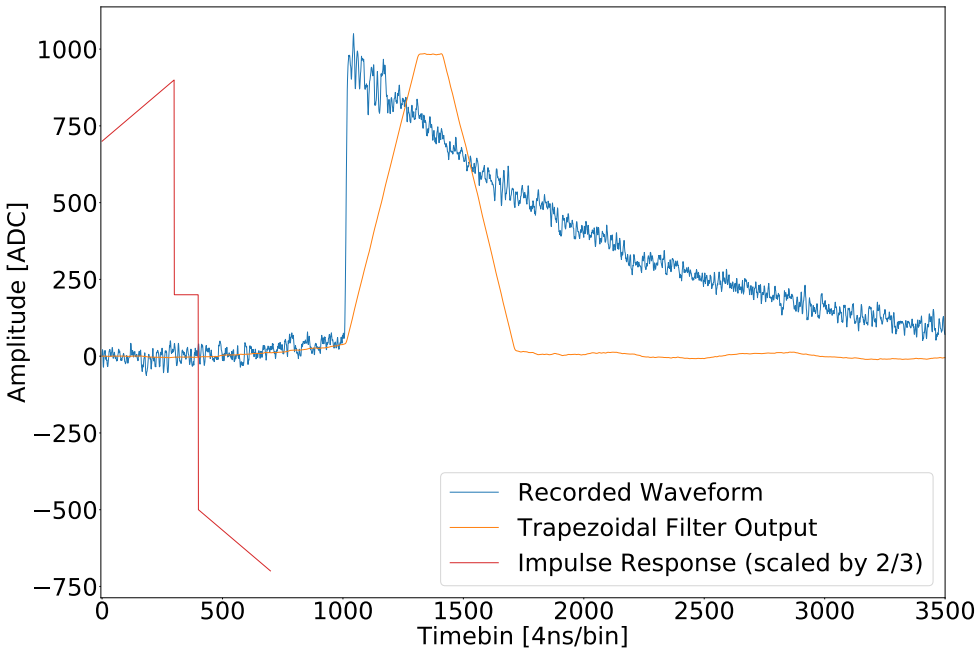

Figure 5.1: The raw waveform for an event (blue) is convolved with the impulse response (red) and yields the trapezoid shape (orange).

For the ^{45}Ca experiment, the amplitude at the midpoint of the flat top of the trapezoid was chosen as the energy of the waveform. This was algorithmically done by first finding the maximum value of the trapezoid $y[t_{\max}]$, where $y[t_i]$ denotes the amplitude of the trapezoidal output of the i'th timebin. Then, the timebins t_a and t_b were determined by requiring that:

$$y[t_a] \leq 0.8 \cdot y[t_{\max}] \leq y[t_{a+1}]$$
$$y[t_b] \geq 0.8 \cdot y[t_{\max}] \geq y[t_{b+1}]$$

The timebin corresponding to the midpoint of the top of the trapezoid can be expressed as $t_{\text{mid}} = t_a + \frac{t_b - t_a}{2}$. Therefore $E(\text{ADC}) = y[t_{\text{mid}}]$. See Fig. 5.2 for an example of this algorithm applied to a waveform.

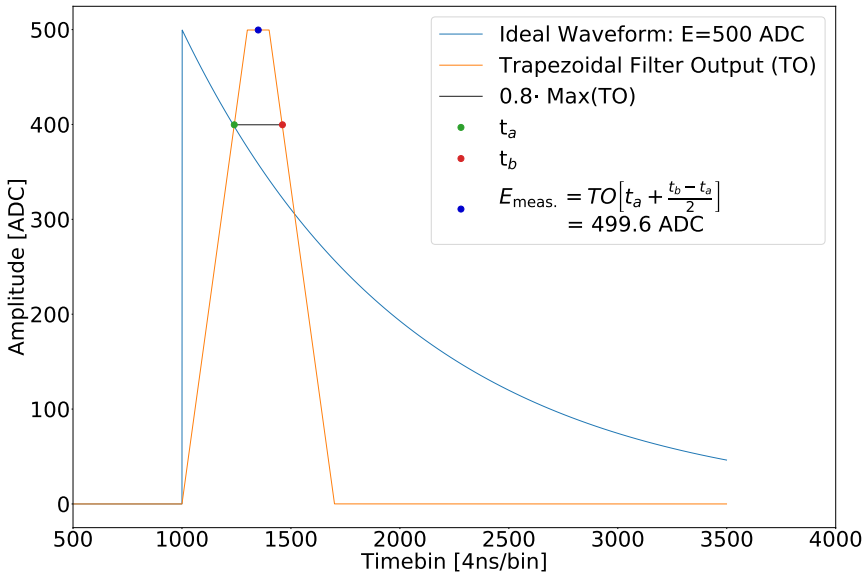

Figure 5.2: The waveform for an idealized event is shown in blue. The trapezoidal filter output $y[t_i]$ is shown in orange. The energy for the waveform is determined by finding the points t_a and t_b, where $y[t_a] \leq 0.8 \cdot y[t_{\max}] \leq y[t_{a+1}]$ and $y[t_b] \geq 0.8 \cdot y[t_{\max}] \geq y[t_{b+1}]$. Then the energy is measured as $E = y\left[t_a + \frac{t_b - t_a}{2}\right]$

5.1.2 Trapezoidal Parameters

The shape of the trapezoid is dependent on the multiple attributes of the waveform from which it was produced. To obtain trapezoids with flat tops, the fall time of the trapezoid filter must be set to the decay constant of the shaping and amplifying electronics. Since the amplifier and shaping components vary slightly from one electronics chain to another, the decay constants, and thus trapezoidal filters, vary from pixel to pixel. To determine these constants, pulser data were used. The pulser data is ideal for such an analysis, as it is free of backscattering which can distort the apparent decay constant of the waveform. Precision BNL PB5 pulsers were capacitively coupled to the detector bias lines through a 1 nF capacitor, see Fig. 4.9. The voltage of the pulsers were set such that the charge injected yielded a signal of roughly 530 keV, well beyond the endpoint of the ^{45}Ca beta spectrum. The frequency was set to 2 Hz. Fig. 5.3 represents a typical distribution of extracted decay constants for pulser events. The distributions for each pixel were fitted with Gaussian shape,

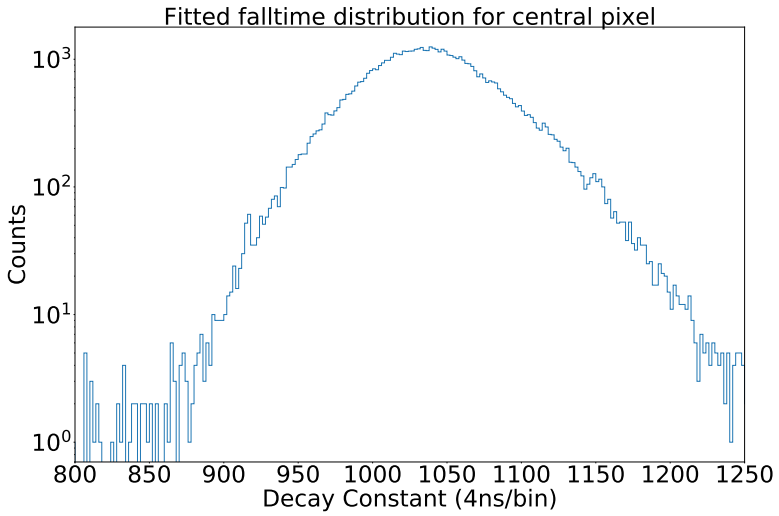

Figure 5.3: A typical distribution of the decay constant observed for pulser events of a central pixel. For each pulser event within a given pixel, the decay constant extracted by fitting the waveform to a decaying exponential function.

and the mean of the fit was used for the trapezoidal decay constant parameter for said pixel.

The two other parameters which define the trapezoidal filter are the shaping time, τ_s, and the *top* parameter. The shaping time determines the length of the rising and falling portion of the trapezoid output. The top parameter corresponds to the length of the top of the trapezoidal output in terms of timebins. It is essentially the number of timebins over which the the filter averages. To determine the optimal parameters, a shaping time and top parameter scan were performed. Since these parameters determine how the trapezoidal filter integrates over and averages noise, the optimal set was chosen by comparing widths of calibration source and pulser peaks for various sets of parameters.

The top parameter and shaping time were varied independently over the square grid of [10, 20, 30, ..., 100, 200, 300, ..., 1000] timebins. For each set of parameters, the corresponding trapezoid filter was used for energy extraction for a set of ^{113}Sn source runs. The 363 keV conversion electron (CE) peak was fitted to a Gaussian distribution

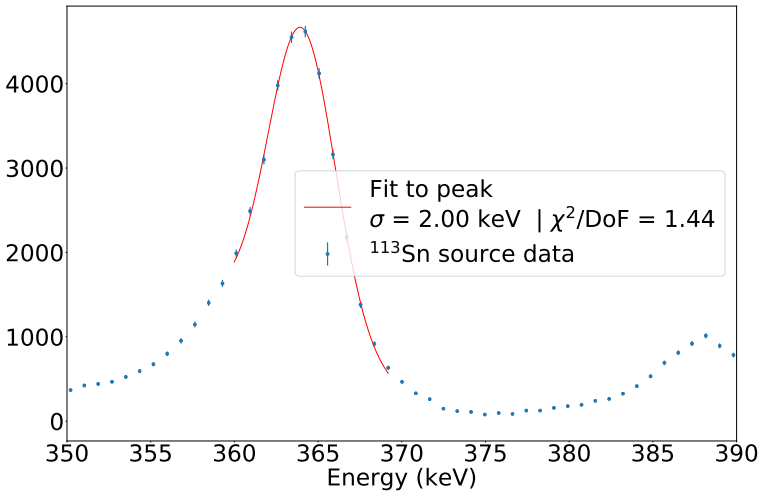

Figure 5.4: For each set of top and shaping time parameters, the ^{113}Sn 363 keV conversion electron peak was fitted to a Gaussian distribution with a linear term and a constant offset.

plus a linear term and a constant offset (see Fig. 5.4 for an example fit). The results of the shaping time scan can be seen in Fig. 5.5.

In terms of energy resolution, a zero length top parameter is ideal (see Ref. [76]). However, for realistic pulses with finite risetimes, the trapezoidal filter output suffers from ballistic deficit. When charge is liberated within a detector, the bias sweeps the charge to the cathode and anode of the detector. The charge collection does not occur instantaneously, but takes some finite amount of time to migrate through the silicon. The shaping electronics exponentially dissipate the charge as it arrives with some decay constant. The difference in amplitude of the output pulse with a finite shaping time and an infinite shaping time is referred to as the ballistic defficit. With an infinite shaping time the shaped output can be integrated to determine the total amount of charge deposited. With a non-infinite shaping time, an additional correction must be applied to determine the total charge deposited. This correction is dependent on the risetime of the pulse, and therefore can vary from pulse to pulse. As discussed in Ref.

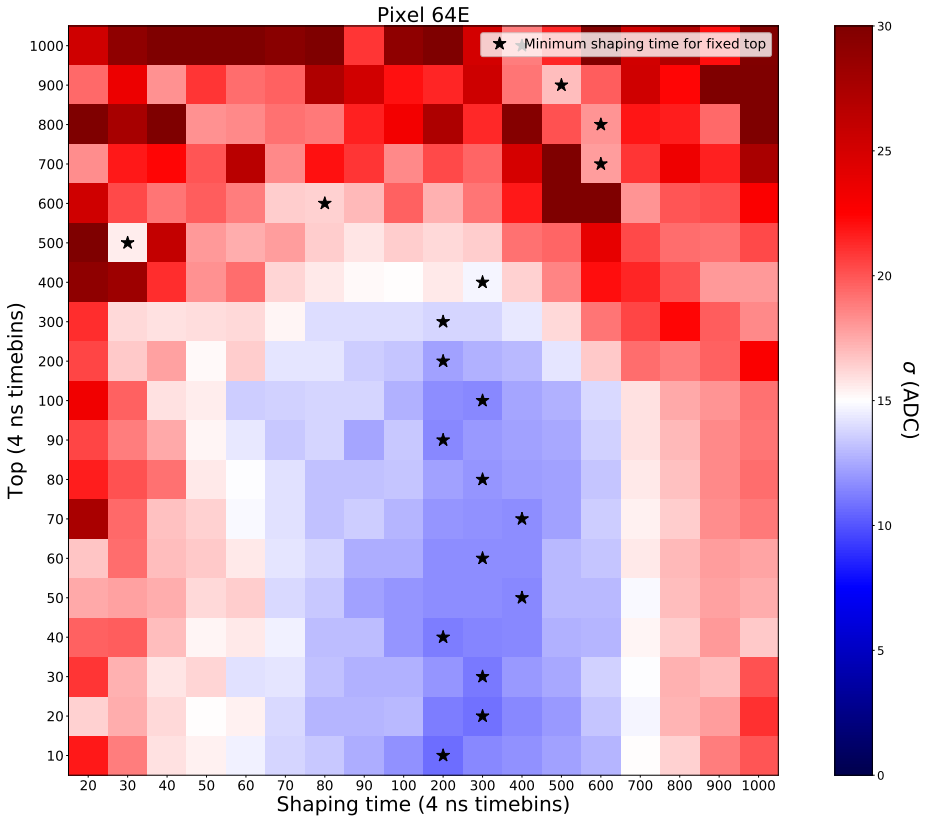

Figure 5.5: Above is a scan of the trapezoidal filter parameter space. The 363 keV ^{113}Sn peak was fit to a gaussian for each set of trapezoidal parameters. The color indicates the width (σ) of the fit.

[57], with a sufficiently long top parameter, the total charge can be extracted from trapezoidal output regardless of any variation in the risetime of the pulse.

Pileup effects must also be taken into consideration with a choice of the top parameter. Pileup (or accidental pileup) refers to an instance where two or more uncorrelated particles deposit energy within the same pixel very close in time. The resulting waveform contains a superposition of the two events and can lead to a distortion in energy extraction. To minimize this effect, the top parameter must be as short as possible. In contrast, a longer top parameter is ideal to accommodate events which backscatter. When a particle deposits energy within the same pixel multiple times, a trapezoidal filter with a top paramater as long as the backscattering process may be used to fully reconstruct the event energy. To capture the full energy for events which backscatter from and back into the same pixel, a top parameter at least as long as the backscattering time window is desirable. By increasing the top parameter, the probability of including an uncorrelated event (accidental pileup) also increases. Hence, the trapezoidal top parameter must be long enough to encompass most backscattering events, but short enough to minimize accidental pileup contamination. A duration of 400 ns (100 timebins) was chosen for the top parameter. In effect, the duration of the top parameter was chosen to be long enough to sum the energy of backscattered events with a maximum of 400 ns between depositions, which encompasses the majority of backscattered events (see Fig. 5.6).

5.1.3 Accidental Pileup & Backscattering Identification

For the ^{45}Ca data, the source activity was roughly 1 kBq. This corresponds to an event rate of 1-2 kHz, or a period of 500 to 1000 μs. The DAQ acquired samples that were 14 μs in duration, so $\frac{14\mu s}{500 \text{ to } 1000\mu s} = 1.4 - 2.8\%$ of the data should contain accidental pileup. These accidentals distort the trapezoidal filter energy extraction if the time separating the two events is less than the length of the trapezoidal filter. That is, if the trapezoidal filter is 3.48 μs long, any accidental pileup will distort

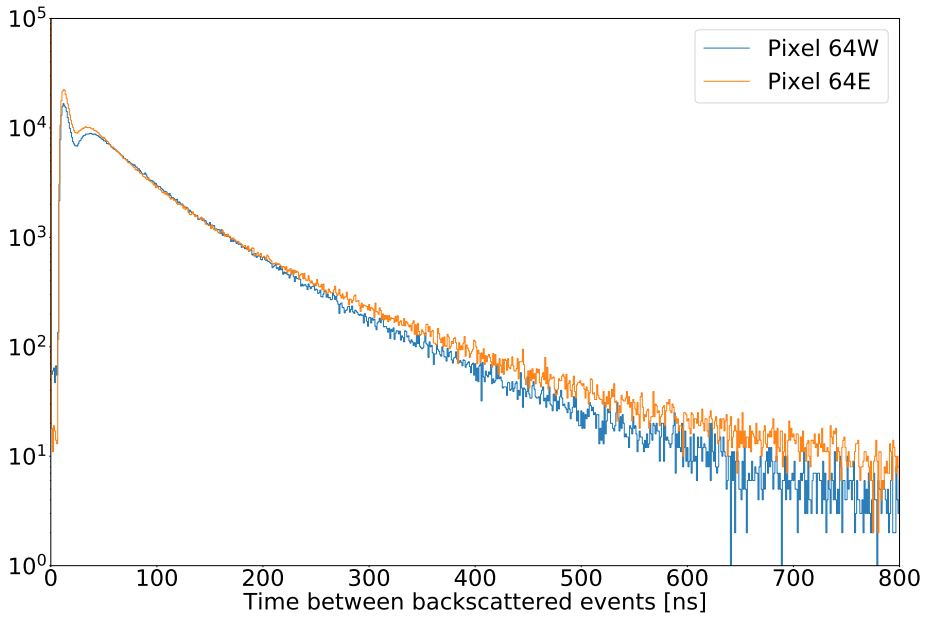

Figure 5.6: Above, the backscattering time distribution is shown for simulation. More than 99.7% of the data falls within a window of 400 ns.

the energy extraction for the primary event if the accidental occurs less than 3.48 μs before or after the primary event (see (a) of Fig. 5.7). To detect such events, a short trapezoidal filter was also implemented.

As previously discussed, the length of the top parameter was chosen to be long enough to encompass the backscattering time window. With such a choice, the trapezoid output integrates the deposited backscatteerd energy. Knowing that backscatter occurred is necessary however, because for each hit in a backscatter event, the particle passes through the dead layer ($\sim$ 100nm SiO) and and loses some amount of energy as it travels. Thus in order to correctly reconstruct the events total energy, it is necessary to identify and count the number of transits through the dead layer.

By convolving a waveform with a shorter trapezoidal filter, the response will also be narrower and therefore have better timing. The trapezoidal filter used for energy extraction was 3.48 μs long and thus cannot easily and systematically distinguish between multiple events that occur within this time window. To detect waveforms with accidental pileup, a much shorter trapezoidal filter with $\tau_s = 40$ ns and a top

parameter of 4 ns was used (see (b) of Fig. 5.7). This filter was able to detect events with energies down to 20 keV and a separation of roughly 100 ns or more between the primary event and the accidental. If the short trapezoidal output for an event contained more than one peak above threshold, the time difference between the two largest peaks was used to categorize the event. If this time difference was larger than the chosen coincidence window, the event was considered to contain accidental pileup (see Fig. 5.8 for the effect of the removing events with accidental pileup). From $\gamma m_e c^2 = E = T + m_e c^2$ where $\gamma = (1 - \frac{v^2}{c^2})^{-1/2}$ and T is the electron kinetic energy, it follows that $v_e = \left(1 - \frac{m_e c^2}{E^2}\right)^{1/2} c$. The energy threshold applied to production data was 50 keV, so $v_e > 0.3c$. Now the distance between the two detectors was $\sim$ 5m, and the time taken for an electron to traverse the spectrometer is $t_{\text{transit}} = \frac{5\text{m}}{v_e}$. For electrons with $T > 50$ keV, $t_{\text{transit}} < 56$ns. For a given coincidence window $t_{\text{coinc.}}$, the number of times the slowest electron can backscatter between the two detectors is very roughly $\frac{t_{\text{coinc.}}}{t_{\text{transit}}}$. A coincidence window of 400 ns was chosen, so then $\frac{t_{\text{coinc.}}}{t_{\text{transit}}} = \sim 7$, with this window. At these energies and with the given source-detector-magnetic field geometries, 30% of the electrons that interact with a detector should backscatter (see Fig. 5.9 for a distribution of the number of backscatters per event). Hence these coincidence windows allow for a potential backscatter collection efficiency of up to $1 - 0.3^{t_{\text{coinc.}}/t_{\text{transit}}} > 99.98\%$.

5.1.4 Baseline Oscillation

As mentioned in Ch. 3, data taken prior to the 2017 set exhibited oscillations attributed to the physical shaking of the cooling line (see Fig. 3.5). Switching from LN_2 to cold gaseous helium significantly reduced the amplitude of the microphonics, however it was not altogether eliminated from the data. The period of the oscillations observed in the waveform data was on the order of the length of the waveform, $T_{\text{osc.}} \sim 14$ μs or $\omega = \frac{2\pi}{T} \sim 225$ kHz. The length of the optimal trapezoidal filter is ~ 3.5 μs. Because the period of the baseline oscillation is comparable to the length

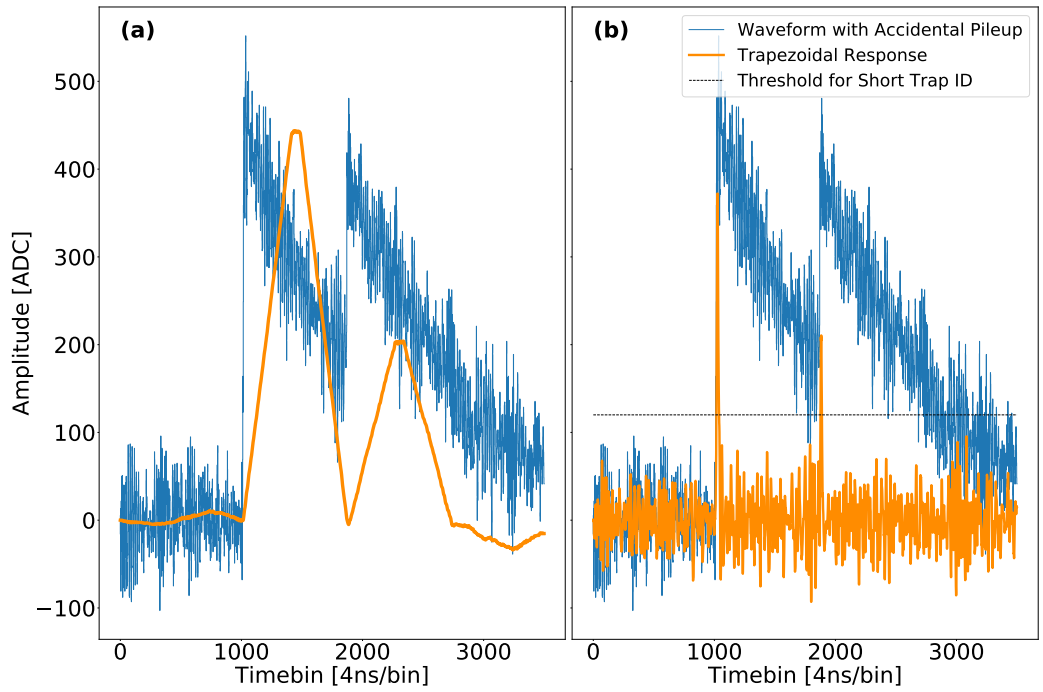

Figure 5.7: When an accidental event occurs within 3.48 μs of the primary event, the trapezoidal response of each begin to overlap and sum. In **(a)**, the accidental was synthetically placed exactly 3.48 μs (870 timebins) after the primary event for illustrative purposes. In **(b)**, the short trapezoidal filter is used to identify the two events.

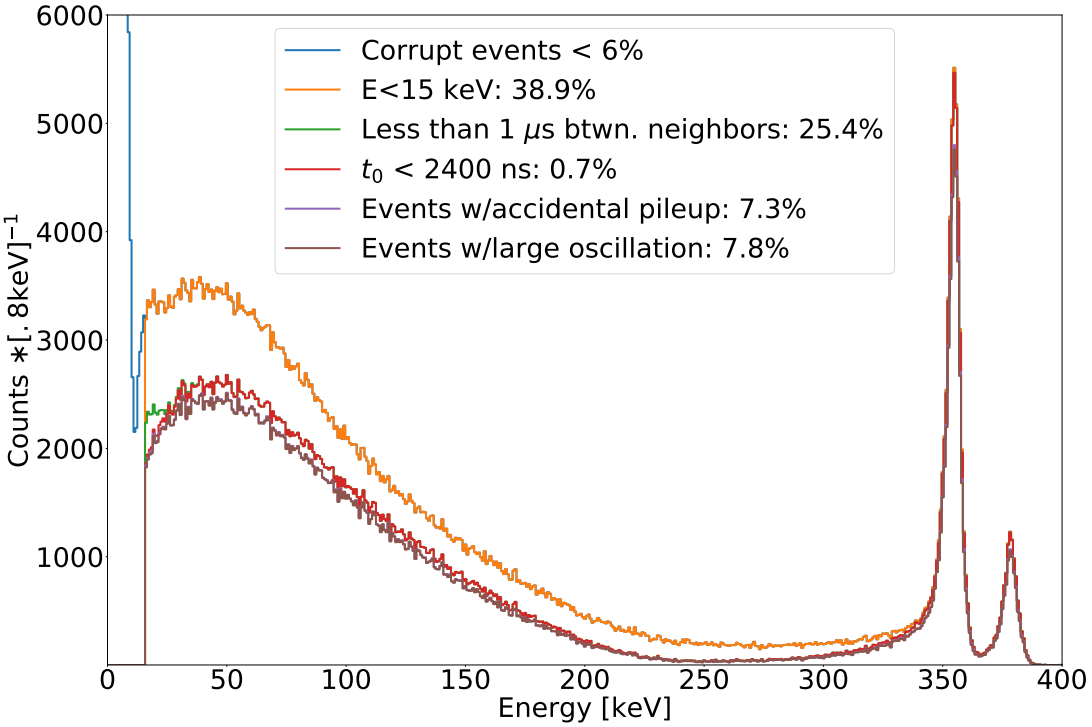

Figure 5.8: Above depicts the effect of each data cut on the shape of the ^{45}Ca and ^{113}Sn spectra. The percentages reported are the percentage of events that were removed by the described cut.

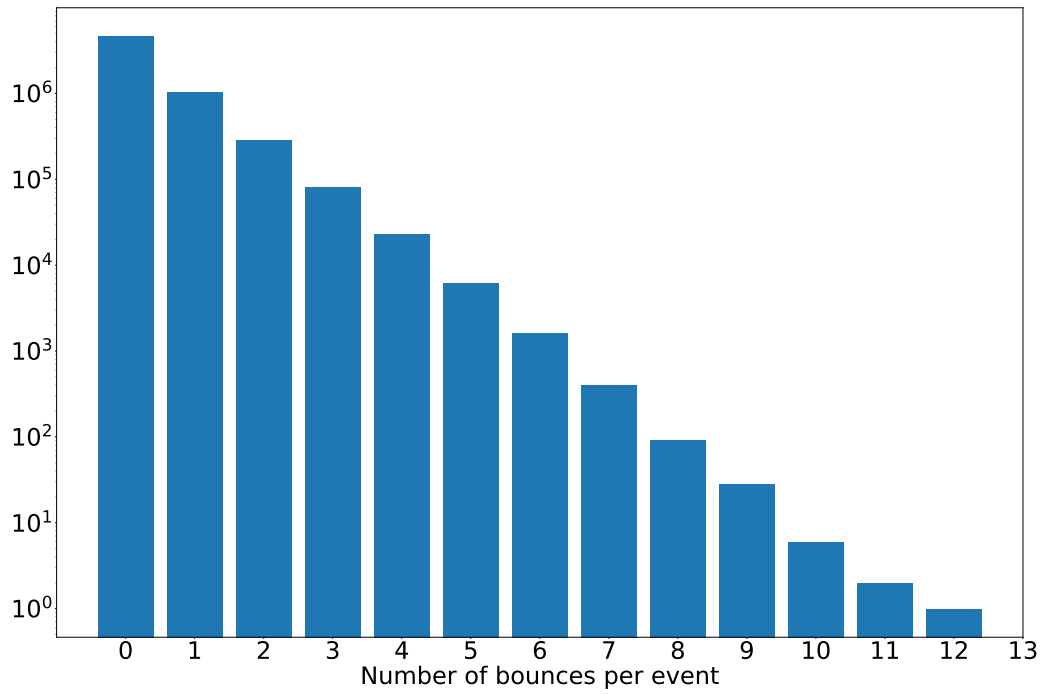

Figure 5.9: Above is a histogram of the number of times decay particle backscatters within a Monte-Carlo ^{45}Ca simulation. See Sec. 5.2 for a description of the simulation.

of the trapezoidal filter, the effect of the oscillation does not average to zero within individual pulses. This effect distorts the trapezoidal output and degrades overall energy resolution. To combat this problem, a linear least square (LLS) fit to an oscillating baseline was implemented.

Linear Least Squares Fitting

The inner product of two functions $f : \Re \to \Re$ over some continuous domain $t \in [a, b]$ is:

$$\langle f, g \rangle := \int_a^b f(t)g(t)dt \tag{5.3}$$

Then over a discrete domain $[t_0, t_1, \ldots, t_m]$, the inner product is defined

$$\langle f, g \rangle := \sum_{i=0}^{m} f(t_i)g(t_i)\Delta t_i \tag{5.4}$$

Now if $\Delta t_i = \text{const.}$ for all i, Δt_i contributes an overall multiplicative factor and Eqn. 5.4 becomes: $\langle f, g \rangle = m \cdot \Delta t \sum_{i=0}^{m} f(t_i)g(t_i)$. Since this factor is the same for all inner products, it may simply be dropped, leaving:

$$\langle f, g \rangle = \sum_{i=0}^{m} f(t_i)g(t_i) \tag{5.5}$$

Now suppose that a waveform Y of m timebins can be described by n functions f_j. Then the i'th component of the waveform is given as:

$$y_i := \sum_{j=0}^{n} \alpha_j f_j(t_i) \tag{5.6}$$

where $\langle f, f \rangle = \sum_{i=0}^{m} \left(f(t_i)\right)^2 = 1$ and $\alpha_j \in \Re$. Then a matrix A can be defined such that:

$$A_{ij} := f_j(t_i) \tag{5.7}$$

$$A = \begin{bmatrix} f_0(t_0) & f_1(t_0) & \dots & f_n(t_0) \\ f_0(t_1) & f_1(t_1) & \dots & f_n(t_1) \\ \vdots & \vdots & & \vdots \\ f_0(t_m) & f_1(t_m) & \dots & f_n(t_m) \end{bmatrix}$$

Then $Y = A\hat{\alpha}$, with $[\hat{\alpha}]_i = \alpha_i$. Note that $A^T \cdot A$ is an m by m square matrix. Therefore if $A^T \cdot A$ is an invertible matrix, $\hat{\alpha}$ may be obtained:

$$\hat{\alpha} = (A^T \cdot A)^{-1} A^T \cdot A\hat{\alpha} = (A^T \cdot A)^{-1} A^T \cdot Y \tag{5.8}$$

For the ^{45}Ca data, the functions used were $f_0 = 1$, $f_i = \sin(\omega_i \cdot t)$, $f_{i+1} = \cos(\omega_i \cdot t)$ where i is one of N frequencies, and $f_{2N+1} = \left(e^{\frac{t-t_0}{\tau_{\text{fall}}}} - e^{\frac{t-t_0}{\tau_{\text{cc}}}}\right)\Theta(t-t_0)$ where Θ is the heaviside function. The first term in $f_{2N+1}(t)$ is the standard exponentially decaying signal, and the second term takes in to account the finite rise time of the signal. τ_{cc}= 20 ns was used. Figure 5.10 demonstrates the LLS fit to a particular ^{45}Ca waveform.

5.1.5 Baseline oscillation effect on a trapezoidal filter

The impulse response is given as Eq. 5.1. If there exists baseline oscillations, then the input signal can be written as $v(t) = v_0(t) + f(t)$ where $v_0(t) = \Theta(t-t_0) \cdot Ae^{-\frac{t-t_0}{\tau}}$ and $f(t) = B\sin(\omega t + \phi)$. Thus the trapezoidal output can be written as:

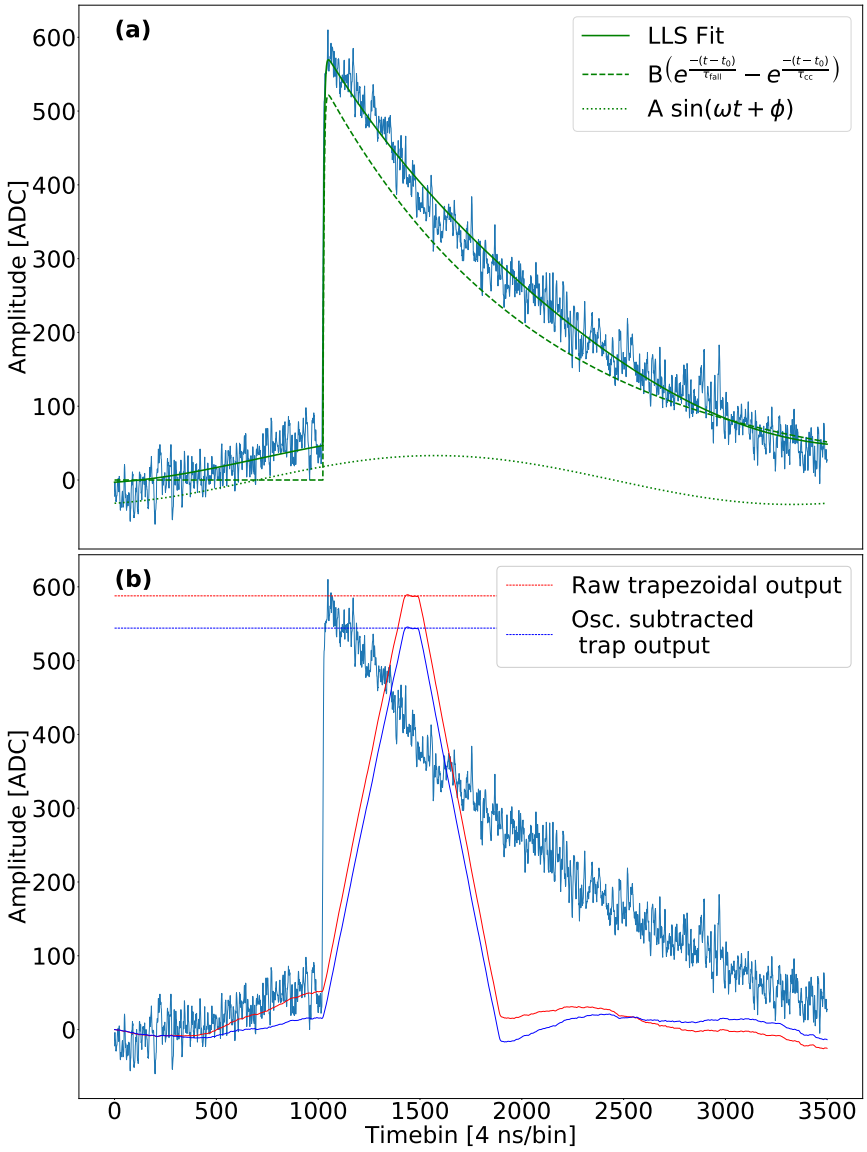

Figure 5.10: **(a)** Each individual function of the LLS fit are shown. The overall fit has a $\chi^2/\text{DoF} = 519$ ADC^2. Given that this value is an estimate of σ^2, the fit corresponds to an estimated $\sigma = 22$ ADC. This agrees well with calculations of the root-mean-square noise for baseline data where σ ~20-30 ADC for this pixel. **(b)** Shows the difference in trapezoidal output between the uncorrected (red) waveform and the trapezoidal output of the waveform with the oscillation removed (blue). In this instance, the differnce is 42 ADC or around 5 keV.

$$s(t) = s_0(t) + s_1(t) := \frac{1}{\tau_{\text{rise}}\tau_{\text{fall}}} \int_{-\infty}^{\infty} h(t-t')v_0(t')dt' + \frac{1}{\tau_{\text{rise}}\tau_{\text{fall}}} \int_{-\infty}^{\infty} h(t-t')f(t')dt' \tag{5.9}$$

The first integral results in the standard trapezoidal output, and the second term, $s_1(t)$, is the contribution of the oscillation.

$$s_1(t) = \frac{1}{\tau_{\text{rise}}\tau_{\text{fall}}} \int_{-\infty}^{\infty} h(t-t')f(t')dt' = \frac{B}{\tau_{\text{rise}}\tau_{\text{fall}}} \int_{-\infty}^{\infty} h(t-t')\sin(\omega t' + \phi)dt' \tag{5.10}$$

Let $x := t - t'$, with $dx = -dt'$. Then Eq. 5.10 may be written as:

$$s_1(t) = \frac{-B}{\tau_{\text{rise}}\tau_{\text{fall}}} \int_{\infty}^{-\infty} h(x)\sin(\omega(t-x) + \phi)dx \tag{5.11}$$

Then the nonzero terms are:

$$\begin{aligned} s_1(t) = \frac{-B}{\tau_{\text{rise}}\tau_{\text{fall}}} \Big(& \int_{\tau_{\text{rise}}}^{0} (\tau_{\text{fall}} + x) sin(\omega(t-x) + \phi)dx \quad + \\ & \int_{\tau_{\text{rise}}+\tau_{\text{top}}}^{\tau_{\text{rise}}} \tau_{\text{rise}} \cdot \sin(\omega(t-x) + \phi)dx \quad + \\ & \int_{2\tau_{\text{rise}}+\tau_{\text{top}}}^{\tau_{\text{rise}}+\tau_{\text{top}}} (2\tau_{\text{rise}} + \tau_{\text{top}} - \tau_{\text{fall}} - x)\sin(\omega(t-x) + \phi)dx \Big) \end{aligned} \tag{5.12}$$

Now $\int_b^a x\sin(\omega(t-x)+\phi)dx = \frac{x}{\omega}\cos(\omega(t-x)+\phi) + \omega^{-2}\sin(\omega(t-x)+\phi)|_b^a$ and $\int_b^a \sin(\omega(t-x)+\phi)dx = \omega^{-1}\cos(\omega(t-x)+\phi)|_b^a$. Therefore Eq. 5.10 becomes:

$$
\begin{aligned}
s_1(t) = \frac{-B}{\tau_{\text{rise}}\tau_{\text{fall}}}\Bigg(& \frac{\tau_{\text{fall}}}{\omega}\cos(\omega t+\phi) + \frac{\sin(\omega t+\phi)}{\omega^2} \\
& - \frac{\tau_{\text{fall}}+\tau_{\text{rise}}}{\omega}\cos(\omega(t-\tau_{\text{rise}})+\phi) - \frac{\sin(\omega(t-\tau_{\text{rise}})+\phi)}{\omega^2} \\
& + \frac{\tau_{\text{rise}}}{\omega}\left[\cos(\omega(t-\tau_{\text{rise}})+\phi) - \cos(\omega(t-\tau_{\text{rise}}-\tau_{\text{top}})+\phi)\right] \\
& + \left(\frac{\tau_{\text{rise}}-\tau_{\text{fall}}}{\omega}\right)\cos(\omega(t-\tau_{\text{rise}}-\tau_{\text{top}})+\phi) - \frac{\sin(\omega(t-\tau_{\text{rise}}-\tau_{\text{top}})+\phi)}{\omega^2} \\
& + \frac{\tau_{\text{fall}}}{\omega}\cos(\omega(t-2\tau_{\text{rise}}-\tau_{\text{top}})+\phi) - \frac{\sin(\omega(t-2\tau_{\text{rise}}-\tau_{\text{top}})+\phi)}{\omega^2}\Bigg)
\end{aligned}
\tag{5.13}
$$

Now the energy of each event is determined by the midpoint of the trapezoidal output, $E = s(\tau_{\text{rise}} + \frac{\tau_{\text{rise}}+\tau_{\text{top}}}{2})$. Therefore the root-mean-square of the contribution of the oscillation to the energy determination is:

$$
\sigma_{osc.} = \sqrt{\frac{1}{\tau_{\text{top}}}\int_{\tau_{\text{rise}}}^{\tau_{\text{rise}}+\tau_{\text{top}}} (s_1(t))^2 dt} \tag{5.14}
$$

Again for the ^{45}Ca data set, $\tau_{\text{rise}} = 300$ timebins, $\tau_{\text{top}} = 100$ timebins, and $\tau_{\text{fall}} \sim 1100$ timebins. For this data set, the relevant observed oscillation frequencies range from tens to a couple hundred kHz. Because the waveform itself is only 14 μs in length, only a fraction of the oscillation is observed within a single waveform. Hence the the magnitude of the contribution also depends on the phase ϕ of the oscillation. Then with a frequency of 60 kHz, this contribution results in a maximum uncertainty of $\sigma_{osc.} = 0.841 \cdot B$, where B is given in ADC bins.

Microphonic Frequency

As discussed above, the oscillation frequency ω is fixed for each LLS fit. As such, standard non-linear fits of baseline data to a constant plus an oscillating function were performed for several different runs taken at various points throughout the experiment. These data were fit to $f(t) = A\sin(\omega t) + B\cos(\omega t) + C$, where A, B, C

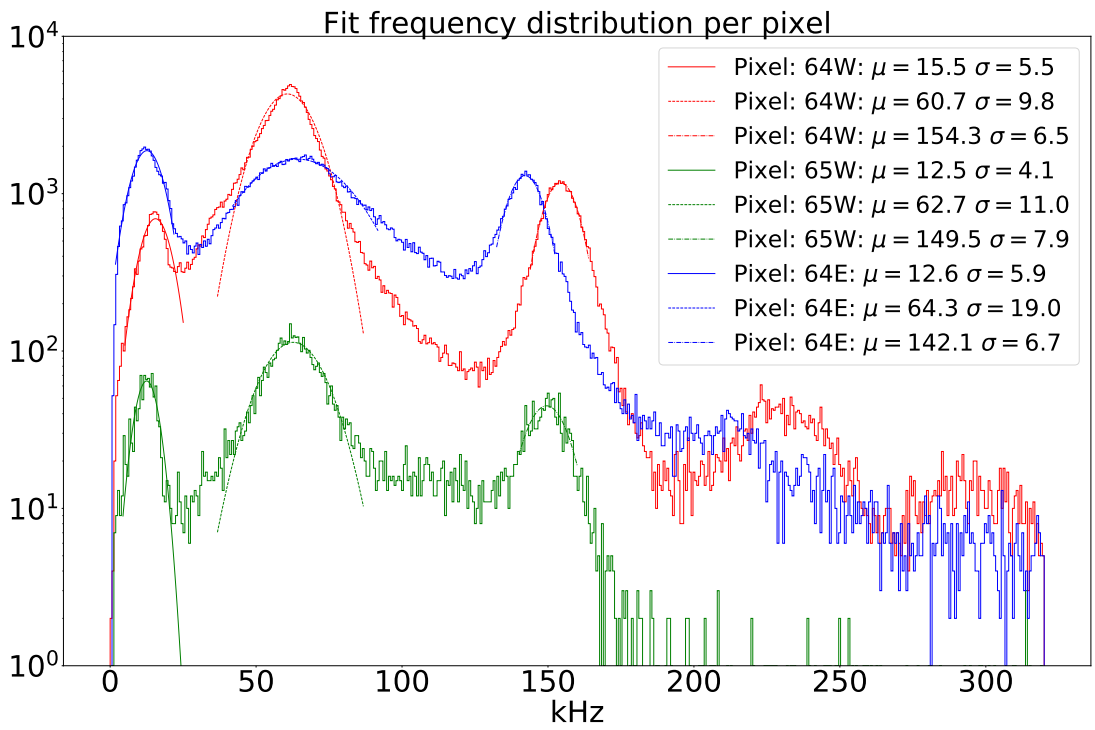

Figure 5.11: Above shows the distribution of frequencies observed (fitted) for the pixels included in these analyses.

and ω are fit parameters. The waveforms were chosen such that the output of the trapezoidal filter described in Sec. 5.1.1 had a maximum amplitude less than 50 ADC, or 8 keV. The distribution of fitted frequencies for a particular set of runs can be seen in Fig. 5.11.

The lowest frequency peak in the 10-15 kHz range was not used for the LLS fits. With a frequency of about 12 kHz, the calculation in Eq. 5.14 yields an uncertainty in the range of $0.008 \cdot B < \sigma_{osc.} < 0.46 \cdot B$, depending on the phase of the oscillation. The typical amplitudes of these low frequency oscillations ranged from 0 to 75 ADC bins. Then in terms of keV, the maximum uncertainty in the trapezoidal output introduced by these oscillations is less than 5.7 keV. The higher frequency peak around 130 kHz was also discarded for the LLS fits. The data are still being analyzed, however, it appears that these frequencies result when a waveform exhibits various noise features

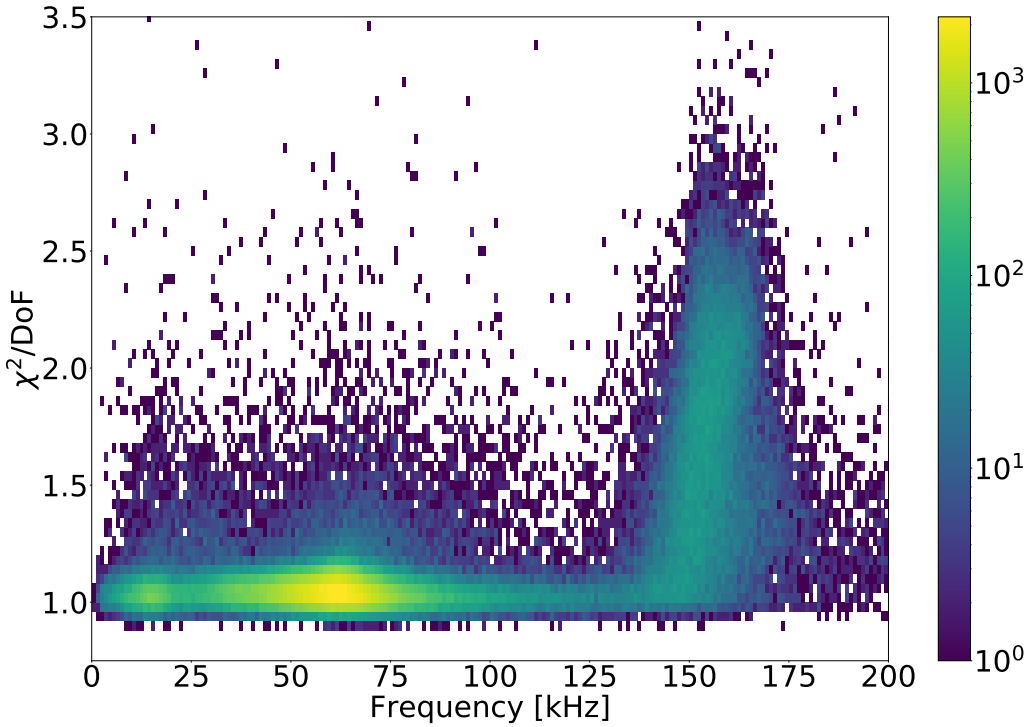

Figure 5.12: In the above 2D histogram, the reduced χ^2 value is plotted as a function of frequency. The fits which resulted with $f > 125$ kHz typically corresponded to events with non-oscillatory noise present in the waveforms. Hence the fits were poorer and the reduced χ^2 values were larger.

with a non-oscillatory behavior (see Fig. 5.12 for a distribution of frequencies versus χ^2/Dof values.

As will be discussed below, the three pixels over which ^{45}Ca beta decay electrons were collected were the central pixels of each detector and pixel 65 of the West detector. The observed fit frequency distribution for these three pixels is shown in Fig. 5.11. The overlap of the $\sim$ 62 kHz peak between the thee relevant pixels allows for a single frequency to be used for every LLS waveform fit, regardless of pixel.

To determine whether this frequency varies as a function of time, this fit procedure was applied to a number of runs which were well separated in time ($\sim$ hours to days apart). Additionally this list of runs spans very early runs to the very final run taken in 2017. As shown in Fig. 5.13, the observed peak frequencies locations do not substantially deviate from run to run. As such, the frequency used within the LLS

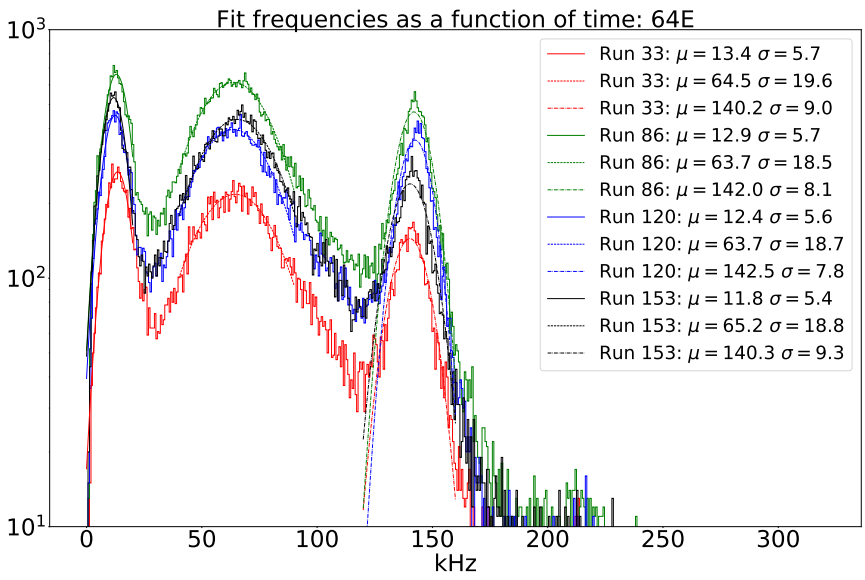

Figure 5.13: Above shows the fitted frequency distribution of baseline data for a sampling of runs taken for the central pixel of the East detector. Since the variation over the above set of runs is very small (< 2 kHz over the set for any peak), the fit frequencty may be fixed for all data runs.

fits were fixed for all runs, as the fit amplitude of oscillation is only used to reject a particular event. Fig. 5.14 shows the effect of the cuts for several different amplitudes.

5.2 Monte-Carlo Spectrum Generation

Before proceeding to building spectra from the aforementioned waveform analysis, a discussion of the Monte-Carlo simulation will first be presented. The MC simulation provides both a means to extract 'b' by direct comparison to data and a route to determine critical underlying systematic uncertainties that would be otherwise inaccessible.

5.2.1 Physical Geometries

The experiment was conducted in the magnet of Ref. [51]. Hence, material and magnetic field geometries of the SCS were also used (with the permission of the

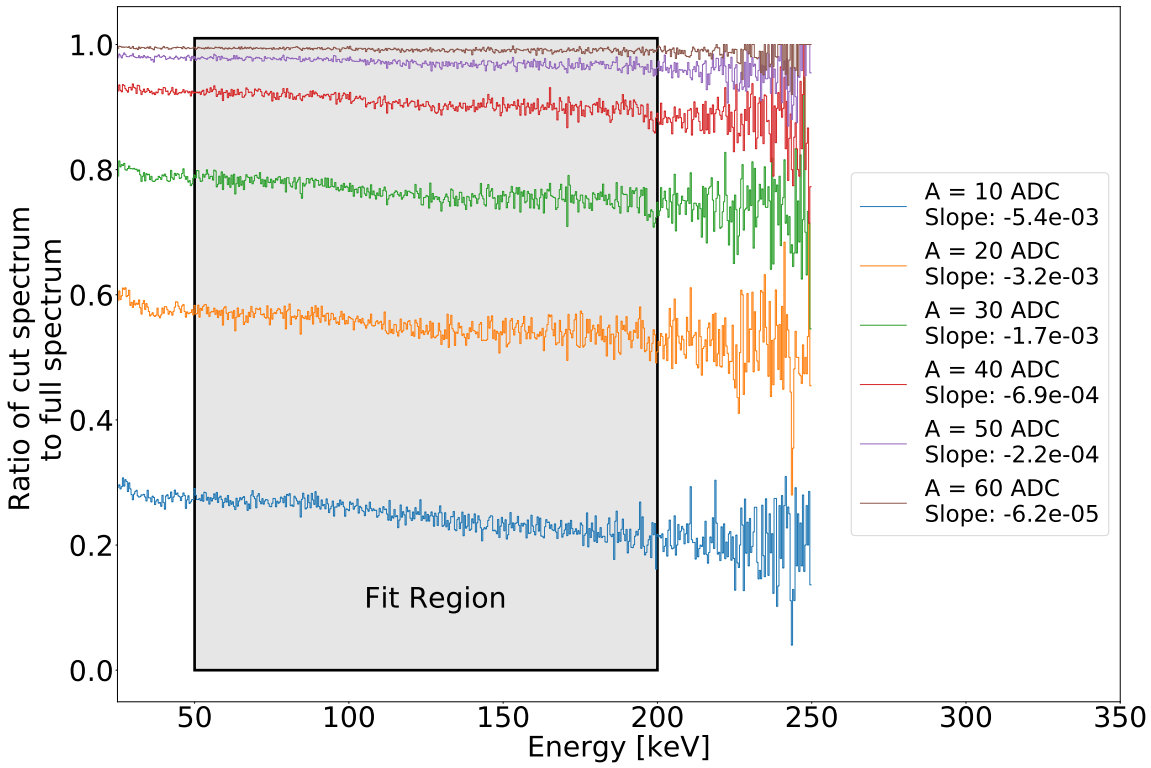

Figure 5.14: Shown above is the effect of various ^{45}Ca spectrum cuts based on LLS fit amplitudes. The quantity of interest is A, the oscillation amplitude. For a given amplitude A (in ADC), the ^{45}Ca spectrum was cut by removing events with oscillation amplitudes greater than A. The resulting spectra were then divided bin-by-bin by the un-cut (in terms of oscillation amplitudes) spectrum. The ratio of these two spectra were then fit to a line. The slopes listed are given in counts per keV. At the endpoint, the largest contribution from the linear term is less than two counts.

collaboration) for the ^{45}Ca experiment. In place of the UCNA detectors of Ref. [51], the silicon detectors of Ref. [61, 62] were used in the simulation.

5.2.2 Generating Ideal and Realistic Source Spectra

All sources were located at least 1.9 m from a detector. As such, photon detection was heavily suppressed by the solid angle occupied by the detectors with respect to the source location ($\Omega < 2 \times 10^{-4}$ sr). Hence, transitions which involved emission of a photon are negligible. The MC therefore was only concerned with nuclear transitions which involved the emission of an electron. For ^{113}Sn, ^{207}Bi, and ^{139}Ce, the energies and the relative intensities of the simulated source were obtained from Ref. [77]. The conversion coefficients were calculated via Ref. [78]. The ^{45}Ca beta spectrum distribution was obtained from and in collaboration with Ref. [64].The simulation proceeded as follows:

A particle with some energy, position, and momentum is generated according to the aforementioned probabilities and geometries. This particle corresponds to some assigned event number. The initial energy, momentum and position. The particle then propagates through the source foil and to the detector. PENELOPE handles the particle's interactions with the magnetic field and materials. In effect, the PENELOPE code takes into account the majority of the physical processes through which a decay electron can lose energy, which includes foil losses, dead layer losses, and bremsstrahlung losses. When the particle first deposits some energy within a detector, the amount energy deposited and location of deposition (pixel) are recorded. If and when a backscatter occurs, the simulation also records each subsequent deposition of energy. The amount of energy deposited, the location and time since initial deposition are recorded. Then these energies are smeared (convolved with a gaussian distribution) according to the measured resolution of the detection system. This is called the electronic response function and will be discussed further in Sec. 5.4. The energy spectrum at the generator stage will be referred to as the

ideal spectrum; while the resulting spectrum after particle transport will be referred to as the *intermediate* spectrum. The spectrum resulting from the convolution of the intermediate MC spectrum with a gaussian will be referred to as the *realistic* spectrum. See Fig. 5.15 for a comparison of the ideal and realistic spectra for the sources used for this experiment.

5.2.3 Electronic Response Function

The shaping electronics varied from pixel to pixel. Hence the electronic response function was determined on a pixel-by-pixel basis: $\Phi \rightarrow \Phi_{\text{pixel}}$. For this analysis, Φ was modeled as a Gaussian distribution. To determine the appropriate width of the distribution for each pixel, the following procedure was carried out.

1. An approximate calibration was applied by simply matching the maximum of the ^{113}Sn 363 keV simulated source peak to data.

2. Then σ was estimated by comparing realistic MC spectra to roughly calibrated data. This was done by convolving intermediate MC spectra with Φ at various values of the detector response width σ. This was done by eye only to get an estimation of σ.

3. A calibration was carried out as described above in Sec. 5.3.2, where the realistic MC source spectra were generated with the current value of σ.

4. An updated value for σ was determined by fitting the convolution of a gaussian of width σ with intermediate MC source spectra to calibrated data.

5. If $\frac{\delta\sigma}{\sigma} > 0.01$, return to 3 and repeat.

Shown in Fig. 5.16 is a comparison of calibration source data taken and the realistic MC spectra for said sources.

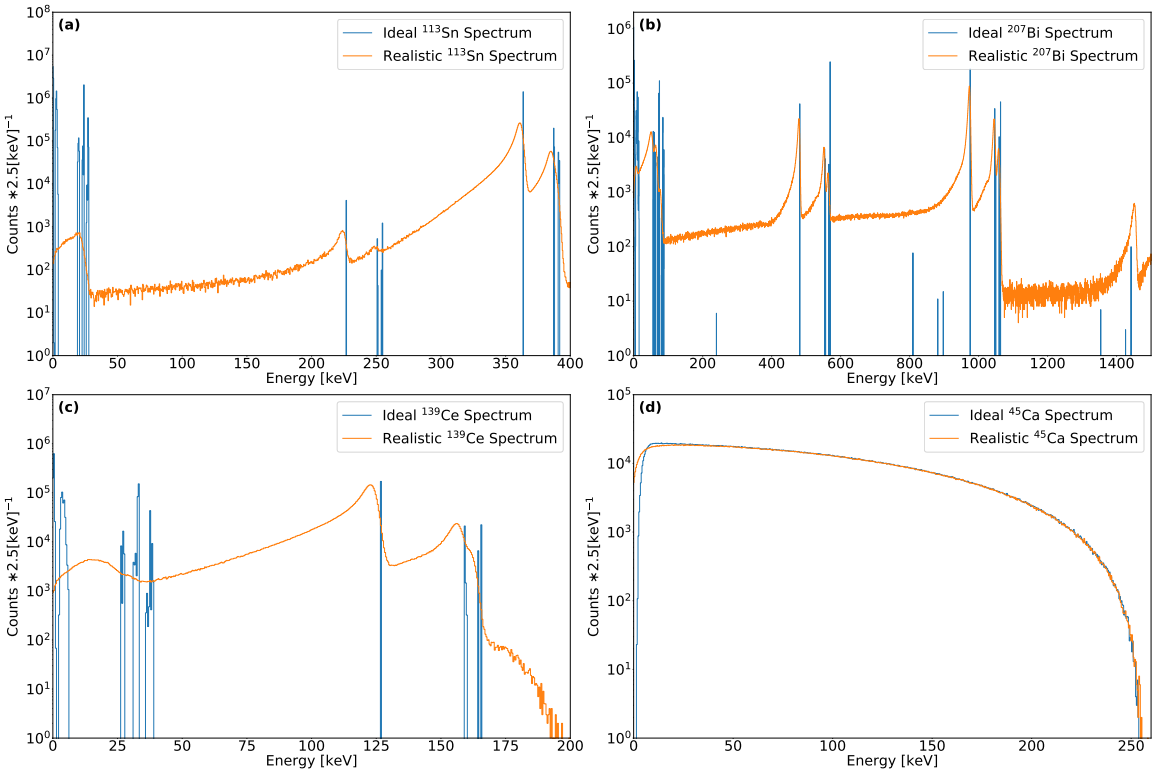

Figure 5.15: Above are the ideal and realistic MC spectra for ^{113}Sn, ^{207}Bi, ^{139}Ce, and ^{45}Ca. The ideal spectra correspond to the source spectra prior to energy loss mechanism such as bremsstrahlung and inelastic scattering losses. The realistic spectra result after these energy loss mechanisms have been applied by PENELOPE.

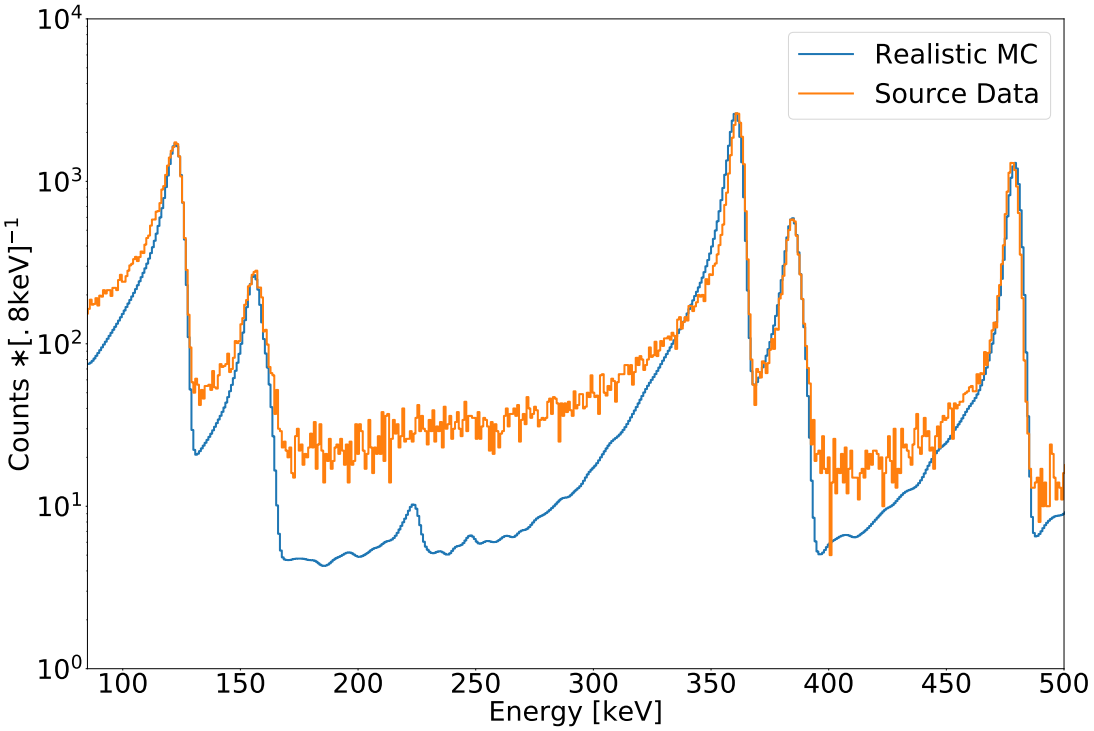

Figure 5.16: Above is the comparison of realistic MC calibration source spectra compared to data collected for pixel 52W. Realistic MC spectra were generated by fitting the output of the PENELOPE simulations convolved with a gaussian to the observed spectrum (blue), with the width of the gaussian as a free parameter.

5.2.4 Generating MC Waveforms

For calibration and system linearity described below, the realistic source spectra were sufficient. However for quantifying various systematic uncertainties and for a 'b' extraction, a third iteration of the simulation was generated. To further emulate the data collected, a simulated waveform was generated for each event of realistic MC spectra. The waveform includes all backscattered events which deposit energy in multiple instances within a given pixel, with relative timing with respect to the initial deposition calculated by PENELOPE. The shape of the waveform was generated by running a step function, an approximate current pulse, through a $CR - RC^2$ filter with pixel dependent decay times. These decay times were chosen to match the mean fall times observed for each pixel (see Fig. 5.3 for the distribution of a given pixel). The amplitude in ADC bins was determined by applying the inverse of the calibration described below. The noise for each pulse was generated by randomly sampling a power spectrum of long baseline traces (or waveforms) of a few milliseconds. The amplitude of the noise was then scaled to the observed RMS baseline noise in each detector. A comparison of a simulated waveform to a waveform captured during production data taking can be seen in Fig. 5.17.

5.3 Spectrum Analysis

5.3.1 Single-Pixel Spectra

Single-pixel energy spectra are ^{45}Ca or calibration source spectra where the included events were confined to a single pixel and are separated by more that 1 μs from the nearest preceding and subsequent event. Energy was extracted as previously described in Sec. 5.1.1. The 1μs separation between events is much larger than the typical backscattering timeframe (see Fig 5.6). Therefore these single-pixel spectra are largely free of distortions which arise from backscattering processes. This timing cut also significantly reduces charge sharing effects for events which are incident near

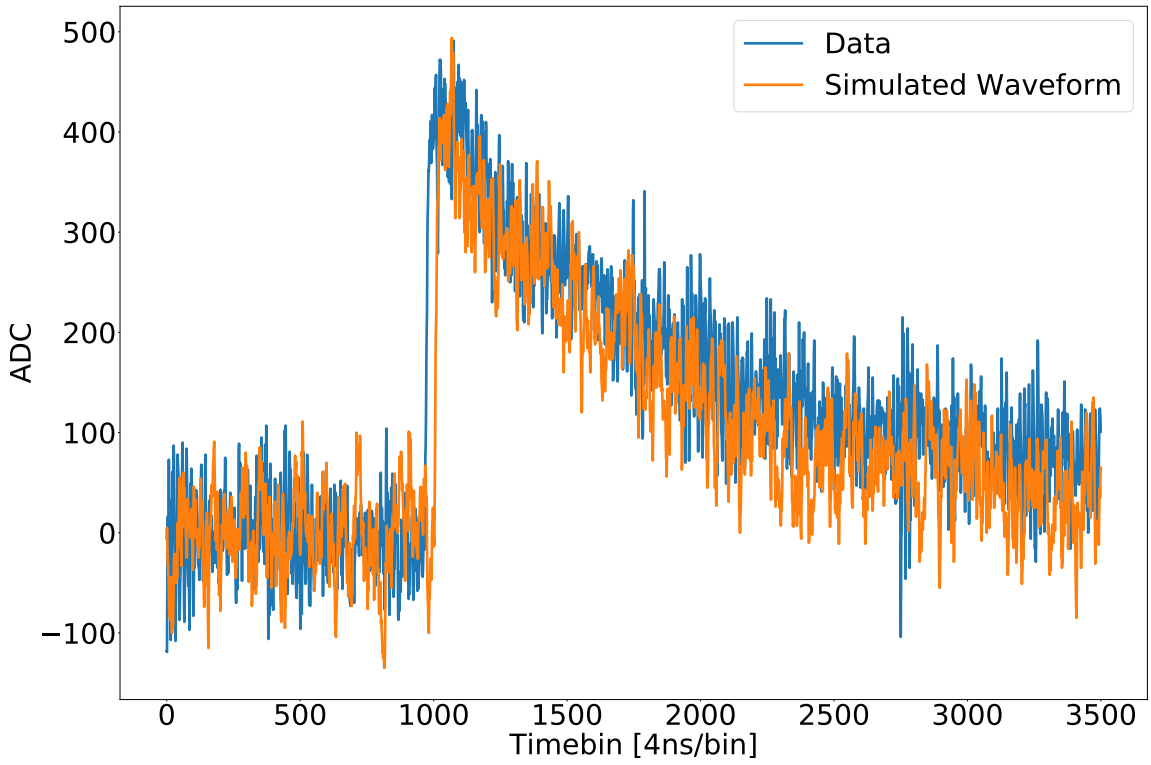

Figure 5.17: Shown above is a waveform recorded while running in blue and a simulated waveform in orange. The orange waveform was generated by convolving a semi-gaussian with a square pulse. Noise was superimposed by randomly sampling power spectra created from long baseline traces and adding the result to the waveform.

pixel boundaries. A goal of the ^{45}Ca experiment is to generate single-pixel spectra and look for distortions in the beta spectrum shape on a pixel-by-pixel basis. The data were subjected to several cuts, which will be discussed below. In the following discussion, the cuts were applied in the order in which they are described.

1. The first cut applied was a timing cut to reject waveforms with corruption present (see Fig. 5.18). The corruption occurred as a result of a race condition within the DAQ. This race condition took place when the RAM shared between eight channels of a given digitizer board was accessed for reading prior to the completion of writing to that sector. These events were generally the result of very low trigger thresholds. The higher event rates forced the DAQ to more frequently access the buffer and thus generate corrupted events. For every waveform, a timestamp and a request time are recorded. The timestamp corresponds to the time (in 4 ns clock ticks) when the trigger for the waveform was generated. The request time corresponds to the time (also in 4 ns clock ticks) at point the event was written to file. To determine whether an event was possibly corrupted, the timestamp of a given event was compared to the request time of neighboring events (ordered by timestamps) on the same board. An event was flagged as corrupted if the timestamp for that event was within 60 μs of a neighbor's request time. The timestamp corresponds to the first timebin of an event's waveform. To ensure that at no point corruption occurred along the waveform, the timestamp plus 3500 timebins (the length of a waveform) also was required to be greater than 60 μs from any neighbor's request time. This problem has been avoided in Nab by implementation of a software dead time.

2. A low energy pedestal cut was applied. All events with $E_{\text{event}} < 25$ keV were removed. See Fig. 5.8 for the effect of the energy cut on the ^{45}Ca and ^{113}Sn data.

3. A timing cut was also applied to remove multipixel events, as they require a separate analysis. A given event was rejected if it fell within 1 μs of its time

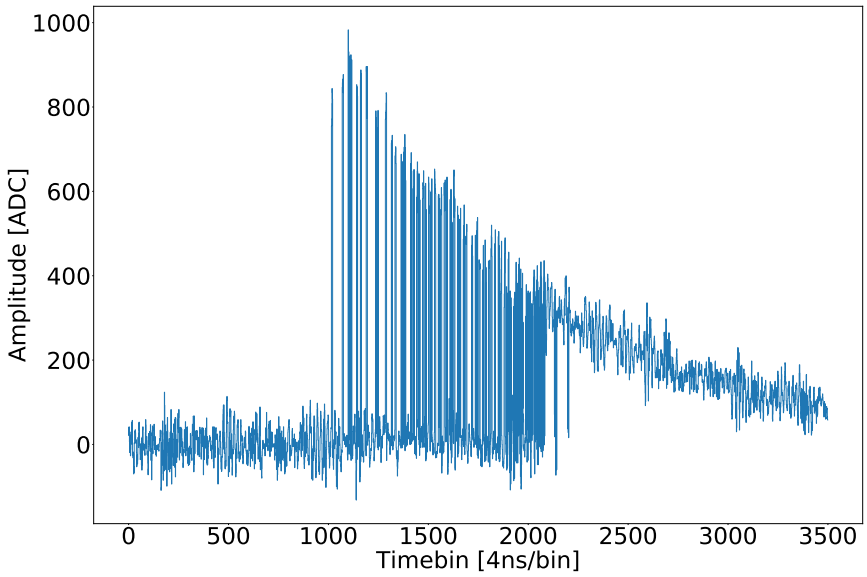

Figure 5.18: When a race condition occurs on a given digitizer board, the waveform being written to the buffer suffers corruption, as seen above.

ordered neighbors. The cut removed any events in which an electron deposits energy in one pixel and backscattered into another. This additionally removed events in which a particle was incident near pixel boundaries and charge sharing between two or more pixels. See Fig. 5.8 for the effect of the timing cut.

4. The DAQ trigger parameters for the ^{45}Ca experiment were not fully optimized. As a result, pulses with large amplitudes occasionally caused two or more triggers, which resulted in multiple recordings of a single waveform (See Fig. 5.19). Consequently, the timebin at which the trapezoidal filter used for energy extraction reached a maximum was was utilized to find these events. If this maximum fell within the first 2400 ns of the waveform, the event was discarded. This cut is referred to as the t_0 cut.

5. The next cut applied corresponds to an event classification. The three types considered are a single independent event, a single event which backscattered into the same pixel multiple times, and pile up events. For the first class, the energy simply corresponds to the calibrated trapezoidal output. For the second

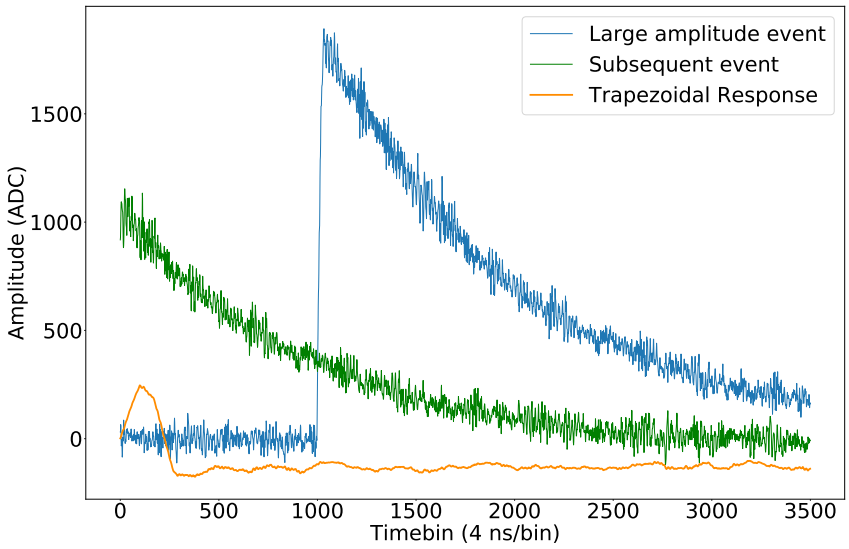

Figure 5.19: Due to inadequately optimized trigger parameters, an event with a sufficiently large amplitude created multiple triggers. This resulted in multiple waveforms being created at slightly later times.

class of event, small dead layer corrections must be applied to fully reconstruct an event's total energy. The third class must be thrown out entirely. The coincidence window of 400 ns discussed in Sec. 5.1.3 was used. The effect of the removal of these events from a single-pixel spectrum can be seen in Fig. 5.8.

6. Finally,the output of the LLS fits to an oscillating baseline are used to remove any events with a baseline oscillation larger that 50 ADC. The effect of the removal of these events may also be seen in Fig. 5.8.

5.3.2 Calibration & System Linearity

An important aspect of the detector system is the linearity of its response to a detected beta particle. The linearity of the detector system refers to the measured or detected energy in relation to those of other events. For example, if an energy of E' ADC is measured for an event of E keV, the system is considered to be linear

if $2 \cdot E'$ is measured for an event of $2 \cdot E$. A measurement of 'b' is determined by the energy spectrum of ^{45}Ca. To extract 'b', the system must either be linear to the uncertainty desired in 'b', or any non-linearities must be well understood and numerically characterized. For the ^{45}Ca experiment, the former will be shown.

Mono-energetic sources with well known energies are ideal for linearity characterization of the detectors and electronics chains. As such, conversion electron (CE) lines for ^{113}Sn, ^{207}Bi, and ^{139}Ce were used for this characterization (see Ch. 4 for details regarding the setup).

Calibration proceeded as follows. For a given radioactive source peak, the corresponding data was fit to a Gaussian plus a linear term. The linear term was implemented to better fit the low energy portion of each peak. The fit was restricted to a 2σ window about the maximum . This fit yielded a mean value $x_{\text{peak}} \pm \Delta x_{\text{peak}}$, where x_{peak} is in terms of ADC. Additionally, the corresponding simulated peaks were also fitted to Gaussians with means $\mu_{\text{peak}} \pm \Delta\mu_{\text{peak}}$ with μ_{peak} in keV. Then these measured peak locations (ADC) were linearly fit to simulated peak locations (keV) by least squares minimization. See Fig. 5.20 for the procedure applied to two pixels from each detector. The calibration uncertainty contribution for a 'b' extraction is discussed in more detail in Sec. 5.4.2.

To quantify the linearity of each calibration, the fractional residuals for each source peak were calculated with respect to the calibration line. These are shown in Fig. 5.20 for two pixels. The fractional residuals for each pixel are all below 0.02.

5.4 Fierz term extraction

The general procedure for extracting a Fierz interference term is to compare the spectra obtained from data to a simulated spectrum. One could in principle simulate numerous ^{45}Ca spectra with different values of the Fierz interference term and compare each one to data. These simulations however require time to accumulate sufficient statistics for a reasonable comparison. Therefore a general method is needed

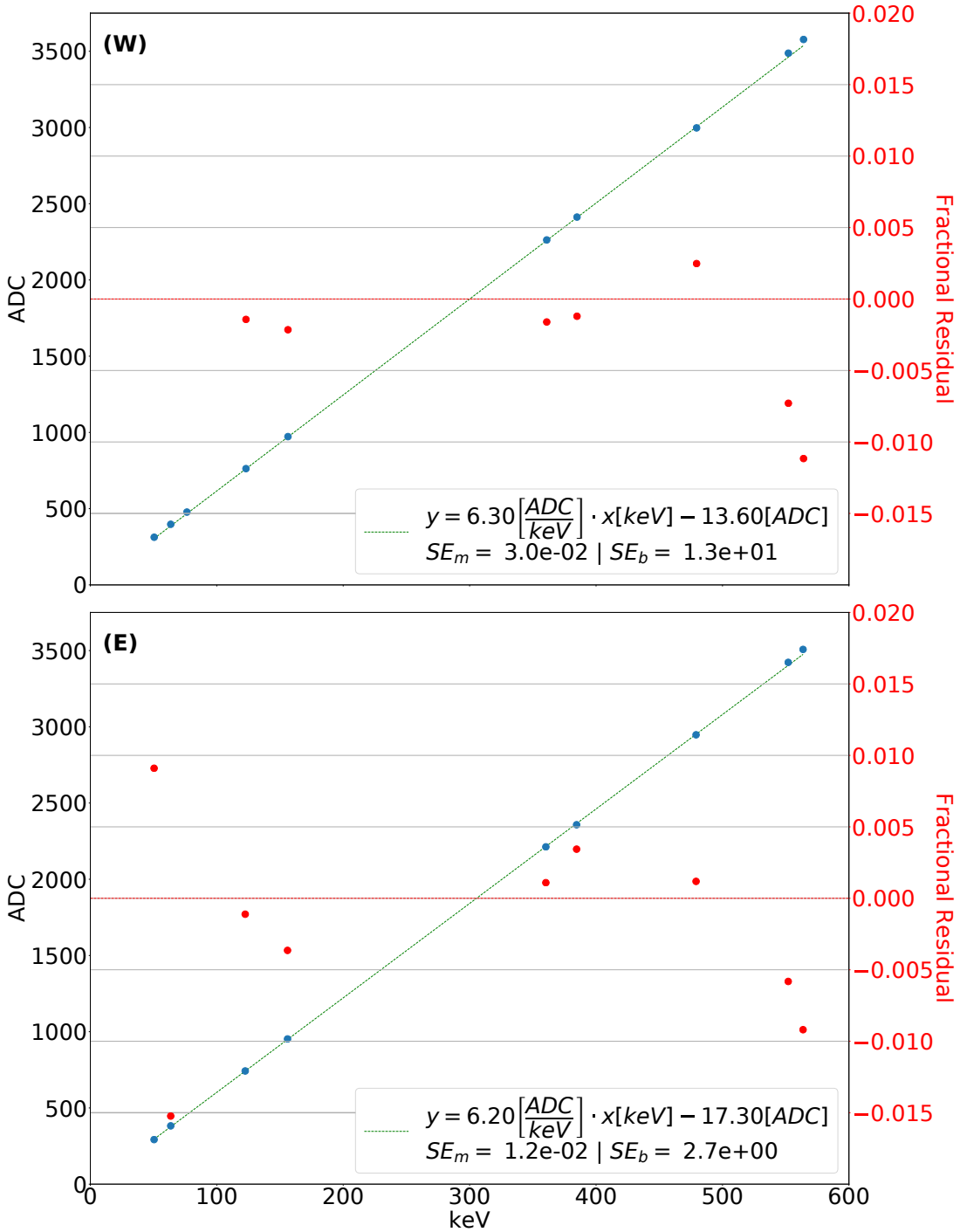

Figure 5.20: Plotted above is the detector calibration for a pixel on the West detector **(W)** and a pixel on the East detector **(E)**. The standard error (SE) for the slope and offset (m and b) is also given. Additionally, the red points correspond to the fractional residuals resulting from calibration at that specific point: $\frac{\text{data-fit}}{\text{fit}}$. The two detectors exhibit a very similar linear response as well as a comparable spread in fractional residuals.

which can be used for a 'b' extraction, but does not require a simulated ^{45}Ca spectrum at that value of 'b'. Recall that the decay rate for ^{45}Ca relevant to this experiment is given by integrating Eq. 1.10 over the electron and neutrino solid angles $d\Omega_e$ and $d\Omega_\nu$ respectively. This yields:

$$w\big(E_e\big) = \frac{F(Z,E_e)}{2\pi^3} p_e E_e \left(E_0 - E_e\right)^2 \xi \left(1 + b\frac{m_e}{E_e}\right) \tag{5.15}$$

Note that what is actually measured is the number of counts N at some reconstructed energy E_r. Electronic response and detector effects can each be modeled as a convolution of Eq. 5.15 with some response function. Let $\Phi(E)$ and $G_d(E)$ be the electronic and detector response respectively.

$$\begin{aligned} N(E_r) &= \eta \cdot \left(\Phi * \left(G_d * w\right)\right)(E_r) \\ &= \eta \int \Phi(E_r, E') G_d(E', E) w(E) dE dE' \end{aligned} \tag{5.16}$$

where η is simply a constant of proportionality. Note that $(G_d * w)(E)$ are the intermediate spectra as defined in Sec. 5.2. Define $w_{SM}(E_e) := \frac{F(Z,E_e)}{2\pi^3} p_e E_e \xi \left(E_0 - E_e\right)^2$, so that $w(E_e) = w_{SM}(E_e)\left(1 + b\frac{m_e}{E_e}\right)$. Then expanding $w(E_e)$ in the above equation yields:

$$\begin{aligned} N(E_r) =& \eta \int \Phi(E_r, E') G_d(E', E) w_{SM}(E_e) \left(1 + b\frac{m_e}{E_e}\right) dE dE' \\ =& \eta \Bigg(\int \Phi(E_r, E') G_d(E', E) w_{SM}(E_e) dE dE' \\ &+ b \int \Phi(E_r, E') G_d(E', E) w_{SM}(E_e) \frac{m_e}{E_e} dE dE' \Bigg) \end{aligned} \tag{5.17}$$

For the following discussion, the dependence of the decay rate on the Fierz interference term will be written explicitly. In effect $w(E_e) \rightarrow w(E_e; b) = w_{SM}(E_e)\left(1 + b\frac{m_e}{E_e}\right)$. Note that $w(E_e; 0) = w_{SM}(E_e)$ and $w(E_e; 1) - w(E_e; 0) = w_{SM}(E_e)\frac{m_e}{E_e}$. Then inserting these relations into Eq. 5.17 results in:

$$
\begin{aligned}
N(E_r) &= \eta\Bigg(\int \Phi(E_r, E')G_d(E', E)w(E_e; 0)dEdE' \\
&\qquad + b\int \Phi(E_r, E')G_d(E', E)\left(w(E_e; 1) - w(E_e; 0)\right)dEdE'\Bigg) \\
&= \eta\Bigg(\int \Phi(E_r, E')G_d(E', E)w(E_e; 0)dEdE' \\
&+b\int \Phi(E_r, E')\left(\int G_d(E', E)w(E_e; 1)dE - \int G_d(E', E)w(E_e; 0)dE\right)dE'\Bigg) \\
&= \eta\Bigg(\int \Phi(E_r, E')(G_d * w(b = 0))(E')dE' \\
&+b\int \Phi(E_r, E')\left(G_d * w(b = 1))(E') - (G_d * w(b = 0)(E')\right)dE'\Bigg)
\end{aligned}
\tag{5.18}
$$

Then with intermediate ^{45}Ca spectra generated with 'b'=0 and 'b'=1 and a reasonable approximation of $\Phi(E_r, E')$, the above relation can be used to fit observed ^{45}Ca spectra ($N(E_r)$) to a linear combination of 'b'=0 and 'b'=1 simulations and extract a Fierz term. The only fit parameters in the above expression are η and 'b'. This approach allows for a Fierz extraction while only requiring two different values of 'b' for MC simulation.

The only corrections explicitly written in Eq. 5.15 are the BSM contributions and the Fermi function which accounts for the first order electromagnetic interaction between the decay electron and the daughter nucleus. There are a number of other effects which also modify the beta spectrum. These effects are thoroughly discussed in Ref. [64], and the numerical algorithm which generates the corrected spectrum is described in Ref. [79]. The spectra used in this analysis were generated from and in

collaboration with the authors of Refs. [64, 79]. All corrections described in these references were included.

5.4.1 Fierz Extraction for Pixel 64 E

The above procedure was carried out for the single-pixel spectra of pixel 64E (the central pixel of the East detector). The width of the electronic response was found to be $\sigma_\Phi = 2.04$ keV. To extract the Fierz term, the realistic MC spectrum was subjected to the same cuts outlined in Sec. 5.3.1. The waveform specific cuts such as the t_0 cut and corruption cut were not applicable to MC. Pixel 77 was inoperable for each detector. In order for MC to reflect these circumstances, any events which deposited energy on pixel 77 were removed. In the cases where an event deposits some energy in pixel 77 and backscatters into another pixel, only the energy deposition in pixel 77 is removed from the MC data stream. Then with MC as data-like as possible, the intermediate b=0 and b=1 spectra were convolved with the electronic response function for pixel 64E, and Eq. 5.18 was used to fit the resulting MC spectra to data. The fit range was chosen to maximize the number of bins over which the fit is performed. The trigger efficiency is $\sim 99.9\%$ at 150 keV (see Sec. 5.4.2 for more detail). As such, 150 keV was taken as the beginning of the fit range. The end of the fit range was dictated by statistical uncertainty. At 220 keV, the relative statistical uncertainty $N/\sqrt{N} = 0.01$, which is at the level of the desired uncertainty in an extracted value of 'b'. A value of $b = 0.40 \pm 0.06 \pm \sigma_{\text{syst.}}$ was extracted (see Fig. 5.21).

5.4.2 Uncertainties

Source Position and Distribution

The strong magnetic field of the SCS (1 T) confines any decay electron emitted by the ^{45}Ca or any other source used to a small area of a few mm^2. Each pixel of the detectors covers an area of about 1 cm^2. The West and East detectors, each with the seven central pixels instrumented, should therefore cover the entire 4π sr solid

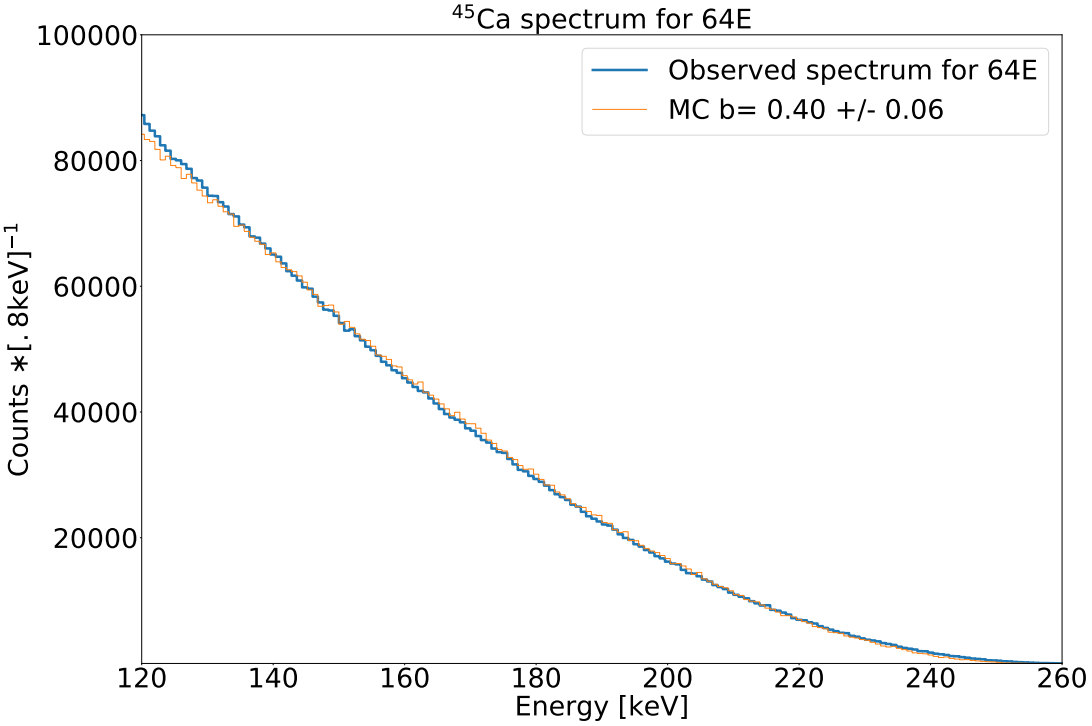

Figure 5.21: Shown above is the observed single-pixel spectrum for the central pixel of the East detector (64E). The data is fit to a linear combination of b=0 and b=1 realistic MC spectra. The extracted Fierz term is indicated in the legend. The uncertainty only reflects the uncertainty of the fit. Systematics have not yet been included.

angle of electron emission from any source properly centered in the magnetic field. With a fully functioning detector, exact knowledge of the source position would not be critical. Summed spectra could be used instead of single-pixel spectra to extract a Fierz term. These summed spectra are nearly independent of geometric effects and therefore subject to less uncertainty in source positioning. Because of a bug in the DAQ firmware and a malfunctioning FET/preamp chain, no useful data was collected for pixels 77 East and 77 West. The active pixels therefore did not cover the full 4π, and some geometric effects or uncertainties must be quantified.

As noted in Ch. 4, the exact location of each source was not known to better than an inch or so. Furthermore, the physical distribution of the source material on the foil was also not well quantified. Therefore the simulated source positions had to be inferred from relative pixel count rates. See Fig. 5.22 for a distribution of count rates among the active pixels. The spot size was ascertained to be roughly 0.6 mm in diameter (see Ref. [74]). Although the most of the ^{45}Ca beta decay electrons are captured captured by pixels 64E/W and 65W, roughly 1% of the decay events are missed in pixels 77E/W.

To determine the impact on a 'b' extraction, a full Fierz term extraction was carried out for MC events restricted to a particular quadrant of the source. See Fig. 5.23 for the dimensions of the simulated source as well as the extracted value of 'b' for each quadrant. The net effect of this variation resulted in an uncertainty of $\sigma_{\text{pos.}} = ^{+0.01}_{-0.07}$.

Trapezoidal Energy Extraction

A systematic study was also carried out to quantify the uncertainty in the energy extraction procedure described above in Sec. 5.1.1. For a fixed energy, 10,000 waveforms were generated as described above in Sec. 5.2. The risetime of each waveform was randomly sampled from a distribution of risetimes observed. For each waveform, a simulated energy was extracted using a trapezoidal filter with parameters prescribed in Sec. 5.1.1. An average difference of the known and extracted energy was

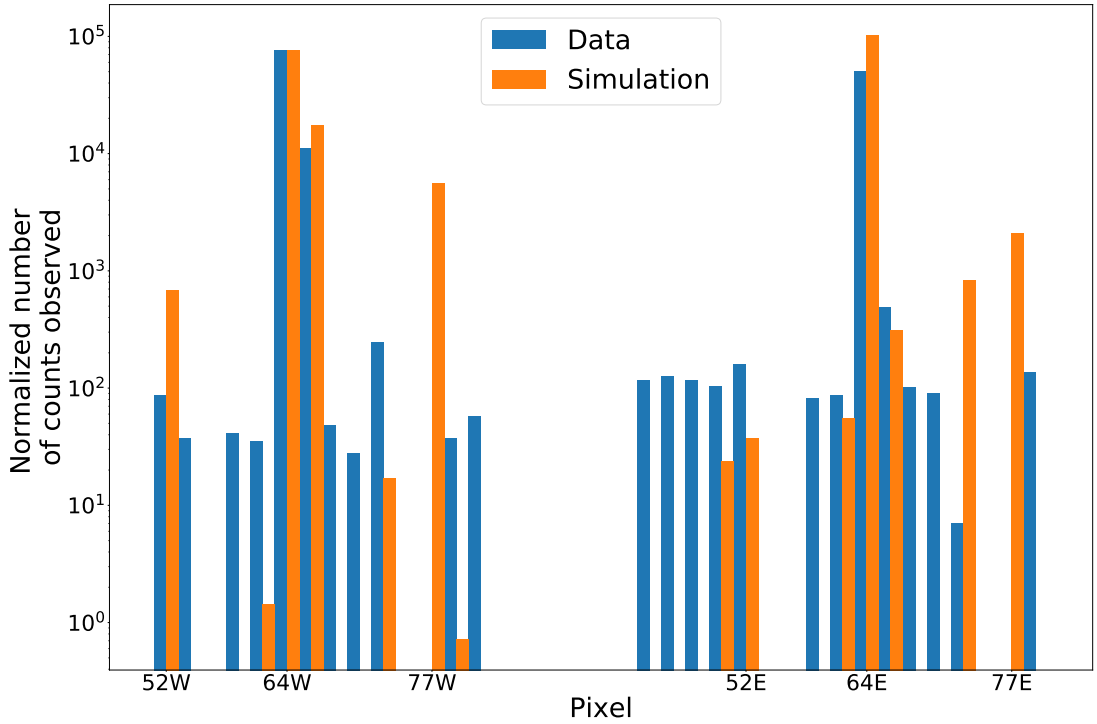

Figure 5.22: Above is a distribution of the number of events on each pixel with $E > 150$ keV for run 120 compared to that of simulation (total number of events in 64W scaled to that of run 120).

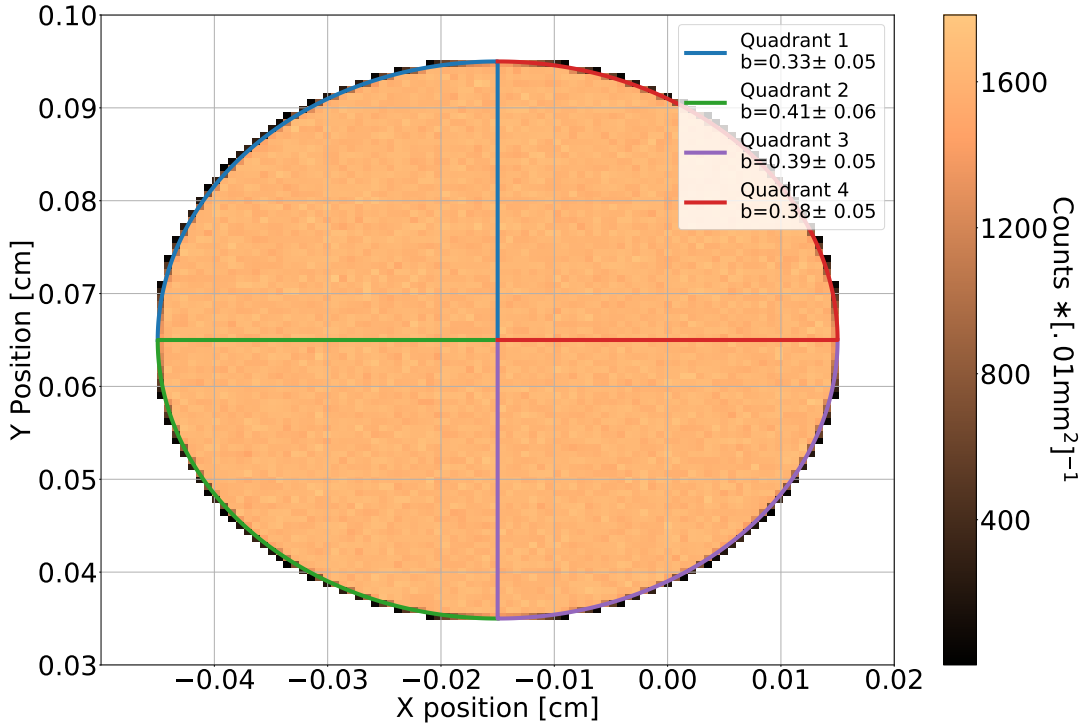

Figure 5.23: Shown above is the simulated ^{45}Ca source geometry. The value of the Fierz interference term that results when restricting MC events to a particular quadrant is shown in the legend.

recorded for the set of 10,000 waveforms. The energy was varied over a 0-600 keV range. The uncertainty was found to scale as $\delta X/X \sim 0.025$ where X is the known energy in ADC. Then the uncertainty in keV is given as $\delta E/E \sim 0.025 * m$, where m is the slope of the calibration for a particular pixel. To determine the impact of this uncertainty on a 'b' extraction, a resampling procedure was utilized. To this end, a histogram of single-pixel event energies was created from observed events (data). Each bin of the histogram was resampled according to a gaussian distribution with a width of $0.025 \cdot m \cdot E$. The resulting data was then used to extract a Fierz interference term. This process was repeated 1,000 times and the standard deviation in 'b' was taken as the systematic uncertainty introduced by the trapezoidal filter. Using this method, a systematic uncertainty of $\sigma_{\text{trap}} = 0.02$ was found.

Baseline Oscillation

A similar study to the above in Sec. 5.4.2 was carried out to determine the uncertainty in 'b' due to baseline oscillation. Waveforms that were found to have an oscillating baseline of an amplitude greater than 50 ADC were removed. To estimate an uncertainty due to the remaining oscillations, the following strategy was employed. The contribution of an oscillating baseline to the trapezoidal filter output was calculated in Eq. 5.13. Typically the energy is read off from the trapezoidal output from around the 1350'th timebin (see Fig. 5.2). An amplitude of $B = 50$ADC was assumed and the output of corresponding to the 1350'th timebin of Eq. 5.13 was recorded for 10^6 randomly sampled phases ϕ. The integral of this distribution was normalized to unity. This distribution was taken as the approximate probability distribution and is shown in Fig. 5.24. This distribution was randomly sampled and added to $b = 0$ event energies. This new $b = 0$ spectrum was then fitted according to the above prescription in Sec. 5.4 to extract a value of 'b'. This process was repeated one thousand times, where the value of 'b' was recorded for each iteration. The value of the systematic uncertainty introduced by the baseline oscillation was estimated as the standard deviation in this distribution of values of 'b'. This gave $\sigma = 0.06$. The

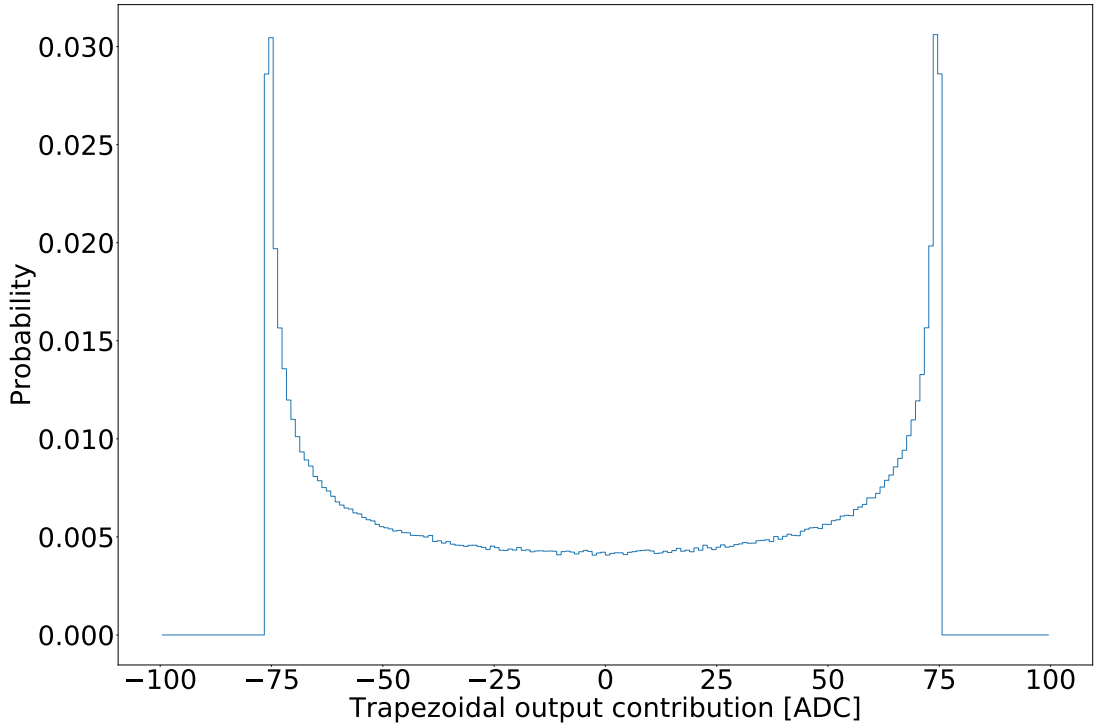

Figure 5.24: MC $b = 0$ and $b = 1$ event energies were resampled to include potential distortions from an oscillating baseline. Shown above is the probability distribution used in the resampling.

process was then repeated for a $b = 1$ spectrum, and the standard deviation in 'b' agreed to within 0.005 of the $b = 0$ spectrum.

Finite MC Statistics

Because an extraction of 'b' is achieved using MC, as opposed to an analytic function, the uncertainty of 'b' also depends on the statistical uncertainty present in the MC used. A resampling method was also used to ascertain the effect of this statistical uncertainty on a value of 'b'. For this study, the b=0 and b=1 MC event energy histograms were resampled. The number of counts in each bin was randomly resampled according to a poisson distribution $P(N) = \bar{N}^N e^{-\bar{N}}/N!$, where $\bar{N}$ is taken to be the number of counts in each MC energy bin. This process was repeated 100,000 times and resulted in a value of $\sigma_{\text{MCstat.}} = 0.04$. See Fig. 5.25 for a distribution of extracted values.

DAQ Trigger Efficiency

A set of simulated waveforms was used to study the DAQ trigger efficiency. The waveforms were generated as outlined in Sec. 5.2. To accurately model the DAQ response to each event, the waveforms were subjected to the trigger scheme as discussed in Sec. 4.3.2, where the double trapezoidal parameters were chosen to match those of the DAQ filter. See Fig. 5.26 for a plot of these efficiencies as a function of energy for the two central pixels. These trigger efficiencies were taken into account when choosing the appropriate fit range for the Fierz term fits. At 150 keV, the trigger efficiency contributes an uncertainty of $\sigma = 0.003$; the smallest contribution to the uncertainty in 'b'.

Deadtime correction

A 60 μs software dead time was implemented in the above analysis to remove events with corruption. As noted above, a race condition within the DAQ FPGA

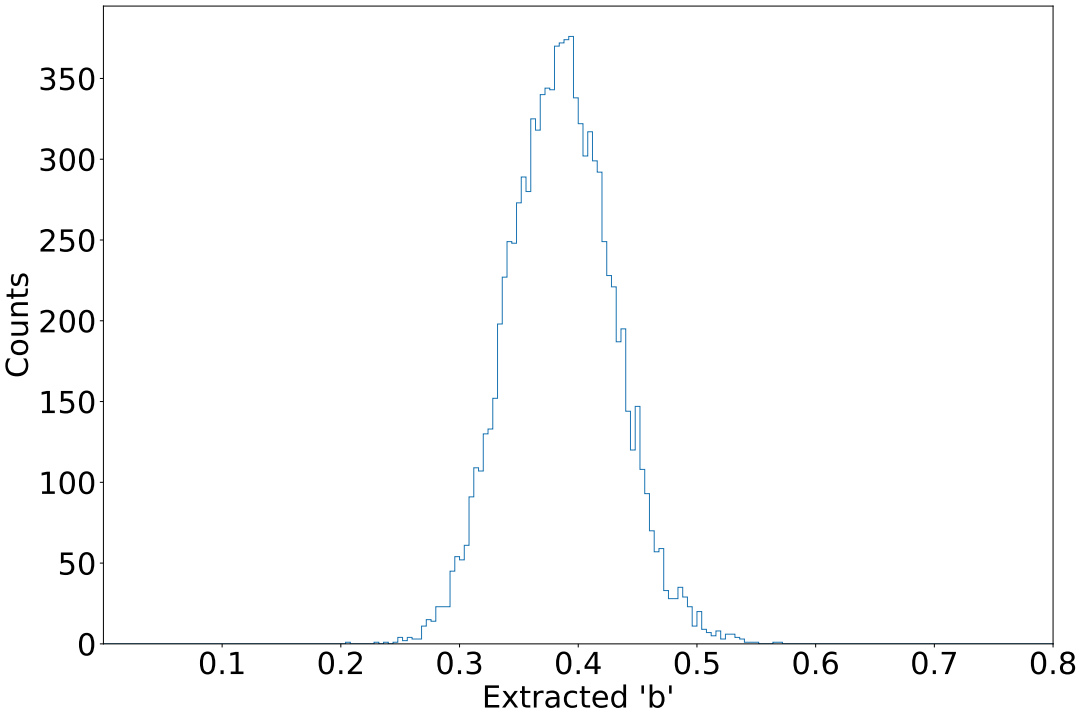

Figure 5.25: Shown above is a histogram of the various values of 'b' extracted by resampling the number of counts in each energy bin of realistic MC, for both b=0 and b=1 spectra. The MC was resampled according to poisson statistics.

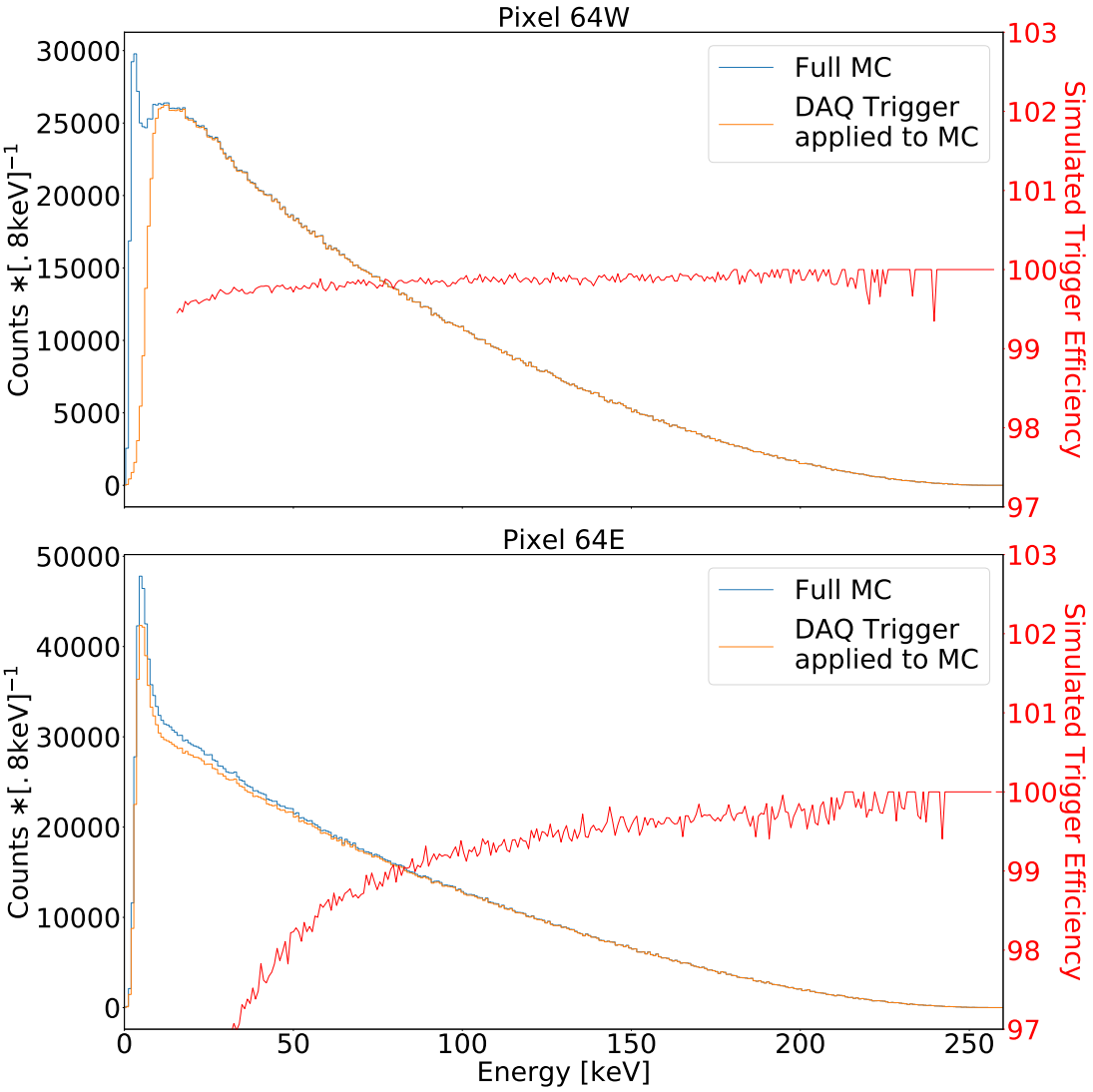

Figure 5.26: Above, the simulated trigger efficiencies for the two central detector pixels is shown. The root-mean-square (RMS) baseline noise of the East pixels was about twice as large as those of the West detector pixels. This difference in signal-to-noise ratio is the primary cause for the difference in simulated trigger efficiencies.

necessitated the implementation of a software dead time of 60μs. The ^{45}Ca activity was about 1 kBq, or 1 ms on average between each decay event. Then the observed rate is reduced by a factor of $\frac{1}{1+10^3[counts/s]\cdot 6\cdot 10^{-5}[s]} = 94.3\%$ of the actual rate. This contribution only amounts to an overall multiplicative factor applied to each energy bin. Hence the overall shape remains the same and the correction may be neglected in a Fierz analysis.

Fit Region

The fit region was chosen by maximizing the range of the included beta spectrum while minimizing the statistical uncertainty in 'b'. Since trigger efficiencies were not included in MC spectra, the inefficiencies over the fitted region were required to be small, $\sim 0.1\%$. As can be seen in Fig. 5.26, the simulated trigger efficiency is about 99.9% at 150 keV for pixel 64E. 150 keV was chosen as the lower limit of the fit range for pixel 64E. The upper limit was chosen such that $\frac{\sigma_{\text{stat}}}{N} \sim 0.01\%$ where N is the number of counts in some energy bin. Solving for N yields $N = 10^6$ counts. Thus the highest energy bin used corresponds to the last bin where $N > 10^6$. This corresponds to an energy of 220 keV for pixel 64E. To determine the uncertainty introduced by this choice of the fit range, the lower and upper energy bins were varied by ± 4 keV which corresponds to 5 bins at 0.8 keV per bin, and a new value of 'b' was extracted. The upper and lower limits of this variation are reported as $\sigma_{\text{region}} = ^{+0.03}_{-0.04}$.

Calibration Error

The calibration used also introduces a source of uncertainty in an extraction of 'b'. Naively, one can again use the aforementioned method of resampling the calibration slope and offset according to the reported errors of the calibration fit parameters. The data are recalibrated according to the resampled slope and offset values and a value of 'b' is extracted using the new calibration. This was done and the uncertainty was found to be $\sigma_{\text{cal.}} \sim ^{+0.2}_{-0.1}$. This strategy does not, however, take into account the

correlation between the slope and the offset of the linear calibration. Instead, the following approach was also implemented. The calibration source peaks have some gaussian width in ADC. Each peak centroid was shifted according to a resampling of a gaussian distribution with the aforementioned width, and a new set of calibration parameters were fit to the resampled peak centroids. The set of calibration parameters for each resampling was then applied to ^{45}Ca data, and a value of 'b' was extracted. This was done with 1,000 different source peak resamplings. A value of $\sigma = ^{+0.77}_{-0.45}$ was found.

Final Value

A summary of the contributions to the dominant systematic uncertainties in an extraction of 'b' is given below in Table 5.1. The uncertainties were added in quadrature resulting in a value of $b = 0.40 \pm 0.05_{\text{stat}} \pm ^{+0.78}_{-0.47\text{sys}}$.

Table 5.1: Above is a list of systematic uncertainties with the approaches used to determine the effect on an extraction of the Fierz interference term. Calibration uncertainty is the dominant uncertainty on the order of 'b'.

Systematic	Uncertainty in 'b'
Calibration Uncertainty	$^{+0.77}_{-0.45}$
Trapezoidal Filter Energy Extraction	0.02
Electronic Response Modeling	0.05
Baseline Oscillation	0.06
MC Source Positioning	$^{+0.01}_{-0.07}$
Detector Efficiency	0.003
MC Statistics	0.04
Fit Range Variation	$^{+0.03}_{-0.04}$

Chapter 6

Conclusion

6.1 Past Fierz Interference Searches

In addition to the that of the ^{45}Ca experiment outlined in Ch. 4, several other Fierz or Fierz related searches have been performed or are currently underway. These results are obtained by one of three approaches. BSM ft values, beta decay correlation coefficient measurements, and beta spectrum shape distortion measurements can all provide limits on 'b'.

BSM ft Values

Recall that the BSM ft values given by Eq. 1.18 include a Fierz component. The term $\left\langle \frac{m_e}{E_e} \right\rangle$ is determined numerically. ξ, however, is a function of the BSM mixing ratio $|\tilde{\rho}|$ (see Eq.1.14). For any transition with a nonzero Gamow-Teller component, $|\tilde{\rho}|$ can be determined from a measurement of the electron-neutrino correlation coefficient 'a' or the beta asymmetry parameter 'A'. Measurement of 'a' for all but neutrons tends to be difficult, as such a measurement entails either a measurement of the nuclear recoil (see Ref. [80]) or the outgoing neutrino momentum. In the case of super-allowed $0^+ \rightarrow 0^+$ Fermi transitions, the expression for 'b' is greatly simplified. With $M_{GT} = 0$ for these transitions, the Fierz term is only a function of scalar

BSM couplings: $b_F := 2\gamma \mathrm{Re}\left(\frac{C_S+C'_S}{C_V+C'_V}\right)$. The notation b_F is used here simply to denote that the transitions in consideration are Fermi transitions and thus free of tensor current contributions. Assuming only left-handed currents present in the transition ($|\tilde{V_{ud}}| \rightarrow |V_{ud}|$), the ft value is then given as:

$$ft = \frac{K}{2G_F^2|V_{ud}|^2\left(1 + b_F\left\langle\frac{m_e}{E_e}\right\rangle\right)} \tag{6.1}$$

A value of $b_F = -0.0028 \pm 0.0026$ is reported in Ref. [35].

The BSM Beta Asymmetry Parameter

Measurements of the beta asymmetry parameter 'A' have also been used to set limits on 'b'. In general, the results are reported in the form of a BSM beta asymmetry parameter $\tilde{A}$. A nonzero value of 'b' essentially contaminates the beta asymmetry parameter: ($A \rightarrow \tilde{A} = \frac{A}{1+\frac{m_e}{E_e}b}$). The results then are usually left in the form of $\tilde{A}$ without disentangling the contribution from 'b'. See Refs. [81–84] for such results for various nuclei or Ref. [85] for a review of these measurements.

6.1.1 Beta Spectrum Measurements

Along with the ^{45}Caexperiment discussed in Chs. 4 and 5, several other experiments have been attempted or are underway which aim to precisely measuring the beta energy spectrum and extract a Fierz interference term.

Ultracold Neutrons

A measurement of 'b' for ultra-cold neutrons (UCN) has been performed and the results are discussed in Ref. [86]. This measurement was extracted from the UCNA 2010 data set of Ref. [52]. The goal of the UCNA experiment was to measure the beta asymmetry parameter 'A' of Eq. 1.9 for ultra cold neutrons (UCN). An extraction of 'A' requires polarized UCN and a measurement of the momentum of the electrons

resulting from beta decay of the UCN. A detailed description of the setup as well as the extraction method can be found in Ref. [52]. The spectrometer utilized for the measurement was the SCS of Ch. 4, with a different detector package. Instead of silicon detectors, a multi-wire proportional chamber in front of a scintillating detector at each end of the SCS were used to measure electron momenta. A beta spectrum was generated by taking "super" sum of detector count rates and a value of 'b' was extracted from the resulting spectrum. A result of $b = 0.067 \pm 0.005_{\text{stat}}{}^{+0.090}_{-0.061\ \text{sys}}$ was reported [86].

^{6}He & ^{20}F Calorimetry

Another interesting experiment poised to measure the Fierz interference term for ^{6}He is ongoing at The National Superconducting Cyclotron Laboratory (NSCL) of Michigan State University. Instead of magnetically confining decay electrons by a strong magnetic field as was done for the ^{45}Ca and UCNA experiments, the decaying ^{6}He nuclei were deposited deep within a scintillating calorimeter [87]. This implantation then allows for all decay particle energy (with the possible exception of Brehmsstrahlung) to be collected. I.e. the detector is free from backscatter effects. The spectra of ^{6}He and ^{20}F have been taken and a projected uncertainty of 0.1% for 'b' is anticipated. A preliminary result for the beta decay of ^{20}F with $b = 0.0021 \pm 0.0051_{\text{stat}} \pm 0.0084_{\text{sys}}$ is reported in Ref. [88].

^{6}He Cyclotron Radiation Emission Spectroscopy

At the University of Washington, a slightly different approach is being implemented to measure the beta decay spectrum of ^{6}He. Instead of using conventional solid state or scintillating detectors to measure the energy of an electron, energy is extracted using cyclotron radiation emission spectroscopy (CRES). The apparatus essentially consists of a large magnetic field created within an electromagnetic radiation waveguide. Instead of using a solid source, the beta decay source exists

as a gas trapped within the waveguide. Because the source exists in a gaseous state, as opposed to a solid source, there are no electron energy losses due to transport through a source foil. As the electrons spiral around the field lines, a very small but measureable amount of cyclotron radiation is emitted. The waveguide allows for collection of this radiation, and an energy is determined by frequency analysis of the collected radiation. See Refs. [89, 90] for more detail regarding the operating principals and technical setup. Using this method for the beta decay of ^{6}He, the collaboration (Project 8) is projected to extract a preliminary result with $\Delta b \sim 10^{-3}$, followed up by an even more precise extraction on the 10^{-4} level.

6.2 Summary and Outlook

The primary goals of this work were to develop a cooling system and explore an analysis strategy for the extraction of the Fierz interference term, 'b', for the Nab experiment. The former was addressed by constructing and testing several prototypes for related experiments such as the UCNB and ^{45}Ca beta spectrum measurements. The first system investigated was a standard LN_2 cooled system. This cooling method resulted in an additional source of noise in waveform data which arose from the physical shaking of the cooling lines. These microphonics stemmed from the vaporization of LN_2 along the cooling lines. To mitigate this as well as a few logistical problems for Nab, the cooling system was redesigned. The updated design features recirculating helium gas, cooled by a cold head. A prototype which utilized LN_2 to cool the helium gas was tested. This demonstrated a proof-of-principle for the Nab cooling system and was followed up with a more realistic prototype to cool the detector system for the ^{45}Ca beta spectrum measurement. This design brought the necessity of utilizing separate cooling lines to light. Additionally, the test also demonstrated the ability to control the system temperature to the 0.1 K level, well under the 0.5 K stability required by Nab.

The work performed in the extaction of the Fierz term for the beta decay of ^{45}Ca addresses the second major goal of this work. The ^{45}Ca beta spectrum measurement was setup and took data in the summer of 2017. The raw waveform data was analyzed using various digital signal processing methods, and energies were extracted for each event. Single-pixel spectra were constructed. These spectra only include that were confined to a single pixel and well separated in time. The calibration source spectra and MC simulated spectra were used to calibrate the extracted energies from ADC units to keV. The linearity of the calibration was such that the fractional residuals of calibration source peaks were below the $2 \cdot 10^{-2}$ level, with respect to the linear calibration. This calibration was applied to data. The calibration source data was also used to precisely determine an electronic response function. Intermediate MC calibration source data were fit to observed spectra by convolving a gaussian distribution with the MC spectra, where the width of the distribution was fit as a free parameter. This electronic response function was used to produce realistic spectra from the intermediate MC data. A value of 'b' was extracted by fitting a linear combination of realistic $b = 0$ and $b = 1$ MC spectra to ^{45}Ca data, with an overall normalization and 'b' as free fit parameters. Finally, a set of systematic studies were conducted to quantify the dominant systematic uncertainties in the extraction of the Fierz term. A value of $b = 0.40 \pm 0.05_{\text{stat}} \pm^{+0.78}_{-0.47\text{sys}}$ was found.

In comparison, the value extracted of 'b' extracted in this work places less stringent constraints on the Fierz interference term for ^{45}Ca than those of Sec. 6.1. While many experimental conditions were sub-optimal for a precise Fierz extraction for ^{45}Ca, many problems likely to be encountered for Nab were illuminated in this process. Many difficulties present for the analysis of the ^{45}Ca data have been circumvented for Nab by various changes to the DAQ firmware. The information gained from the cooling system will also be a key component in Nab detector stability. The usage of separate lines of recirculating, cold Helium gas for the upper and lower detectors will allow for much finer adjustments of detector temperatures for Nab. Finally, the analysis strategy for an extraction of 'b' has not yet been finalized for Nab. This

work provides insight into benefits and pitfalls of one such route. The knowledge and lessons learned provided by the ^{45}Ca beta spectrum measurement will be used by the Nab experiment to achieve a competitive Fierz interference extraction with $\delta b \sim 10^{-3}$.

Bibliography

[1] M. S. Jean-Louis Basdevant, James Rich, *Fundamentals in Nuclear Physics*. Springer, 2005. 1

[2] K. Heyde, *Basic Ideas and Concepts in Nuclear Physics*. Institute of Physics Publishing, 1999.

[3] K. Krane, *Introductory Nuclear Physics*. John Wiley & Sons Inc., 1988. 1

[4] A. Pais, *Inward Bound*. Oxford University Press, 1988. 2

[5] F. L. Wilson, "Fermi's theory of beta decay," *American Journal of Physics*, vol. 36, no. 12, pp. 1150–1160, 1968. 2

[6] C. L. Cowan, F. Reines, F. B. Harrison, H. W. Kruse, and A. D. McGuire, "Detection of the free neutrino: a confirmation," *Science*, vol. 124, no. 3212, pp. 103–104, 1956. 2

[7] E. Segrè, "Spontaneous fission," *Phys. Rev.*, vol. 86, pp. 21–28, Apr 1952. 2

[8] M. Pftzner, E. Badura, C. Bingham, *et al.*, "First evidence for the two-proton decay of ^{45}Fe," *Eur Phys J A*, 2002. 2

[9] J. D. Jackson, S. B. Treiman, and H. W. Wyld, "Possible tests of time reversal invariance in beta decay," *Phys. Rev.*, vol. 106, pp. 517–521, May 1957. 14, 15, 16, 56

[10] E. Olsen, M. Pfützner, N. Birge, M. Brown, W. Nazarewicz, and A. Perhac, "Landscape of two-proton radioactivity," *Phys. Rev. Lett.*, vol. 110, p. 222501, May 2013. 2

[11] S. Weinberg, "A model of leptons," *Phys. Rev. Lett.*, vol. 19, pp. 1264–1266, Nov 1967. 2, 3

[12] J. W. A. Salam, "Weak and electromagnetic interactions," *Nuovo Cim (1959) 11: 568*, 1958.

[13] S. L. Glashow, "The renormalizability of vector meson interactions," *Nuclear Physics*, vol. 10, pp. 107 – 117, 1959. 2, 3

[14] M. Gonzlez-Alonso, O. Naviliat-Cuncic, and N. Severijns, "New physics searches in nuclear and neutron decay," *Progress in Particle and Nuclear Physics*, vol. 104, pp. 165 – 223, 2019. 2, 13, 15, 17, 56

[15] P. W. Higgs, "Broken symmetries and the masses of gauge bosons," *Phys. Rev. Lett.*, vol. 13, pp. 508–509, Oct 1964. 3

[16] F. Englert and R. Brout, "Broken symmetry and the mass of gauge vector mesons," *Phys. Rev. Lett.*, vol. 13, pp. 321–323, Aug 1964. 3

[17] G. Arnison, *et al.*, "Experimental observation of isolated large transverse energy electrons with associated missing energy at s=540 gev," *Physics Letters B*, vol. 122, no. 1, pp. 103 – 116, 1983. 3

[18] G. Arnison, *et al.*, "Experimental observation of lepton pairs of invariant mass around 95 gev/c2 at the cern sps collider," *Physics Letters B*, vol. 126, no. 5, pp. 398 – 410, 1983.

[19] G. Aad, *et al.*, "Observation of a new particle in the search for the standard model higgs boson with the atlas detector at the lhc," *Physics Letters B*, vol. 716, no. 1, pp. 1 – 29, 2012. 3, 5

[20] R. Davis, "A review of the homestake solar neutrino experiment," *Progress in Particle and Nuclear Physics*, vol. 32, pp. 13 – 32, 1994. 3

[21] *et. al*. Fukuda, Y., "Evidence for oscillation of atmospheric neutrinos," *Phys. Rev. Lett.*, vol. 81, pp. 1562–1567, Aug 1998.

[22] G. Mention, M. Fechner, T. Lasserre, T. A. Mueller, D. Lhuillier, M. Cribier, and A. Letourneau, "Reactor antineutrino anomaly," *Phys. Rev. D*, vol. 83, p. 073006, Apr 2011. 3

[23] *et. al*. T. Saeki, "A new limit on the flux of cosmic antihelium," *Physics Letters B*, vol. 422, no. 1, pp. 319 – 324, 1998. 3

[24] A. G. Cohen, A. D. Rújula, and S. L. Glashow, "A matter-antimatter universe?," *The Astrophysical Journal*, vol. 495, pp. 539–549, mar 1998.

[25] *et. al*. J. Alcaraz, "Search for antihelium in cosmic rays," *Physics Letters B*, vol. 461, no. 4, pp. 387 – 396, 1999. 3

[26] W. Contributors, "Standard model," May 2019. 4

[27] C. S. Wu, E. Ambler, R. W. Hayward, D. D. Hoppes, and R. P. Hudson, "Experimental test of parity conservation in beta decay," *Phys. Rev.*, vol. 105, pp. 1413–1415, Feb 1957. 7

[28] C. Burgess and G. D. Moore, *The Standard Model: A primer*. Cambridge University Press, 2011. 9, 11

[29] T. D. Lee and C. N. Yang, "Question of parity conservation in weak interactions," *Phys. Rev.*, vol. 104, pp. 254–258, Oct 1956. 10, 13

[30] M. G. V. Cirigliano, M. Gonzlez-Alonso, "Non-standard charged current interactions: beta decays versus the lhc," *J. High Energ. Phys.*, vol. 46, 2013. 12, 13

[31] M. Tanabashi, *et al.*, "Review of particle physics," *Phys. Rev. D*, vol. 98, p. 030001, Aug 2018. 12, 13, 19, 20, 24

[32] J. Hardy and I. Towner, "$|v_{ud}|$ from nuclear β decays," *PoS CKM2016*, 2016. 13, 17, 18

[33] T. Bhattacharya, V. Cirigliano, S. D. Cohen, A. Filipuzzi, M. González-Alonso, M. L. Graesser, R. Gupta, and H.-W. Lin, "Probing novel scalar and tensor interactions from (ultra)cold neutrons to the lhc," *Phys. Rev. D*, vol. 85, p. 054512, Mar 2012. 13

[34] M. Ebel and G. Feldman, "Further remarks on coulomb corrections in allowed beta transitions," *Nuclear Physics*, vol. 4, pp. 213 – 214, 1957. 14, 16

[35] J. C. Hardy and I. S. Towner, "Superallowed $0^+ \to 0^+$ nuclear β decays: 2014 critical survey, with precise results for V_{ud} and ckm unitarity," *Phys. Rev. C*, vol. 91, p. 025501, Feb 2015. 17, 18, 19, 21, 122

[36] W. J. Marciano and A. Sirlin, "Improved calculation of electroweak radiative corrections and the value of V_{ud}," *Phys. Rev. Lett.*, vol. 96, p. 032002, Jan 2006. 17, 22

[37] C. Patrignani *et al.*, "Review of Particle Physics," *Chin. Phys.*, vol. C40, no. 10, p. 100001, 2016. 18, 26

[38] J. F. Donoghue and D. Wyler, "Isospin breaking and the precise determination of vud," *Physics Letters B*, vol. 241, no. 2, pp. 243 – 248, 1990. 18

[39] M. Ademollo and R. Gatto, "Nonrenormalization theorem for the strangeness-violating vector currents," *Phys. Rev. Lett.*, vol. 13, pp. 264–266, Aug 1964. 18

[40] G. L. Greene, E. G. Kessler, R. D. Deslattes, and H. Börner, "New determination of the deuteron binding energy and the neutron mass," *Phys. Rev. Lett.*, vol. 56, pp. 819–822, Feb 1986. 19

[41] J. Byrne, *Neutrons, nuclei, and matter: an exploration of the physics of slow neutrons.* Dover, 1994. 19

[42] J. M. Robson, "Radioactive decay of the neutron," *Phys. Rev.*, vol. 78, pp. 311–312, May 1950. 19

[43] J. M. Robson, "The radioactive decay of the neutron," *Phys. Rev.*, vol. 83, pp. 349–358, Jul 1951. 19

[44] D. Dubbers and M. G. Schmidt, "The neutron and its role in cosmology and particle physics," *Rev. Mod. Phys.*, vol. 83, pp. 1111–1171, Oct 2011. 20

[45] W. Mampe, P. Ageron, C. Bates, J. M. Pendlebury, and A. Steyerl, "Neutron lifetime measured with stored ultracold neutrons," *Phys. Rev. Lett.*, vol. 63, pp. 593–596, Aug 1989. 21

[46] S. Arzumanov, L. Bondarenko, S. Chernyavsky, W. Drexel, A. Fomin, P. Geltenbort, V. Morozov, Y. Panin, J. Pendlebury, and K. Schreckenbach, "Neutron life time value measured by storing ultracold neutrons with detection of inelastically scattered neutrons," *Physics Letters B*, vol. 483, no. 1, pp. 15 – 22, 2000. 21

[47] P. R. Huffman, C. R. Brome, J. S. Butterworth, K. J. Coakley, M. S. Dewey, S. N. Dzhosyuk, R. Golub, G. L. Greene, K. Habicht, S. K. Lamoreaux, C. E. H. Mattoni, D. N. McKinsey, F. E. Wietfeldt, and J. M. Doyle, "Magnetic trapping of neutrons," *Nature*, vol. 403, pp. 62–64, Jan. 2000. 21

[48] Pattie, R. W. , *et. al*, "Measurement of the neutron lifetime using a magneto-gravitational trap and in situ detection," *Science*, vol. 360, no. 6389, pp. 627–632, 2018. 21, 22

[49] J. S. Nico, M. S. Dewey, D. M. Gilliam, F. E. Wietfeldt, X. Fei, W. M. Snow, G. L. Greene, J. Pauwels, R. Eykens, A. Lamberty, J. V. Gestel, and R. D. Scott, "Measurement of the neutron lifetime by counting trapped protons in a cold neutron beam," *Phys. Rev. C*, vol. 71, p. 055502, May 2005. 21

[50] D. Wilkinson, "Phase space for neutron beta-decay: an update," *Nuclear Instruments and Methods in Physics Research Section A: Accelerators, Spectrometers, Detectors and Associated Equipment*, vol. 404, no. 2, pp. 305 – 310, 1998. 22

[51] Brown, M. A.-P. *et. al*, "New result for the neutron β-asymmetry parameter A_0 from ucna," *Phys. Rev. C*, vol. 97, p. 035505, Mar 2018. 22, 39, 94, 96

[52] Mendenhall, M. P. *et. al*, "Precision measurement of the neutron β-decay asymmetry," *Phys. Rev. C*, vol. 87, p. 032501, Mar 2013. 22, 122, 123

[53] A. T. Yue, M. S. Dewey, D. M. Gilliam, G. L. Greene, A. B. Laptev, J. S. Nico, W. M. Snow, and F. E. Wietfeldt, "Improved determination of the neutron lifetime," *Phys. Rev. Lett.*, vol. 111, p. 222501, Nov 2013. 22

[54] *et. al*. R. Alarcon, "Precise Measurement of the Neutron Beta Decay Parameters "a" and "b"," *Proposal for an Experiment at the Spallation Neutron Source*, 2007. 24

[55] R. Alarcon *et. al*, "Precise measurement of $\lambda = g_a/g_v$ and search for non-(v-a) weak interaction terms in neutron decay," *Funding proposal for the neutron decay spectrometer Nab at SNS*, 2010. 24

[56] N. Fomin, G. Greene, R. Allen, V. Cianciolo, C. Crawford, T. Tito, P. Huffman, E. Iverson, R. Mahurin, and W. Snow, "Fundamental neutron physics beamline at the spallation neutron source at ornl," *Nuclear Instruments and Methods in Physics Research Section A: Accelerators, Spectrometers, Detectors and Associated Equipment*, vol. 773, pp. 45 – 51, 2015. 25, 139

[57] G. Knoll, *Radiation Detection and Measurement*. John Wiley & Sons, Inc., 1999. 32, 63, 64, 65, 66, 81

[58] J. S. Blakemore, *Semiconductor statistics*. Courier Corporation, 2002. 33

[59] R. Pires, R. Dickstein, S. Titcomb, and R. Anderson, "Carrier freezeout in silicon," *Cryogenics*, vol. 30, no. 12, pp. 1064 – 1068, 1990. 33

[60] J. Ramsey, "Nab preamp assembly," tech. rep., Los Alamos National Lab, ramseyjc@ornl.gov, 2017. 38

[61] L.J. Broussard *et. al*, "Detection system for neutron β decay correlations in the ucnb and nab experiments," *Nuclear Instruments and Methods in Physics*

Research Section A: Accelerators, Spectrometers, Detectors and Associated Equipment, vol. 849, pp. 83–93, 2017. 37, 61, 67, 96

[62] A. Salas-Bacci *et. al*, "Characterization of large area, thick, and segmented silicon detectors for neutron -decay experiments," *Nuclear Instruments and Methods in Physics Research Section A: Accelerators, Spectrometers, Detectors and Associated Equipment*, vol. 735, pp. 408 – 415, 2014. 37, 61, 67, 96

[63] V. Grillo, "Cryofab bayonet heat leak rates," tech. rep., Cryofab, 2018. 49

[64] L. Hayen, N. Severijns, K. Bodek, D. Rozpedzik, and X. Mougeot, "High precision analytical description of the allowed β spectrum shape," *Rev. Mod. Phys.*, vol. 90, p. 015008, Mar 2018. 57, 96, 108, 109

[65] N. Severijns and O. Naviliat-Cuncic, "Structure and symmetries of the weak interaction in nuclear beta decay," *Physica Scripta*, vol. T152, p. 014018, jan 2013. 57

[66] B. R. Holstein, "Recoil effects in allowed beta decay: The elementary particle approach," *Rev. Mod. Phys.*, vol. 46, pp. 789–814, Oct 1974. 57

[67] B. R. Holstein, "Erratum: Recoil effects in allowed beta decay: The elementary particle approach," *Rev. Mod. Phys.*, vol. 48, pp. 673–673, Oct 1976.

[68] N. Severijns, "Correlation and spectrum shape measurements in β-decay probing the standard model," *Journal of Physics G: Nuclear and Particle Physics*, vol. 41, p. 114006, oct 2014. 57

[69] T. W. Burrows, "Nuclear data sheets 109, 171," 2008. 58

[70] "Isotrak." Website, 2019. 58

[71] B. Plaster *et. al*, "A solenoidal electron spectrometer for a precision measurement of the neutron -asymmetry with ultracold neutrons," *Nuclear Instruments and*

Methods in Physics Research Section A: Accelerators, Spectrometers, Detectors and Associated Equipment, vol. 595, no. 3, pp. 587 – 598, 2008. 61

[72] W. Bludau, A. Onton, and W. Heinke, "Temperature dependence of the band gap of silicon," *Journal of Applied Physics*, vol. 45, no. 4, pp. 1846–1848, 1974. 63

[73] "Micron semiconductor limited." 65

[74] B. Zeck, *Angular Correlation and Spectroscopy Measurements of the β-Decay of Neutrons and ^{45}Ca Nuclei.* PhD thesis, North Carolina State University, 2019. 65, 74, 111

[75] A. Jezghani, *A Detection and Data Acquisition System for Precision Beta Decay Spectroscopy.* PhD thesis, University of Kentucky, 2019. 67

[76] V. T. Jordanov and G. F. Knoll, "Digital synthesis of pulse shapes in real time for high resolution radiation spectroscopy," *Nuclear Instruments and Methods in Physics Research Section A: Accelerators, Spectrometers, Detectors and Associated Equipment*, vol. 345, no. 2, pp. 337 – 345, 1994. 67, 74, 75, 79

[77] M. R. Bhat, "Evaluated nuclear structure data file (ensdf)," 2019. Data extracted using the NNDC On-Line Data Service from the ENSDF database, file revised as of March 15, 2019. 96

[78] T. Kibdi, T. Burrows, M. Trzhaskovskaya, P. Davidson, and C. Nestor, "Evaluation of theoretical conversion coefficients using bricc," *Nuclear Instruments and Methods in Physics Research Section A: Accelerators, Spectrometers, Detectors and Associated Equipment*, vol. 589, no. 2, pp. 202 – 229, 2008. 96

[79] L. Hayen and N. Severijns, "Beta spectrum generator: High precision allowed spectrum shapes," *Computer Physics Communications*, vol. 240, pp. 152 – 164, 2019. 108, 109

[80] Gorelov, A. *et. al*, "Scalar interaction limits from the $\beta-\nu$ correlation of trapped radioactive atoms," *Phys. Rev. Lett.*, vol. 94, p. 142501, Apr 2005. 121

[81] B. R. Holstein, "Limit on fierz interference in nuclear beta decay," *Phys. Rev. C*, vol. 16, pp. 753–756, Aug 1977. 122

[82] F. Wauters, V. D. Leebeeck, I. Kraev, M. Tandecki, E. Traykov, S. V. Gorp, N. Severijns, and D. Zákoucký, "β asymmetry parameter in the decay of ^{114}In," *Phys. Rev. C*, vol. 80, p. 062501, Dec 2009.

[83] F. Wauters, I. Kraev, D. Zákoucký, M. Beck, M. Breitenfeldt, V. De Leebeeck, V. V. Golovko, V. Y. Kozlov, T. Phalet, S. Roccia, G. Soti, M. Tandecki, I. S. Towner, E. Traykov, S. Van Gorp, and N. Severijns, "Precision measurements of the ^{60}Co β-asymmetry parameter in search for tensor currents in weak interactions," *Phys. Rev. C*, vol. 82, p. 055502, Nov 2010.

[84] G. Soti, F. Wauters, M. Breitenfeldt, P. Finlay, P. Herzog, A. Knecht, U. Köster, I. S. Kraev, T. Porobic, P. N. Prashanth, I. S. Towner, C. Tramm, D. Zákoucký, and N. Severijns, "Measurement of the β-asymmetry parameter of ^{67}Cu in search for tensor-type currents in the weak interaction," *Phys. Rev. C*, vol. 90, p. 035502, Sep 2014. 122

[85] N. Severijns, M. Beck, and O. Naviliat-Cuncic, "Tests of the standard electroweak model in nuclear beta decay," *Rev. Mod. Phys.*, vol. 78, pp. 991–1040, Sep 2006. 122

[86] Hickerson, K. P. *et. al*, "First direct constraints on fierz interference in free-neutron β decay," *Phys. Rev. C*, vol. 96, p. 042501, Oct 2017. 122, 123

[87] X. Huyan, O. Naviliat-Cuncic, D. Bazin, A. Gade, M. Hughes, S. Liddick, K. Minamisono, S. Noji, S. V. Paulauskas, A. Simon, P. Voytas, and D. Weisshaar, "Toward a measurement of weak magnetism in 6he decay," *Hyperfine Interactions*, vol. 237, p. 93, May 2016. 123

[88] M. Hughes, *Precision Measurements in ^{20}F Beta Decay*. PhD thesis, Michigan State University, 2019. 123

[89] D. M. Asner, R. F. Bradley, L. de Viveiros, P. J. Doe, J. L. Fernandes, M. Fertl, E. C. Finn, J. A. Formaggio, D. Furse, A. M. Jones, J. N. Kofron, B. H. LaRoque, M. Leber, E. L. McBride, M. L. Miller, P. Mohanmurthy, B. Monreal, N. S. Oblath, R. G. H. Robertson, L. J. Rosenberg, G. Rybka, D. Rysewyk, M. G. Sternberg, J. R. Tedeschi, T. Thümmler, B. A. VanDevender, and N. L. Woods, "Single-electron detection and spectroscopy via relativistic cyclotron radiation," *Phys. Rev. Lett.*, vol. 114, p. 162501, Apr 2015. 124

[90] A. A. Esfahani, S. Bser, C. Claessens, L. de Viveiros, P. J. Doe, S. Doeleman, M. Fertl, E. C. Finn, J. A. Formaggio, M. Guigue, K. M. Heeger, A. M. Jones, K. Kazkaz, B. H. LaRoque, E. Machado, B. Monreal, J. A. Nikkel, N. S. Oblath, R. G. H. Robertson, L. J. Rosenberg, G. Rybka, L. Saldaña, P. L. Slocum, J. R. Tedeschi, T. Thmmler, B. A. Vandevender, M. Wachtendonk, J. Weintroub, A. Young, and E. Zayas, "Results from the project 8 phase-1 cyclotron radiation emission spectroscopy detector," *Journal of Physics: Conference Series*, vol. 888, p. 012074, sep 2017. 124

[91] N. Birge, "Mass table calculations with nuclear density functional theory," Master's thesis, University of Tennessee, Knoxville, 2015. 153

Appendix

Appendix A

Maximum Proton Kinetic Energy in Neutron Beta Decay

For simplicity, natural units will be used for the proceeding derivation. Also, all masses written are rest masses. The Q-value is defined as the restmass of the decaying mother minus the rest mass of all the decay products. For free neutron decay $Q = m_n - m_p - m_e - m_\nu \approx m_n - m_p - m_e$. The neutrons will be considered to decay at rest. This is reasonable for the above discussion, as the neutrons used in the Nab experiment are cold neutrons with a kinetic energy $T_n < 1$ eV [56]. For the following, let E, T, p denote total energy, kinetic energy and momentum. Any subscripts will denot the particle to which the energy or momentum belongs. Energy and momentum conservation imply:

$$Q = T_p + T_e + T_\nu \tag{A.1}$$

$$-\mathbf{p_p} = \mathbf{p_e} + \mathbf{p}_\nu \tag{A.2}$$

Squaring both sides of Eq. A.2 gives:

$$p_p^2 = p_e^2 + p_\nu^2 + 2p_e p_\nu \cos(\theta_{e\nu}) \tag{A.3}$$

Now the proton kinetic energy is obviously maximized by maximizing the proton momentum. Then from the above p_p^2 is maximal when $\theta_{e\nu} = 0$, so Eq. A.3 becomes:

$$p_p^2 = p_e^2 + p_\nu^2 + 2p_e p_\nu \tag{A.4}$$

Now $p_p = \left(E_p^2 - m_p^2\right)^{1/2}$ and $E = T + m$. Taking the neutrino as massless ($E_\nu = T_\nu = p_\nu$), Eq. A.4 becomes:

$$\begin{aligned} E_p^2 - m_p^2 &= p_e^2 + T_\nu^2 + 2T_\nu p_e \\ \rightarrow T_p^2 + 2m_p T_p &= p_e^2 + T_\nu^2 + 2T_\nu p_e \end{aligned} \tag{A.5}$$

Then solving Eq. A.1 for T_ν and inserting the result into Eq. A.5

$$T_p^2 + 2m_p T_p = p_e^2 + (Q - T_e - T_p)^2 + 2(Q - T_e - T_p)p_e \tag{A.6}$$

Then solving the above for T_p yields:

$$T_p = \frac{(Q - T_e + p_e)^2}{2\left(Q - T_e + p_e + m_p\right)} \tag{A.7}$$

Now at the maximum proton kinetic energy, $\frac{dT_p}{dT_e} = 0$. Thus taking the derivative of Eq. A.7 and solving for T_e gives:

$$T_e = \frac{Q}{2\left(1 + \frac{m_e}{Q}\right)} \tag{A.8}$$

Then inserting the value found for the electron kinetic energy into Eq. A.7 gives a maximum proton kinetic energy of 634 eV $<<$ $m_p = 938$ GeV. Thus:

$$E_p = T_p + m_p \approx m_p \tag{A.9}$$

Appendix B

High voltage feedthrough design drawings

The technical drawings for the high voltage transfer lines used in Nab experiment were uploaded as an attachment (see HV_FT_drawing.pdf). The design requirements presented a couple of challenges. The lines were required to stand off the 30 kV potential between the inner and outer high voltage cages while transporting a cryogenic coolant to the Nab detector mount. Therefore the lines not only had to be electrically isolating but also minimize thermal heat contamination. For one, any contamination diminishes the cooling power of the helium gas used to cool the detectors. Additionally, heat leaks also ultimately result in condensation and freezing of atmospheric water on the transfer line. The buildup of condensation of water or frost eventually would lead to an electrical short of 30 kV to ground along the high voltage feedthroughs. By itself, electrical isolation or thermal insulation of a transfer line is solvable via commercially available, economical products. The requirement of the lines to be both electrical isolating an thermally insulated was not as straightforward. There were croygenic suppliers willing to construct such a line, however the prices quoted were prohibitive and the lead times very large. As such, the idea was put forward to construct vacuum jacketed transfer lines from G-10 and assemble them

locally. Two of the three initial prototypes survived 10 rounds of thermal cycling. To mitigate internal stresses brought about by thermal expansion, the inner line of the feedthrough was redesigned to incorporate a bellows.

Appendix C

Ramsey Bayonet design drawings

The technical drawings for the Ramsey bayonets were uploaded as an attachment (see Ramsey_bayonet_drawing.pdf). These mount with the high voltage feedthroughs of Sec. B in the high voltage cage and mate with the detector mount cooling lines. These were produced by Cryofab according to the design specifications.

Appendix D

Dip Tube Feedthrough design drawings

The technical drawings for the dip tube feedthroughs were uploaded as an attachment (see dip_tube_feedthrough_drawing.pdf). This allows the dip tube of the vacuum jacketed, flexible transfer lines to mate with the vacuum vessel in which the cold head resides.

Appendix E

Vacuum vessel design drawings

The technical drawings for the vacuum vessel which houses the Sumitomo CH-110 cold head were uploaded as an attachment (see Vacuum_vessel_drawing.pdf). This provides the insulating vacuum for the cold head and heat exchangers used to cool the recirculating heliumg gas.

Appendix F

Heat exchanger design and drawings

The technical drawings for the Nab heat exchangers were uploaded as an attachment (see HE_drawing.pdf). The Nab cooling goal set forth was to be able to bring the detector temperature to $\sim$ 100K with a stability of 0.5K over the length of a run. As discussed in Ch. 3, a simple cold coiled tube proved to be an insufficient heat exchanger to accomplish these goals. Hence the design of the cooling system was modified. A Sumitomo Ch-110 cold head was substituted for LN_2 as the heat sink for the system. It is a single stage cold head with a cooling power of $\sim$ 140W at 50K. Thus with an adequately designed heat exchanger, much colder helium can be delivered to the detector mount.

The primary objective was to design a more turbulent heat exchanger. A schematic of the first prototype attempt can be seen in Fig. F.2. It should be noted that at this point, LN_2 was still intended to be used as the heat sink. The prototype was essentially a stainless steel box with copper fins to break up the flow. The heat exchanger was to be submerged in LN_2 and helium gas passed through the heat exchanger. After its construction, pressure drop across the heat exchanger was measured for various flow rates (see Fig. F.2 for a schematic of the setup). With room temperature nitrogen at

140 PSI, the maximum pressure drop measured across the heat exchanger was less than a few PSI. Although such a low pressure drop was unexpected, the more valuable lesson learned from the prototype was the need to create a flexible and adaptable design. There were many unknowns and variables that had to be accommodated by the heat exchanger, so iterating upon the design would be likely. Thus the design in the attached technical drawings was eventually settled upon.

The outer body of the heat exchanger is a standard 4.5" conflat half nipple fitting silver soldered to a solid copper base. The conflat flange allows for the heat exchanger to be extended if need be by bolting a second conflat full nipple to the end of the heat exchanger. For Nab, the extension would be unnecessary, however it does provide some flexibility for any future uses.

The inner fins of the first prototype were instead replaced with copper spacers and disks. The advantage to these is that both the disks and spacers may be added, removed or even swapped for thinner pieces. Should more impedance be desired, thinner spacers may be used and more disks may be added. For less impedance, disks may simply be removed. This adaptability thus allows the heat exchanger to be utilized over a much broader set of flow rates and pressures.

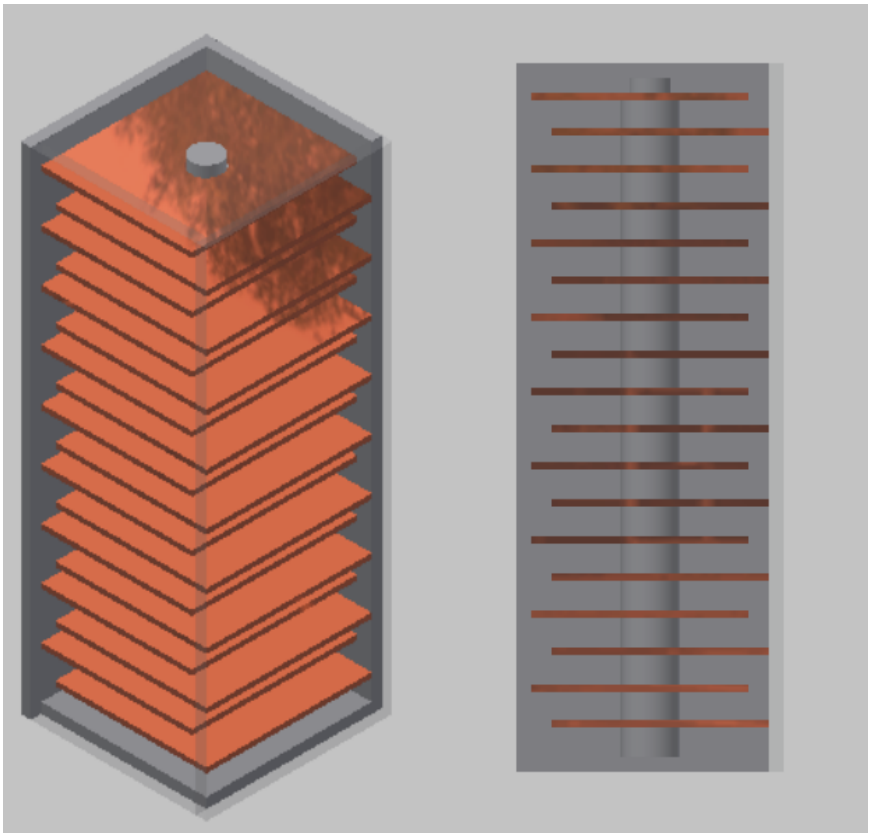

Figure F.1: Shown above are two views of a 3D model of the first heat exchanger prototype. Two outer stainless steel walls are transparent to show the internal geometry. A rod was welded to the bottom of the heat exchanger. Stainless steel spacers and copper fins were stacked along the length of the heat exchanger. Helium gas enters through the bottom via a 1/4" VCR fitting (not shown). The orientation of the fins were designed to force the gas to serpentine around each fin and maximize the total gas path length through the heat exchanger. Gas exits the heat exchanger through a 1/4" VCR fitting at the top (not shown).

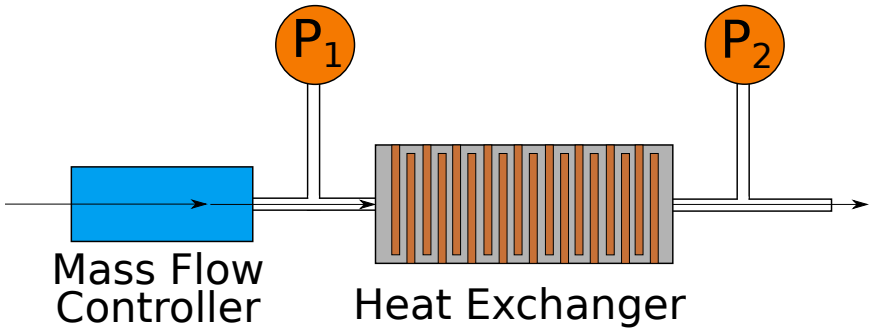

Figure F.2: The above setup was used to measure the impedence of the heat exchanger prototype. Room temperature nitrogen gas at roughly 140 PSI was provided by ORNL. The flow was regulated by a mass flow controller, and the pressures at P_1 and P_2 were measured for various flow rates. The pressure drop of the heat exchanger is defined as the difference of P_1 and P_2.

Appendix G

Heat exchanger mount plate design drawings

The technical drawings for the heat exchanger mount plate were uploaded as an attachment (see HE_mount_plate_drawing.pdf). This piece mounts to the Sumitomo CH-110. The heat exchangers are coupled to the cold head using this mount plate. The plate is entirely OFHC copper for optimal thermal conductivity between the cold head and the heat exchangers.

Appendix H

Full Cooling Schematics

Process and Instrumentation Diagrams (PID) of the schematic shown in Fig.3.1 have also been included as an attachment (Cooling_loop_schematics.pdf). These schematics provide a more detailed view of the cooling system and the included components. The design and preliminary P&ID work was performed by the author of this work. The final drawings in the attachment were the work of Maria Zemke.

Vita

Noah Watson Birge was born in Des Moines, Iowa and grew up in Dallas, Texas. In high school, he excelled in mathematics and science courses, but did not develop a serious interest in physics until his second year as an undergraduate at The University of Tennessee at Knoxville. At that time, he changed his major from a pre-medicine concentration to an academic physics and mathematics double major. In his last year as an undergraduate, he began working in a Theoretical Nuclear Physics group. This work was continued in his graduate career at the University of Tennessee. His advisor accepted a position with another university and as a result, Noah was unable to continue to pursue his PhD with said group. The results of his work were instead published as a Master's Thesis in Ref. [91]. After receiving his Master's in Nuclear Theory, Noah was accepted to the Fundamental Neutron Physics Group, with Professor Nadia Fomin as his advisor.